分 类 号： 0572.22　　单位代码： 10422
密　　级： 公开　　学　　号： D2017069

山东大学

博士学位论文

Thesis for Doctoral Degree

论文题目： 在 ATLAS 实验同号双轻子末态中寻找伴随单顶夸克产生的希格斯玻色子

Search for Higgs Boson production associated with single top quark in same sign di-lepton final state at ATLAS

作者姓名 Khuram Tariq
学院名称 前沿交叉科学青岛研究院
专业名称 粒子物理与原子核物理
指导老师 冯存峰
合作导师 李冰

2022 年 12 月 2 日

原 创 性 声 明

本人郑重声明：所呈交的学位论文，是本人在导师指导下，独立进行研究所取得的成果。除文中已经注明引用的内容外，本论文不包含任何其他个人或集体已经发表或撰写过的科研成果。对本论文的研究作出重要贡献的个人和集体，均已在文中以明确方式标明。本声明的法律责任由本人承担。

论文作者签名：______ 日 期：2022.12.02

关于学位论文使用授权的声明

本人完全了解山东大学有关保留、使用学位论文的规定，同意学校保留或向国家有关部门或机构送交论文的复印件和电子版，允许论文被查阅和借阅；本人授权山东大学可以将本学位论文全部或部分内容编入有关数据库进行检索，可以采用影印、缩印或其他复制手段保存论文和汇编本学位论文。

（保密的论文在解密后应遵守此规定）

论文作者签名：______ 导师签名：______ 日 期：2022.12.02

Contents

ABSTRACT

The study of the couplings of Higgs boson to other elementary particles, is essential to test the Standard Model (SM) predictions. The only scalar boson in the SM is also responsible for the mass of elementary particles. So the top quark, the most massive particle ever discovered should have a strong coupling with the Higgs boson. The Yukawa coupling of the Higgs boson to the Top quark y_t, is of particular interest and a key parameter of the SM. It can be determined indirectly from the $gg \to H$ production through a top-quark loop and directly from cross-section measurements of top-quark pair production associated with a Higgs boson (ttH). The production the ttH process has been recently observed, probing the Yukawa interactions between the Higgs boson and top quarks. However, the ttH production rate is sensitive only to the magnitude of y_t and has no sensitivity to its sign. The production of Higgs bosons in association with a single top quark (tHq production) process is sensitive to magnitude as well as sign of Higgs-top-Yukawa coupling, y_t. In the SM hypothesis ($y_t = +1$), the interference between these two diagrams is maximally destructive and leads to very small production cross-sections of about 71, 16 and 2.9 fb for the t-, tW- and s-channel, respectively, at $\sqrt{s} = 13$ TeV. New physics effects could lead to constructive interference between the ttH and WWH couplings and enhance the cross-sections by an order of magnitude or more.

This thesis presents the first results for the production of a Higgs boson in association with a single top quark with ATLAS experiment. The data collected with the ATLAS detector at LHC at $\sqrt{s} = 13$ TeV between 2015 and 2018 corresponding to integrated luminosity of 139.0 fb^{-1} is used. The tHq and tWH processes are considered as separate tH productions, while the s-channel production is neglected. The search uses final states distinguished by the number and flavour of leptons: two same-charge light-flavour leptons and no hadronically-decaying τ leptons (2LSS), targeting Higgs decay modes to WW^*, ZZ^*, and $\tau\tau$. A dedicated categorization is developed and optimised to enhance the sensitivity of the search. The boosted decision tree algorithm is used to discriminate between signal and background. The dominant background of fake leptons is estimated with the Template-Fit method (validated by Matrix Method) and charge flip background is estimated with Data-driven technique.

Assuming a positive or negative sign of the top-quark Yukawa coupling relative to its SM value, using all the relevant Higgs boson decay modes, no significant deviation from the background- only hypothesis is observed. The biggest contribution to the $\mu(tHq)$ is given by the data statistical uncertainty. The observed (expected) upper limit on the signal strength, $\mu = \sigma/\sigma_{\text{SM}}$ at 95% confidence level for the SM hypothesis is 8.3 (6.8).

Key words: ATLAS, LHC, Standard Model, New physics, Higgs bosons, Top quark, Yukawa-coupling

Acknowledgement

The way to PhD is a long journey require consistent effort and support. The completion of my thesis was possible with guidance and support of several people including my supervisor, colleagues, friends and family.

My first and big appreciation goes to my supervisor, Prof. Cunfeng Feng, for his marvelous supervision. Sincere gratitude is extended to his constructive feedbacks starting from day one, when I came to the China, all the way to my PhD. His continuous support and guidance provided me encouragement for a consistent endeavor that is necessary in a long journey to PhD. During the precious time under his supervision, I have not only learnt about Physics, but how to be a humble, clam and virtuous person. I would also like to thank my co-supervisor Prof. Bing Li for his dedicated support and guidance.

I greatly appreciate the support received through the collaborative work undertaken with the analysis group members Valentina Vecchio, Carlos Escobar, Fabio Cardillo, Nello Bruscino, Jesus Guerrero and Tanja Holm. We had very fruitful discussions about analysis every week even though we were in different time zone. It was really an intellectual collaboration. Its worthy here to acknowledge the ATLAS experiment at CERN for proving a chance to work with the largest collaborative efforts ever attempted in science.

I wish to extend my special thanks to Xuan Yang providing practical and valuable suggestions in the analysis. Other colleagues form Shandong, Rui Yuan, Ye Tian, Hengying Zhang, Tianting Wang, and Yanhong Yu you people make me feel like China as my second home. It truly has been very good time in the lab. I would like to thank Prof. ZHU Chengguang my instructor for ATLAS qualification task. It was really interesting to do practical work in the lab.

While at CERN, I also had great pleasure of working with Tahir Javid, Mehar Ali, M Bilal and Shahzad Ali, we have spent quality time together.

Once again sincere gratitude to my mentor and master supervisor Dr. Ashafq Ahamd for providing the work place at National Center for Physics(NCP).

I would like to acknowledge the Chinese Government Scholarship Council(CSC) for providing financial support throughout the PhD. Also to the Shandong university for accepting as me an international student and providing all the sources to complete the various projects.

Last but not least, I would like to thank my family for all their love and encouragement. For my parents, whose unconditional love and guidance are with me in whatever I pursue. You are always there for me.

Chapter 1 Introduction

The standard model (SM) of particle physics, represents our best understanding of physics phenomena at the most fundamental scales. It provides a unified picture for all known elementary particles, the building blocks of matter and the way they interact via three of the four fundamental forces. Over the decades, SM has been tested extensively by a broad variety of experiments. It is able to successfully explain almost all experimental results over a wide energy range, with a great precision. Its great predictive power was again remarkably exemplified by the discovery of Higgs boson in 2012 at CERN’s Large Hadron Collider (LHC).

However, the SM is not the ultimate theory of everything, and falls short of explaining several well-established observations: like explanation of what is dark matter, nor incorporate the gravitational force, or how neutrinos acquire mass. Modern high-energy physics experiments seek to probe the predictions of SM as precise as possible, and to search for new phenomena predicted by beyond the standard model (BSM) scenarios. The large hadron collider (LHC) is the world’s most powerful and largest accelerator, conceived to cover a broad physics programme. The ATLAS and CMS experiments observed the Higgs boson in 2012 at a mass of 125 GeV.

Being the heaviest elementary particle, top quark possess some unique properties, one of those is heaving strongest coupling with the Higgs boson. For the deeper understanding of the electroweak symmetry breaking mechanism and the underlying physics, precise measurements of Higgs properties is essential. The Higgs boson couplings to gauge bosons and fermions are precisely specified by the standard model. The study of top quark Yukawa coupling y_t to the Higgs boson, predicted in the SM to be close to unity, is well motivated and any deviation could provide valuable insights regarding possible BSM extensions. The recently observed [1] $t\bar{t}H$ process represents a privileged channel to probe y_t directly, without making any assumption about new physics. However, the $t\bar{t}H$ process is only sensitive to the magnitude $|y_t|^2$, not to the sign of this parameter. On the contrary, the associated production of Higgs boson and a single top quark, denoted tH, is the only process sensitive at leading order to the magnitudes as well as relative sign of top-Yukawa coupling.

The tHq event topology is characterised by two heavy objects – the top quark and the Higgs boson – plus a light-flavour quark (either d- or $\bar{u}$-quark), called spectator quark, and an extra soft b-quark (in most of the cases out of detector acceptance). The top-quark and Higgs-boson systems are produced in the central portion of the detector recoiling against each other: a semi-leptonic top-quark decay produces high-momentum electrons and muons that can be used to trigger the event. Higgs boson decays to vector bosons or τ leptons ($H \to WW^*, ZZ^*, \tau\tau$), which subsequently decay to light leptons ($l = e^{\pm}, \mu^{\pm}$), lead to a multi-lepton final state with comparatively small background contributions from other processes. Higgs boson decays to bottom quark–antiquark pairs ($H \to bb$) provide a larger event rate, albeit with challenging backgrounds from $t\bar{t}$ + jets production. The rare Higgs boson decays to two photons ($H \to \gamma\gamma$) result in easily triggered and relatively clean signals for both leptonic or fully hadronic top-quark decays, with backgrounds mainly from other production modes of the Higgs boson. The production of tWH involves three heavy objects and lacks the presence of forward activity: it does not exhibit the defining features of tHq events, while closely resembling the ttH topologies, having an identical final state.

There is no measurement in ATLAS yet. The CMS Collaboration searched for tHq production with a partial Run 2 dataset (i.e. an integrated luminosity of 35.9 fb^{-1} [23], assuming a positive or negative sign of the top-quark Yukawa coupling relative to its SM value, using all the relevant Higgs boson decay modes, and set limits on the observed (expected) cross-section of this process of 1.94 ($0.92^{+0.40}_{-0.27}$)pb for the SM hypothesis of a Yukawa coupling $y_t = +1$, and 0.74 ($0.53^{+0.24}_{-0.16}$) pb for the inverted Yukawa coupling (ITC) hypothesis $y_t = -1$. These results translate in an observed (expected) upper limit on the signal strength, $\mu = \sigma/\sigma_{\text{SM}}$, of 27 ($13^{+6}_{-4}$) for the SM hypothesis and 1 (0.75 $^{+0.34}_{-0.23}$) for the ITC hypothesis. An updated version of the ttH and tHq multi-lepton results by CMS (including hadronically decaying τ-lepton channels) and using full LHC Run 2 dataset (i.e. an integrated luminosity of 137 fb^{-1}) [2] measures $\mu_{tHq} = 5.7 \pm 2.7$ (stat.) $\pm$ 3.0 (syst.).

In this thesis, I will discuss the production of Higgs boson in association with single top quark in final state with two same-charge light-flavour leptons and no hadronically-decaying τ leptons (2LSS), as I was the main analyser of this channel. My contribution starts form the very first step, analysis framework development for mini ntuples production. Then I put my efforts on analysis region optimization using cut-and-count method. This analysis suffers from low statistics, from a difficult distinction to irreducible backgrounds it requires a complicated estimate of non-prompt and also charge flip backgrounds. I have performed detailed study on background estimation, testing various methods and techniques. I also completed the statistical analysis and fit results at the end.

The thesis is structured in the following way: Chapter 2 gives an introduction to the theoretical basis consisting, SM mainly focuses on the top quark and SM Higgs boson. Chapter 3 introduces the Large Hadron Collider and the ATLAS detector. Here I will also discuss the production quality control test, I performed to check the stability of small-strip thin gap chamber(sTGC) for the ATLAS new small wheel muon upgrade detector for high luminosity LHC. I have performed this work as my ATLAS qualification task. Chapter 4 contains a brief discussion on event generation, detector simulation and also explains the object definition and selection criterion in detail. In Chapter 5 there is detailed explanation on background estimation. Chapter 6 explains the systematic uncertainties and fit results. The thesis concludes with a summary and outlook in Chapter 7.

Chapter 2 The Standard model of particle physics

The universe as we understand it is made up of fundamental particles that interact with one another in accordance with a set of laws of nature. The standard model (SM) of particle physics, summarizes our current understanding of fundamental particles and their interactions. The SM is incredibly effective since its predictions agree with the results of tests conducted over many years by physicists. The theory has existed in its current form since the 1970s, but it wasn't until 2012 that the Higgs boson, the final piece of its particle puzzle, was found at the LHC. There are some fundamental questions which are not addressed by current SM. Some of these are theoretical in nature, while others are experimental findings in high energy particle physics and astronomy that appear to be inconsistent with the SM. The goal of the analysis presented in this thesis is to searches for process of the production of a Higgs boson in association with a single top quark. This process is not only relevant for the stability of the Higgs potential but also sensitive to the presence of new physics.

In this chapter, the theoretical background necessary for the searches for tH production at the LHC is introduced. Beginning with an overview of the standard model, the Higgs mechanism and Yukawa couplings responsible for the masses of SM particles are introduced in section 2.3, which then goes on to define the theoretical framework behind the fundamental forces. Section 2.4 concentrate on the theoretical description of top quark and Higgs boson properties in the context of the Standard Model. Also contains a brief explanation of the production and decay channels that were employed to study their coupling.

2.1 Overview of the standard model

Three of the four fundamental forces are successfully described by the Standard Model. After decades of study to precisely characterize interactions between fermions and photons, the electromagnetic force was first conceptualized historically within the framework of quantum electrodynamics (QED). Later, under the electroweak (EWK) theory, QED and the weak force were unified. The framework of quantum chromodynamics(QCD) was used to describe the strong force. Since there is currently no proper unification of the SM with the General Theory of Relativity, only the gravitational force is excluded from the SM. The gravitational force's interaction strength is substantially weaker than that of the other forces in the context of particle physics, and its possible impact is negligible. The SM itself is a renormalizable and gauge invariant quantum field theory that combining the EWK and QCD in a single theory with the non-abelian symmetry:

$$SU(3)_C \otimes SU(2)_L \otimes U(1)_Y \tag{2.1}$$

The invariance under 3-dimensional special unitary group $SU(3)_C$ results in the presence of massless gluons (g), mediators of the strong force described by quantum chromodynamics (QCD), while the $SU(2)_L \otimes U(1)_Y$ is associated to the theory of EWK interactions.

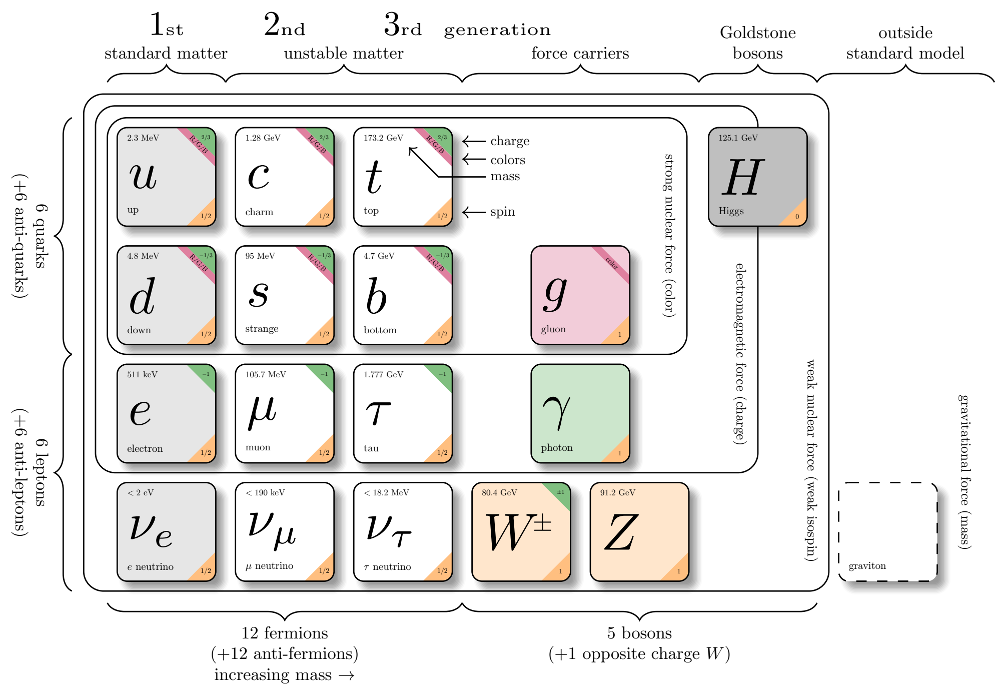

Figure 2.1: Elementary particles of the Standard Model

Figure 2.1 provides a summary of the fundamental characteristics of the particles in the standard model. They are distinguishable as fermions and bosons. Fermions are particles with a half-integer spin where as bosons possess integral spin. Based on their masses, decay and couplings to the force carriers, Fermions are divided into two main groups known as quarks and leptons. Each group consists of six particles, which are related in three generations. All known stable matter in the universe is made up of only first generation fermions. The second and third generation fermions are unstable and quickly decay to more stable lighter particles. Fermions of each subsequent generation are more massive than the last.

The six lepton are paired in three generations, each generation contains one charged lepton (electron, muon, or tau) and one corresponding neutrino (electron neutrino, muon neutrino, or tau neutrino). Leptons are not subject to the strong interaction as they have no color charge. The charged leptons experience electromagnetic and weak forces while the electrically neutral leptons (neutrinos) interact with matter only via the weak force.

The six quarks (other group of fermions) are also paired in three generation, each generation contains one up-type quark, with $+2/3$ electric charge (up, charm, or top) and one down-type quark with $-1/3$ electric charge (down, strange, and bottom). Compared to the leptons they carry the color charge and undergo both the strong and weak nuclear interactions. Each flavor of quarks can have three different colors: red (R), green (G), blue (B), which is analogous to the primary colors in nature. Due to a phenomenon known as color confinement, quarks are never found in isolation and are always bound to other quarks in composite states called hadrons. All observable quark final states should have white color, eg. consists of three colors (RGB) known as Baryons or consists of color-anticolor pair known as Mesons. Bound states of four and five quarks also exist, called tetraquarks and pentaquarks.

Bosons having integral spin are the second fundamental class of elementary particles. There are two types of bosons in the Standard Model (SM): spin 0 bosons known as scaler boson, of which the Higgs boson is the only one known and Spin 1 bosons known as vector (gauge) bosons. The gauge bosons are the force carriers of fundamental interactions. The photon is the mediator of the electromagnetic force and couples to charged particles while the gluon is the mediator of the strong nuclear force and couples to particles with color charge. Both photon and gluon are massless particles. The three weak bosons (W^+, W^-, and Z) are the mediators of the weak nuclear interaction.

The most elusive particle of the Standard Model is the Higgs Boson, the only scalar (spin-0) boson. Its existence is a consequence of unification of the electroweak (EWK). The fermions, W-bosons, and Z-bosons would all lack mass if the Higgs boson had no part in this process. As a result, it can be argued that the Higgs "gives mass" to the Standard Model particles. It couples to all massive particles in the Standard Model.

2.2 Quantum chromodynamics

Quantum chromodynamics (QCD) is the theory in the SM describing strong interactions. The QCD is a gauge theory symmetric under the 3-dimensional special unitary group, $SU(3)_C$. The conserved charged related to this symmetry is the color charge, so the quark fields have a fundamental representation under this group since only quarks have color charge. The free-field Lagrangian density for massless spin 1/2 quarks can be written as:

$$\mathcal{L} = \bar{\psi}(x) i\gamma^{\mu}\partial_{\mu}\psi(x) \tag{2.2}$$

where $\psi(x)$ is a $SU(3)_C$ triplet for the quark fields. In color space the Lagrangian is invariant under $SU(3)_C$ transformations:

$$\psi(x) \rightarrow e^{ig_s \frac{\lambda_a}{2}\theta_a(x)}\psi(x) \tag{2.3}$$

where g_s is the QCD coupling strength, $\frac{\lambda_a}{2}$ (a = 1,...,8) is the Gell-Mann matrices that generate $SU(3)_C$ and θ_a set of arbitrary parameters. It is important to introduce the covariant derivative in order to maintain the Lagrangian density's gauge invariance under such a transformation.

$$D_{\mu} = \partial_{\mu} - ig_s G_{\mu}^{a}(x)\frac{\lambda_a}{2} \tag{2.4}$$

$G_{\mu}^{a}(x)$ is the the vector field of gluons that mediate the strong interaction. The kinetic energy term of the gluon field $\frac{1}{4}G_a^{\mu\nu}G_{\mu\nu}^{a}$, should also be included to complete the Lagrangian density, where the color field tensor $G_{\mu\nu}^{a}$ is:

$$G_{\mu\nu}^{a} = \partial_{\mu}G_{\nu}^{a} - \partial_{\nu}G_{\mu}^{a} + g_s f^{abc}G_{\mu}^{b}G_{\nu}^{c} \tag{2.5}$$

with f^{abc}, the $SU(3)_C$ group structure constants. The full QCD Lagrangian can be written as:

$$\mathcal{L}_{QCD} = \bar{\psi}(x) i\gamma^{\mu}\partial_{\mu}\psi(x) - g_s\bar{\psi}(x)\gamma^{\mu}\frac{\lambda_a}{2}\psi(x)G_{\mu}^{a} - \frac{1}{4}G_a^{\mu\nu}G_{\mu\nu}^{a} \tag{2.6}$$

The first term describes the propagation of quarks in free fields, the second term depicts quark-gluon interactions, and the third word is the free kinetic term for gluon fields. The gluon fields and their interactions with the quarks were introduced by requiring the local gauge invariance. It is important to note, however, that the introduction of an explicit mass term $G^a_\mu G^\mu_a$ in Eq. 2.6 would break the gauge invariance of the Lagrangian.

2.3 Electroweak theory

The electroweak theory primarily arisen as a result to develop a self-consistent gauge theory for the weak force, in analogy with quantum electrodynamics (QED). Sheldon Lee Glashow, Abdus Salam, and Steven Weinberg [3, 4, 5] each independently founded that they could build a gauge-invariant theory of the weak force as long as they also took the electromagnetic force into account, that leads to the unification of electromagnetic and weak force. The $SU(2)_L \otimes U(1)_Y$ group is associated to electroweak interactions. Since left and right-handed particles couple differently through the EWK interaction, the projection of matter fields to their respective chiral components is considered:

$$\Psi_L = \frac{1-\gamma^5}{2}\begin{pmatrix}\psi \\ \psi'\end{pmatrix} = \begin{pmatrix}\psi_L \\ \psi'_L\end{pmatrix} \tag{2.7}$$

$$\psi_R = \frac{1+\gamma^5}{2}\psi \tag{2.8}$$

$$\psi'_R = \frac{1+\gamma^5}{2}\psi' \tag{2.9}$$

Where ψ and ψ' are the fermion fields, represent either up- and down-type quarks, or a neutrino and a lepton. As for strong interactions, the electroweak theory is introduced by imposing a local gauge invariance of a $SU(2)_L \otimes U(1)_Y$ group. Four gauge fields are used to characterize the four electroweak theory mediators ($Z, W^\pm$ and γ). The gauge invariance under the $SU(2)_L$ results in the 3 gauge fields $W^i_\mu(i = 1; 2; 3)$, acts only on the left-handed fermions. The isospin quantum number for left-handed fermions is $I_3 = \pm 1/2$ (for neutrinos and up-type quarks $I_3 = +1/2$ and for electrons, muons, taus, and down-type quarks $I_3 = -1/2$. While the gauge invariance of the $U(1)_Y$ group results in the single gauge field B_μ, that interacts with both left and right-handed fermions. The relationship between the conserved quantum numbers, isospin I and hypercharge Y, can be determined by the Gell-Mann-Nishijima formula:

$$Q = I_3 + Y \tag{2.10}$$

Consequently, the Lagrangian density of the electroweak theory can be expressed as:

$$\mathcal{L} = i\bar{\Psi}_L\gamma^\mu D_\mu \Psi_L + i\bar{\psi}_R\gamma^\mu D_\mu \psi_R + i\bar{\psi}^{'}_R\gamma^\mu D_\mu \psi^{'}_R \tag{2.11}$$

The covariant derivatives D_μ is defined as:

$$D_\mu = \partial_\mu - igW^i_\mu \frac{\sigma_i}{2} - ig^{'}\frac{Y}{2}B_\mu \tag{2.12}$$

where g and $g^{'}$ are the coupling constant of the $SU(2)_L$ and $U(1)_Y$ that define the strength of the interactions. The physical mass eigenstates of the W and Z bosons, as well as photons, can be connected to the four degrees of freedom introduced by the $SU(2)L \otimes U(1)_Y$ local gauge symmetry:

$$W^\pm_\mu = \frac{1}{\sqrt{2}}(W^1_\mu \mp iW^2_\mu) \tag{2.13}$$

$$\begin{pmatrix} W^3_\mu \\ B_\mu \end{pmatrix} = \begin{pmatrix} cos\theta_W & sin\theta_W \\ -sin\theta_W & cos\theta_W \end{pmatrix} \begin{pmatrix} Z_\mu \\ A_\mu \end{pmatrix} \tag{2.14}$$

where A_μ describes the photon field of electromagnetism and θ_W is the Weinberg angle which parametrize the liner superposition. The relevant strength tensor is presented in order to construct the kinetic terms for the gauge field.

$$B_{\mu\nu} = \partial_\mu B_\nu - \partial_\nu B_\mu \tag{2.15}$$

$$W^i_{\mu\nu} = \partial_\mu W^i_\nu - \partial_\nu W^i_\mu + g\epsilon^{abc}W^b_\mu W^c_\nu \tag{2.16}$$

Now, the final electroweak Lagrangian density can be expressed as follow:

$$\mathcal{L} = i\bar{\Psi}_L\gamma^\mu D_\mu \Psi_L + i\bar{\psi}_R\gamma^\mu D_\mu \psi_R + i\bar{\psi}^{'}_R\gamma^\mu D_\mu \psi^{'}_R - \frac{1}{4}B^{\mu\nu}B_{\mu\nu} - \frac{1}{4}W^{\mu\nu}_i W^i_{\mu\nu} \tag{2.17}$$

Since a mass term would connect the left- and right-handed fields and violate the gauge symmetry, it is forbidden to include one for the gauge fields (gauge bosons) and fermions. However, the experiment's findings demonstrate that fermions and gauge bosons ($W^\pm, Z$) do have masses. The mechanism that creates mass for the fields will be introduced in the section that follows.

2.3.1 Electroweak spontaneous symmetry breaking

As discussed in previous section, any fermion or gauge field would break gauge invariance if a mass term were added. As a result, all fermions and gauge bosons are massless in the QCD and electroweak Lagrangians defined by Eqs. 2.6 and 2.17. However, this stands in stark contrast to the experimentally observed non-zero fermion, W, and Z boson masses. The answer to this issue was put up by Englert and Brout and Higgs based on introduction of new degrees of freedom and subsequent spontaneous breaking of the $SU(2)_L \otimes U(1)_Y$ symmetry.

A complex weak iso-doublet Φ is used to introduce the additional degrees of freedom. Before symmetry breaking, the Higgs Lagrangian is described as:

$$\mathcal{L} = (D_\mu \Phi)^\dagger (D^\mu \Phi) - V(\Phi^\dagger \Phi) \tag{2.18}$$

where the potential $V(\Phi^\dagger \Phi)$ is defined as:

$$V(\Phi^\dagger \Phi) = -\mu^2 \Phi^\dagger \Phi + \lambda (\Phi^\dagger \Phi)^2; \mu^2, \lambda > 0 \tag{2.19}$$

The hypercharge corresponding to the Higgs filed is $Y_\Phi = 1/2$. The covariant derivative D_μ is same as in equation 2.12. The shape of Higgs potential results in a degenerate minimum at:

$$\Phi_0^\dagger \Phi_0 = -\frac{\mu^2}{2\lambda} = \frac{v^2}{2}; \mu^2 > 0 \tag{2.20}$$

where v describes the vacuum expectation value of the scaler potential. The symmetry is explicitly broken once a particular ground state $\frac{1}{\sqrt{2}}\begin{pmatrix} 0 \\ v \end{pmatrix}$ is selected from the set of degenerate minima, but the Lagrangian remains gauge invariant. The field expansion around its minimum can be expressed as:

$$\Phi(x) = \frac{1}{\sqrt{2}} \begin{pmatrix} 0 \\ v + H(x) \end{pmatrix} \tag{2.21}$$

where the field $H(x)$ describes the field excitations around the minimum. With the new field defined, the resulting Lagrangian for the BEH mechanism can be written as:

$$\begin{aligned} \mathcal{L} = \;& \frac{1}{2}\partial_\mu H \partial^\mu H - \lambda v^2 H^2 - \lambda v H^3 - \frac{1}{4}\lambda v H^4 \\ & + \frac{1}{4} g^2 v^2 W_\mu^- W^{+\mu} + \frac{1}{8}(g^2 + g^{'2}) v^2 Z_\mu Z^\mu \\ & + \frac{1}{8}(2vH + H^2)(2g^2 W_\mu^- W^{+\mu} + W_\mu^- W^{+\mu} Z_\mu Z^\mu) \end{aligned} \tag{2.22}$$

The first line of Eq. 2.22 describes the Higgs field corresponds to a new physical massive particle, the Higgs boson, with mass $m_H = v\sqrt{2\lambda}$. The second line introduces the mass terms of the weak interaction bosons and the third line presents the interaction of the weak bosons $W^{\pm}$ and Z with the Higgs boson. The masses of the $W^{\pm}$ and Z bosons can be obtained are follow:

$$m_W = gv/2 \tag{2.23}$$

$$m_Z = \sqrt{g^2 + g'^2}v/2 \tag{2.24}$$

As the vacuum expectation value v is related to energy scale of the EWSB, it can be measured from Fermi constant:

$$v = \sqrt{\frac{1}{2G_F}} \approx 246\text{GeV} \tag{2.25}$$

So far it is described how the BEH mechanism can generate the gauge boson masses. However, unless more modifications are made to the SM Lagrangian, fermions remain to be massless.

2.3.2 Yukawa couplings and quarks in the EW theory

Fermions can obtain the mass by incorporating interaction term between fermions and the Higgs filed. This term is know as the Yukawa coupling. For Leptons:

$$\begin{aligned} \mathcal{L}^l_{Yuk} = & \sum_l -y_l \bar{L}^{(l)} \Phi_U l_R + h.c \\ = & \sum_l m_l \bar{l}l - \frac{y_l}{\sqrt{2}} \bar{l}lH \end{aligned} \tag{2.26}$$

where, in addition to the mass terms, leptons interact with the Higgs boson, with the Yukawa coupling which is proportional to the mass of the leptons $y_l = \sqrt{2}m_l/v$. Quarks can also be added into the EW theory:

$$\mathcal{L}^q_{Yuk} = \sum_q -m_q \bar{q}q - \frac{y_q}{\sqrt{2}} \bar{q}qH \tag{2.27}$$

where q represent the six flavour of quarks. In contrast to the lepton, the down-type quarks mass eigenstates q do not correspond to the weak eigenstates q_0 but are related through the unitary matrix known as Cabbibo-Kobayashi-Maskawa (CKM) matrix:

$$\begin{pmatrix} d_0 \\ s_0 \\ b_0 \end{pmatrix} = \begin{pmatrix} V_{ud} & V_{us} & V_{ub} \\ V_{cd} & V_{cs} & V_{cb} \\ V_{td} & V_{ts} & V_{tb} \end{pmatrix} \begin{pmatrix} d \\ s \\ b \end{pmatrix}$$

The matrix can have a complex phase that leads to CP violation. Then, the weak eigenstates appear in the interaction of quarks with the weak bosons:

$$\mathcal{L}_q = \sum_{q=u,c,t} \bar{L}_0^q (iD_\mu \gamma^\mu) L_0^q + \sum_{q=u,c,t,d,s,b} \bar{q}_{0R} (iD_\mu \gamma^\mu) q_{0R} \tag{2.28}$$

The weak boson decays are primarily modified by this distinction between mass and weak eigenstates. There would only be three possible couplings with quarks if they were similar. All combinations of the up and down quark states are possible as a result of the flavor mixing. The relevant element of the CKM matrix V_{ij} determines the coupling's amplitude, and are free parameters of the theory, that are to be measured experimentally. With a ratio of roughly $20:1$, the largest mixing is between d and s quarks while the top for example, decays almost completely to the bottom quark.

2.4 Coupling of a top quark to Higgs boson

Over the past several decades, many studies have consistently tested the Standard Model theory. The most recent Higgs boson measurements at ATLAS and CMS [7, 8], exhibit remarkable agreement with SM predictions, and neither collaboration has discovered any notable deviations from this theory. Despite the SM's enormous success, many indications suggest that it is not a complete theory that can account for everything in the universe. What exactly are dark energy and dark matter? What precisely determines the masses of each fermion? Why have right-handed neutrinos never been observed? Can we combine other forces in the same way that electromagnetic and the weak force have been combined? Most of these questions suggested Beyond the Standard Model extensions include massive fermions and bosons, additional Higgs fields, and other particles that would interact with the Standard Model Higgs.

The discovery of the Higgs has ushered in a new era of precision measurement in collider physics. In many situations, we may get signs of the existence of new particles by closely investigating interactions that are particularly sensitive to the injection of new physics. Higgs interactions are very sensitive to new physics because of the Higgs interact to all massive particles. As a result, they can act as a good bellwether for phenomena beyond the standard model. Through its decays, a Higgs boson with a mass of around 125 GeV enables experimenters to study the Higgs boson couplings to numerous SM particles. The probability of the Higgs boson decaying to a specific final state known as the Higgs boson branching fraction (BR), is depicted in Fig. 2.2 (left), as a function of Higgs boson mass.

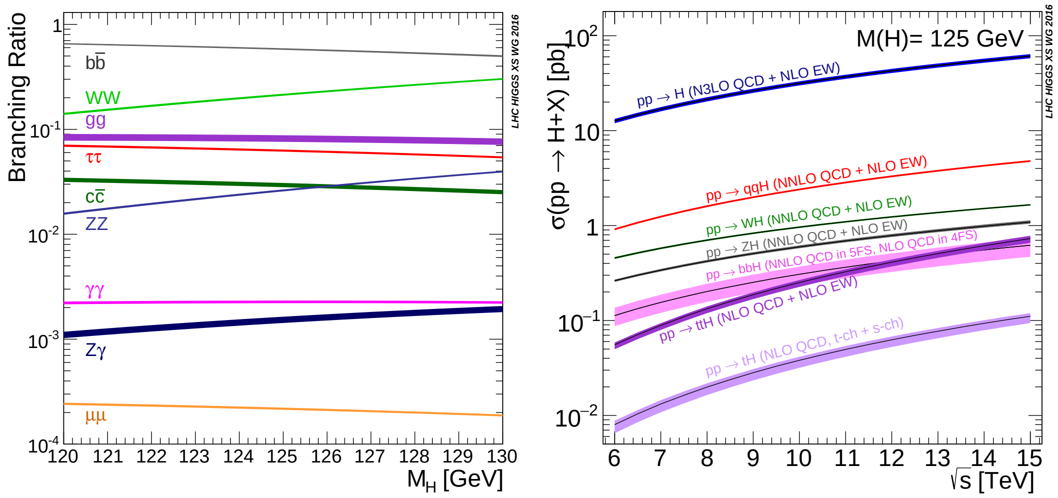

Figure 2.2: Left: Branching ratios of the dominant Higgs decays as a function of the Higgs mass M_H. Right: Main production channels of the Higgs boson as a function of the collision energy. The figures are taken from [10]

At the LHC, the Higgs boson is produced in several production channels. Gluon-gluon fusion (ggF), vector boson fusion (VBF), vector-boson associated Higgs production (VH), and top-associated Higgs production are predominant Higgs production modes. Their cross-section as a function of the center-of-mass energy is displayed in figure 2.2 (right). The feynman diagrams for these production are presented in figure 2.3.

The top quark is the heaviest particle in the Standard Model. It was observed in 1995 at the Tevatron [9]. It has the most distinctive features among the quarks due to its large mass, which is appropriately around 173.3 GeV. Its shorter lifetime is caused by the fact that it is substantially heavier and can decay into a true W boson. As a result, it is the only quark which does not form bound states. It decays directly into the bW final state the relevant CKM term $|V_{tb}| \approx 1$. Additionally, the top quark's Yukawa coupling to the Higgs boson is nearly one, which is much higher than for any other quark. Due to its dominant role in

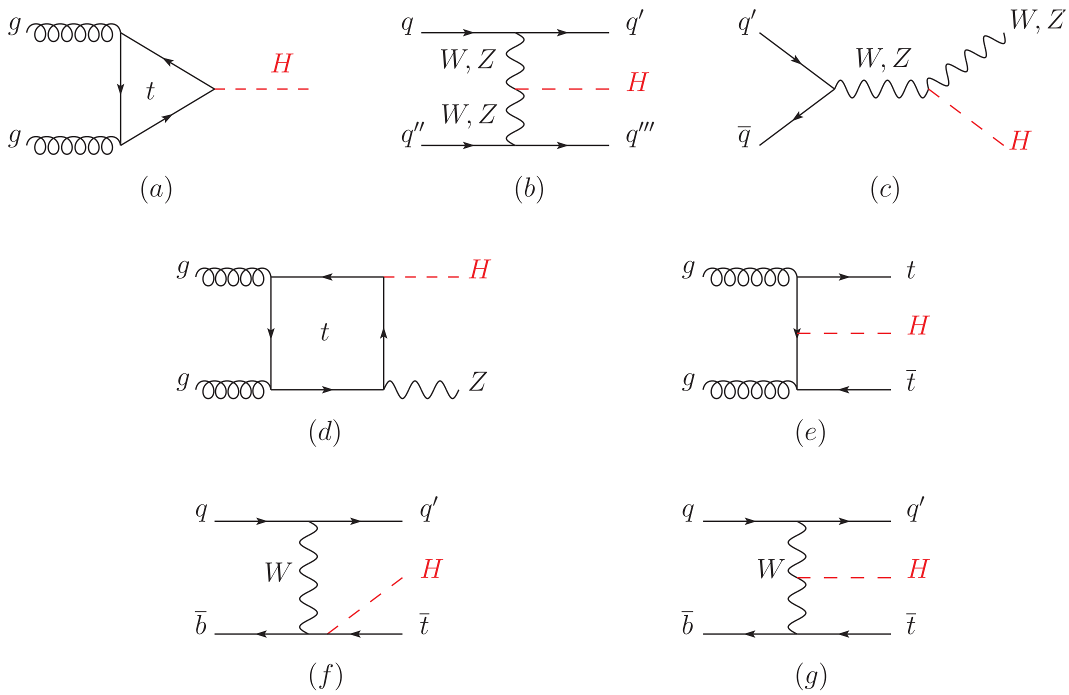

Figure 2.3: Main leading order Feynman diagrams contributing to the Higgs boson production in (a) gluon fusion, (b) Vector-boson fusion, (c) Higgs-strahlung (associated production with a gauge boson at tree level from a quark-quark interaction), (d) associated production with a gauge boson, (e) associated production with a pair of top quarks, (f-g) production in association with a single top quark.

quark/fermion loops, it is crucial to understand it in order to interpret some of the Higgs' properties accurately. Three main avenues can be employed to analyze any Higgs coupling: Higgs emission, Higgs decay, and top quark contribution to loops involving the Higgs. The top quark is too massive to be a product of Higgs decay. It can be studied from the loops. Any such measurement, however, inevitably involves underlying theory assumptions. Other particles that the SM does not predict may also contribute to the Higgs modes involving a loop or may even modify how other particles are coupled to the Higgs. As a result, only Higgs emission from a top quark can offer a direct measurement of the top Yukawa coupling. The Higgs associated production with a pair of top quark ($t\bar{t}H$) is highest cross-section of such process.

Although subdominant and much more difficult to observe, the Rarer production mode Higgs boson generation in association with a single top quark (tH), can provide important information, particularly with reference to the top Yukawa coupling sign. It is because of the destructive interference between two large contributions, one where the Higgs boson couples to a space-like W boson (tWH) and the other where it couples to the top quark (tHq).

Chapter 3 The ATLAS experiment at LHC and sTGC quality control

The analysis presented in this thesis is performed using proton-proton collisions data recorded by the ATLAS detector at Large Hadron Collider (LHC) during 2015-2018. In this chapter, I will discuss the ATLAS experiment which is one of the four main experiment at LHC. In order to precisely study the Higgs sector and to extend the sensitivity to new physics to the multi-TeV range, extensive and massive upgrade program of the ATLAS experiment is underway. The New Small Wheels (NSW) is a part of major muon spectrometer upgrade. NSW use novel small-strip Thin Gap Chambers (sTGC) which are built in SDU China, one of the construction sites. I will also discuss the production quality control test performed to check the stability of sTGC in this chapter. It was my ATLAS qualification task.

3.1 The Large Hadron Collider

The Large Hadron Collider (LHC) at the laboratories of the European Organization for Nuclear Research (CERN) is the world’s largest and most powerful particle accelerator located near Geneva on the border between France and Switzerland. About 100 meter below the ground, it consists a giant 27 kilometre ring of superconducting magnets with a series of accelerating structures. At LHC, both protons and heavy ions are collided, most of the following discussion focuses on proton-proton collisions.

A schematic view of LHC in a complex chain of particle accelerators is shown in Figure 3.1. Before the particles collides in main LHC, they have to be per-accelerated by various smaller accelerators. The journey start from simple hydrogen gas cylinder. Electrons are stripped off by ionization of hydrogen atoms and the remaining protons are first accelerated in liner accelerator LINAC-2 up to kinetic energy of 50 MeV. Travelling at one-third the speed of light the protons are injected in to the proton synchrotron booster (PSB). The PSB, boosts the energy of protons to 1.4 GeV by applying pulsed electric filed each time they reach a certain point. Gaining 91.6 % of speed of light, protons enters the proton synchrotron. Strong magnetic filed at right angle to the direction of motion bends them to the circle of 628 meter in circumference. Here they gain energy about 25 GeV and speed up to 99.9 % of speed of light. Finally, injected into the Super Proton synchrotron (SPS) where they are accelerated to 450 GeV.

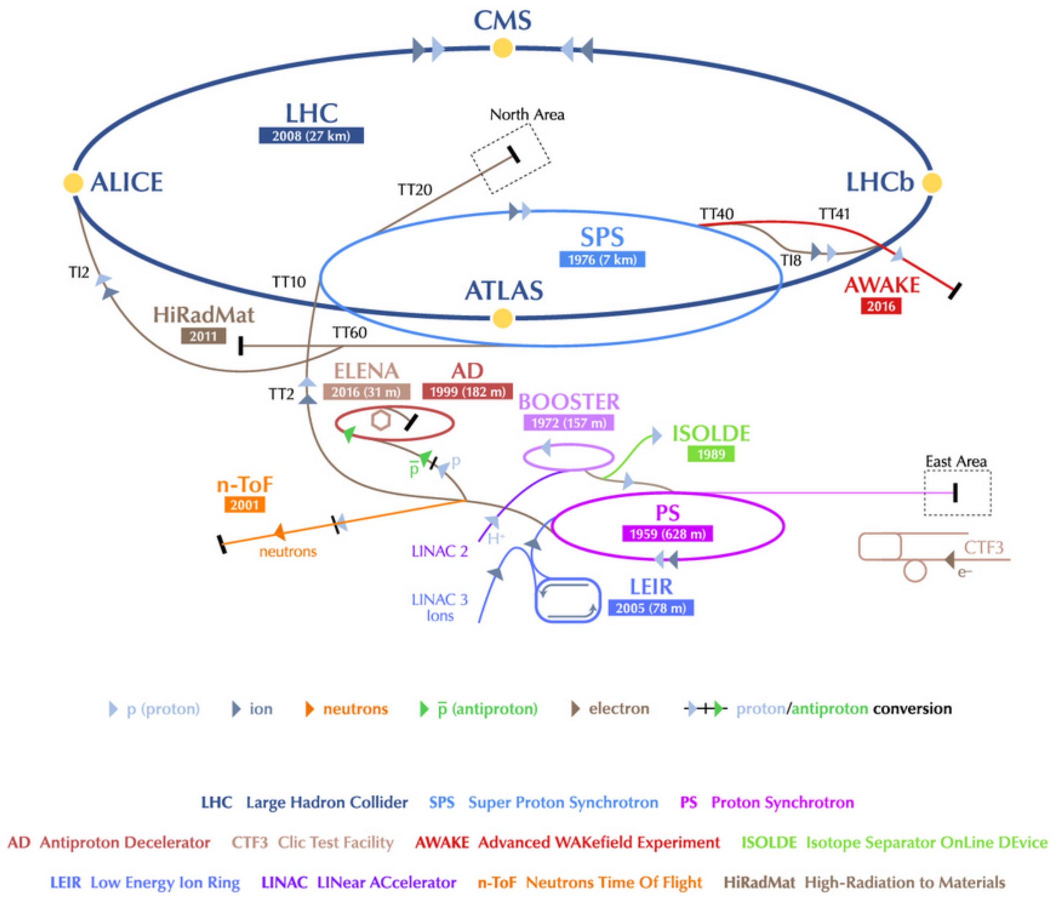

Figure 3.1: The CERN accelerator complex. The chain of proton starts from the LINAC-2, passing through the Booster, PS, and SPS injected to the LHC. [11]

Now at this stage, the protons have got enough energy to be injected into the main LHC. The injection is done via two transfer lines in separate beam pipes where circulated in opposite directions, clock wise and anti clockwise. The design energy at LHC is to accelerate each beam at 7 TeV. With this much energy the beam completes over 11,000 circles around the 27 km ring in each second. The protons already approaching the limiting speed of light in PS, the added energy manifest if self as increasing mass of protons. So in LHC protons are 7000 time heavies then they are at rest. They are guided in circular path around accelerator ring by a strong magnetic field of strength 8.3 T maintained by 1232 superconducting dipole magnets. The distribution system of liquid helium cools the magnets to 1.85 K –a temperature colder than outer space. Protons at the LHC are accelerated by radio-frequency (RF) cavities (eight per beam) located along the collider ring, operating at 400 MHz with a 5 MV/m gradient. Just before the collision, additional 392 quadrupole magnets are used to focus the beams of 2808 bunches, each bunch contains around 10^{11} protons.

The beams are made to collide at four main interaction points where the four major experiments are established.

- ATLAS —A Toroidal LHC Apparatus
- CMS —Compact Muon Solenoid
- ALICE —A Large Ion Collider Experiment
- LHCb —LHC beauty experiment

Both the ATLAS and CMS are multi-purpose experiments and were build to answer open questions in the particle physics, one famously being the existence of the theorized Higgs particle, that was confirmed in July 2012. Other research goals of CMS and ATLAS are the search for physics beyond the Standard Model and supersymmetric particles. Although they have the same physics goals, the two experiments are established in a different manner, as to be able to confirm each other's results independently. ALICE was constructed to study the heavy ions collision and search for evidence of the quark-gluon plasma. LHCb focuses on studying the physics of b-quarks, particularly the CP violation in b-hadrons.

Along with the centrer of mass energy, the instantaneous luminosity is another important parameter of colliders. For a particular process, number of events generated per second in the LHC collisions is given by:

$$N_{event} = \mathcal{L} \times \sigma_{event} \tag{3.1}$$

Where $\mathcal{L}$ is the instantaneous luminosity and σ_{event} is the cross section of the process under study. The instantaneous luminosity can be defined in-terms of beam parameters:

$$\mathcal{L} = \frac{f_{rel} N_b^2 n_b \gamma_r}{4\pi\epsilon_n \beta^*} F \tag{3.2}$$

Where f_{rev} is the machine revolution frequency; N_b is the typical number of protons per bunch; n_b is the number of colliding bunch pairs, γ_r is the relativistic factor. F is a geometric luminosity reduction factor that accounts for the crossing

Table 3.1: Integrated luminosity delivered by LHC, recorded by ATLAS, and certified to be good quality data during stable beams for pp collisions at $\sqrt{s}$ = 13 TeV in 2015-2018. [12]

Integrated Luminosity (fb^{-1})	2015	2016	2017	2018	Cumulative
LHC Delivered	4.0	38.5	50.2	63.4	156
ATLAS Recorded	3.9	35.6	46.9	60.6	147
Good for Physics	3.2	33.0	44.4	58.5	139

angle at the interaction point. For head on collision the value of the factor F is 1 and it decreases with increase in the crossing angle. The factor $\epsilon_n\beta^*$ in denominator directly related to the beam size at the interaction point. By integrating over the data-taking time, the amount of data delivered by a collider can be measured in terms of the total integrated luminosity: $L = \int \mathcal{L}dt$ measured in unit fb^{-1}. Analysis presented in this thesis, uses data recorded by ATLAS during Run-II form 2015 to 2018, which correspond to total integrated luminosity 139.0 fb^{-1} as shown in Figure 3.2.

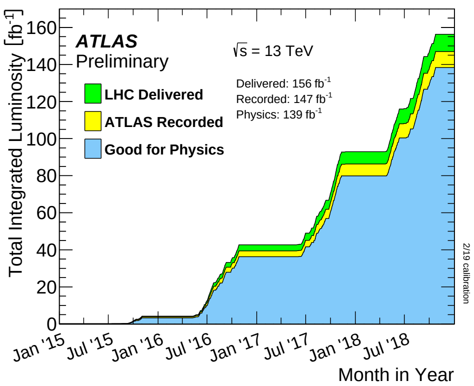

Figure 3.2: Cumulative luminosity versus time delivered by LHC (green), recorded by ATLAS (yellow), and certified to be good quality data (blue) during stable beams for pp collisions at $\sqrt{s}$ = 13 TeV in 2015-2018 [13]

3.2 The ATLAS Detector

The ATLAS detector is one of the two general purpose particle detectors placed at the LHC. It is designed to study the SM and Beyond the Standard

Model (BMS) Physics that includes flavour physics, QCD, electroweak interactions and new physics processes from high precision measurements to searches for new phenomena at TeV scale. In order to exploit these goals, it is the world's largest detector ever constructed for a particle collider with 25m in diameter, 44m cylindrical length and overall weight about 7000 ton.

Symmetric around the interaction point which covers nearly 4π in solid angle, it is a collection of sub-detectors, magnets and supporting infrastructure. The sub-detectors are arranged in concentric layers around the beam pipe. A schematic view of the detector is shown in Figure 3.3. Starting from the point of interaction the particles emerging from the p-p collisions firsts interact with the inner detector (ID) responsible for the precise measurement of their transverse momentum and charge. Then the calorimeter system where most of the particles deposit their energy and stop here except for muons and neutrinos. The outermost sub-detector is the Muon Spectrometer (MS) provide tracking and triggering of muons.

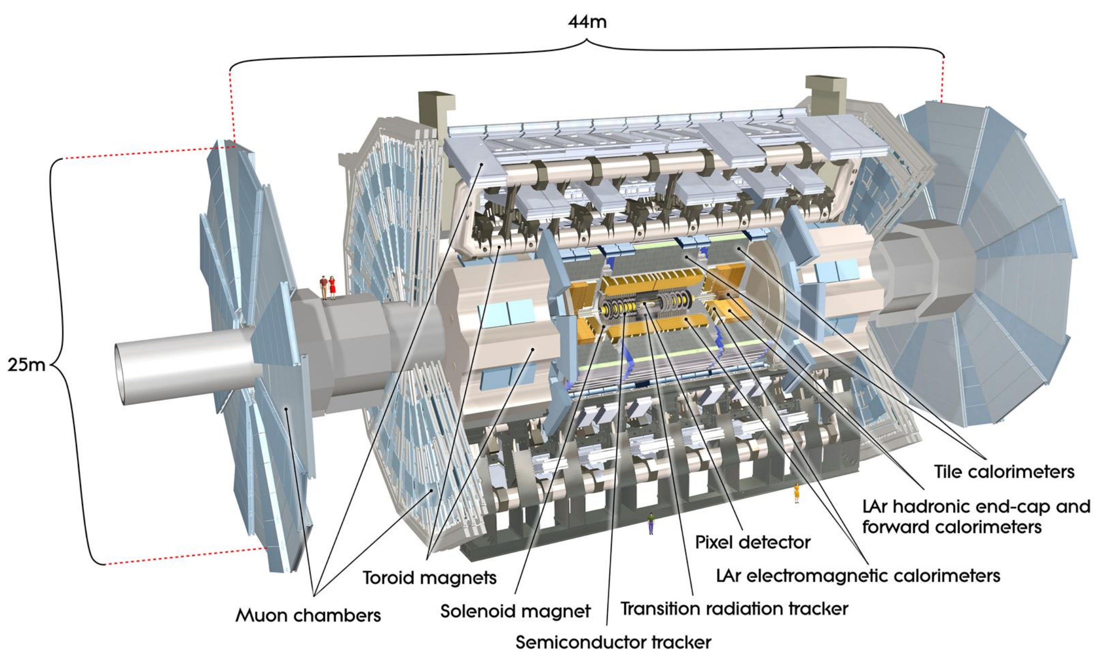

Figure 3.3: Cut-away view of the ATLAS detector [14]. The subdetectors are indicated and labeled.

3.2.1 ATLAS coordinate and Variables

This subsection briefly summarised the coordinate system and nomenclature used to describe the ATLAS detector since they are used repeatedly throughout this thesis. The nominal interaction point in the center of detector is set as origin of the coordinate system. Along the beam direction is the z-axis which transverse to the x-y plane. The positive x-axis points from interaction point to the center of LHC ring, where as the upwards from IP is positive y-axis. The transverse momentum $p_T = \sqrt{p_x^2 + p_y^2}$, the transverse energy $E_T = \sqrt{p_T^2 + m^2}$, and the missing transverse energy $E_T^{miss} = -|\Sigma_i \vec{p_T}^i|$ are defined in the x-y plane. The transverse plane is important in kinematics variables description mainly for two reasons. First, the transverse momentum of all particles produced in the p-p interaction has to sum up to zero. Second, the transverse momentum of charged particles measured directly from the curvature of the track due to solenoidal magnetic field of the inner detector.

As the ATLAS detector is cylindrical in shape so, it is also convenient to use cylindrical coordinates. In this cylindrical system, ϕ being the azimuthal angle defined in the transverse x-y plane around the beam axis where as polar angle θ is measured between the beam axis and transverse plane. However, using θ is not always practical due to large dependence of the number of particles produced on the angle. Most of the particles produced closer to the beam-line. So instead of the polar angle θ, the pseudorapidity η is mostly used , which is defined as:

$$\eta = -\ln(\tan\frac{\theta}{2}) \tag{3.3}$$

The small $|\eta|$ values are referred as the central region and large values of $|\eta|$ as forward region. The pseudorapidity is a low mass approximation of the rapidity y defined in equation 3.4. For $p \gg m$ and $\theta \gg 1/\gamma$ (where γ is the relativistic factor) the pseudorapidity η is approximately equal to the rapidity y:

$$y = \frac{1}{2}\ln(\frac{E + p_z}{E - p_z}) \tag{3.4}$$

Under a Lorentz boost along z-axis, the difference in pseudorapidity $\Delta\eta$, is an invariant quantity. This property is useful in hadron colliders, since the partons (e.g. quarks or gluon) in protons carry fractions of the incoming proton momentum and thus have unknown longitudinal momenta. Furthermore, interactions rarely have their center-of-mass frame coincident with the detector rest frame due to the composite nature of the colliding protons. The angular distance between two physics objects defined in pseudorapidity-azimuthal angle space is given by:

$$\Delta R = \sqrt{(\Delta\eta)^2 + (\Delta\phi)^2} \tag{3.5}$$

Another important set of variables is defined in the context of the particle tracks. Due to a finite resolution of the detector, the particle originating in the collision vertex are reconstructed with some finite distance from it. This distance is parameterized through impact parameters. In order to define these parameter, a point of the closest approach of the track to the vertex in the transverse plane is established. The transverse impact parameter d_0, is the point of closest approach to the z-axis in the x-y plane, where as z_0 referred as longitudinal impact parameter, is the z-coordinate at the point of closest approach to the z-axis.

3.2.2 The Inner detector

Up to thousands of particles emerge from the collision point every 25 ns, results in a very large track density in the detector. In order to achieve good momentum and vertex resolution, the inner detector being closet to the interaction point should have good granularity along with the great resistance to radiation damage. Pixel and silicon microstrip (SCT) trackers are characterized by high granularity to cope with higher occupancy and the Transition Radiation Tracker (TRT) based on gaseous drift tube technology provides additional track measurements and particle identification. The tracks of charged are curved by the strong magnetic field of 2T provided by the surrounding solenoid. The overall structure of the ID can be seen in figure 3.4. It is about 6 m long and 2 m high and covers $|\eta|$ range up to 2.5. All three sub detector are divided into the barrel and end-cap regions. In the end-caps layers of sensors are mounted as disks or wheels perpendicular to the beam axis where as the barrel is composed of cylindrical layers of sensors arranged concentrically around the beam pipe.

Pixel detector

The fundamental unit of the pixel detector is the silicon semiconductor module. The basic working principle is, when a charged particle pass through these modules, electron-hole pairs are generated and the created charge is then collected and measured via read out channels. A module is a rectangular active device of area 16.4 × 60.8 mm^2, and a thickness of 250 μm. Each module consist of 47232

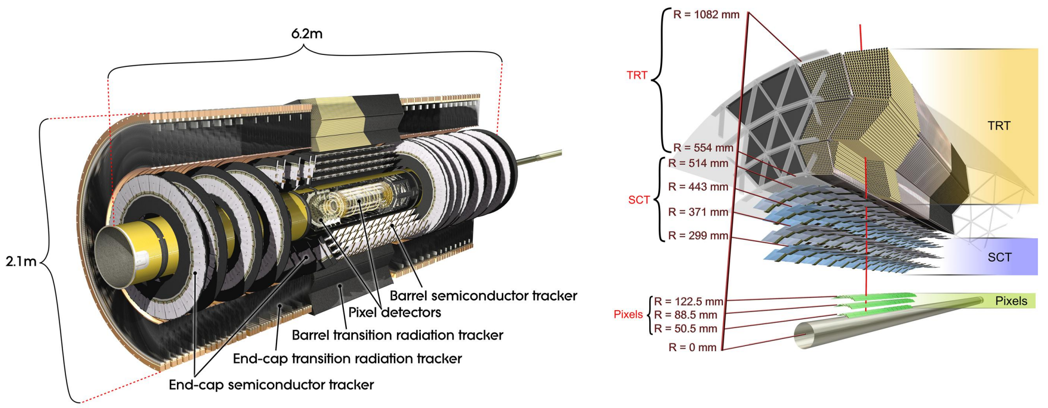

Figure 3.4: (a) Schematic view of the ATLAS inner detector. (b) Drawing showing the sensors and structural elements [15]

pixels of nominal size 50×400 μm. The whole pixel system has about 80.4 milion readout channels, majority of the total readout channels in the ATLAS detector.

Originally, there were three cylindrical layers surrounding the beam pipe (barrel) and three end-cap disks concentric with the beam at each end of the barrel. The barrel three layers located at 50.5 mm, 88.5 mm and 122.5 mm, respectively and the disk layers are located at z positions of 495 mm, 580 mm and 650 mm. During the Long Shutdown 1 (LS1), a fourth layer named as Insertable B-Layer (IBL) was placed 33 mm from the center of the beam-pipe. It aims at providing improvements on b-tagging and secondary vertex reconstruction.

Semiconductor Tracker

The second silicon semiconductor detector named as Semiconductor Tracker (SCT), is placed around the pixel system. It consists of 4088 modules of silicon-strips arranged in four layers in the barrel section and two end-caps with nine disks on each end. Covering this area with pixels would significantly increase the number of read-out channels, result in complicating the data collection process. So a strip layout is used in order to maintain the number of channels to a reasonable value without degrading the resolution.

Each layer of the SCT is covered with strip of size 80 μm $\times$ 12 cm. Two back-to-back layers of silicon strips are placed together with a small stereo angle of 40 mrad to each other. This helps improving the space resolution along the longest strip dimension. The spatial resolution is 17 μm perpendicular to the strip, and

580 μm in the parallel direction. The hits in SCT provide 30 % better precision to reconstruct the track momentum up to $p_T = 500$ GeV. Though larger than the pixel, in the SCT there are only around 6 million channels, while covering the same region of pseudorapidity $|\eta| < 2.5$.

Transition Radiation Tracker

The Transition Radiation Tracker (TRT) is outermost part of the ID. In contrast to the previous two sub-detectors based on the semi conductor technology, the TRT is a gaseous detector consists of thin-walled proportional drift tubes (straws) 4 mm in diameter, filled with gases mixture (70% Xe, 27% CO_2, and 3% O_2). In the centre of the tubes, there is a 0.03 mm diameter gold-plated tungsten wire. A constant voltage is applied between central wire and the outer wall. When a particle transverse through gas mixture in the tubes it ionize the gas molecules. The free electrons drift towards the central anode wire, where they are amplified and readout by the radiation-hard front-end electronics. The TRT barrel region contains 52544 straws of 144 cm in length, oriented parallel to the beam while two end-caps each contain 122880 straws 37 cm in length radially aligned to the beam axis.

Along with the simple detection of a passing particle, the TRT also provides additional information on the particle type that flew through the detector, i.e. if it is an electron or pion. These information are provided through transition radiation, generated in a polypropylene mixture placed between the straws. The emission of the transition radiation depends on the relativistic factor $\gamma = E/m$, which is high for the electron due to its low mass. A very robust pattern recognition is achieved by combination of precision trackers at small radii in Pixel and SCT, with the TRT at a larger radius.

3.2.3 The calorimeter system

The philosophy behind the calorimeters is almost opposite to that of inner tracking detectors. Instead of letting the particles transverse through the inner detector, tracking the particle trajectory with as little material as possible, calorimeters on the other hand, force the particles to deposit all their energy and stop in a large chunk of material. Calorimeters used in the ATLAS are sampling calorimeters consist of layers of absorbing (passive) high-density material that stops incoming particles and layers of an active medium that measures their energy.

Different particles behave differently in the calorimeter depending on their properties of interaction with material, so in the ATLAS calorimeter system is divided between two main parts, the electromagnetic (EM) calorimeter and Hadronic calorimeter. The calorimeter system is illustrated in figure 3.5. Electromagnetic calorimeters stops and measure the energy of electrons and photons where as Hadronic calorimeters sample the energy of hadrons. Calorimeters can stop most of the known particles, only muons and neutrinos have the interaction rate small enough to pass the calorimeters.

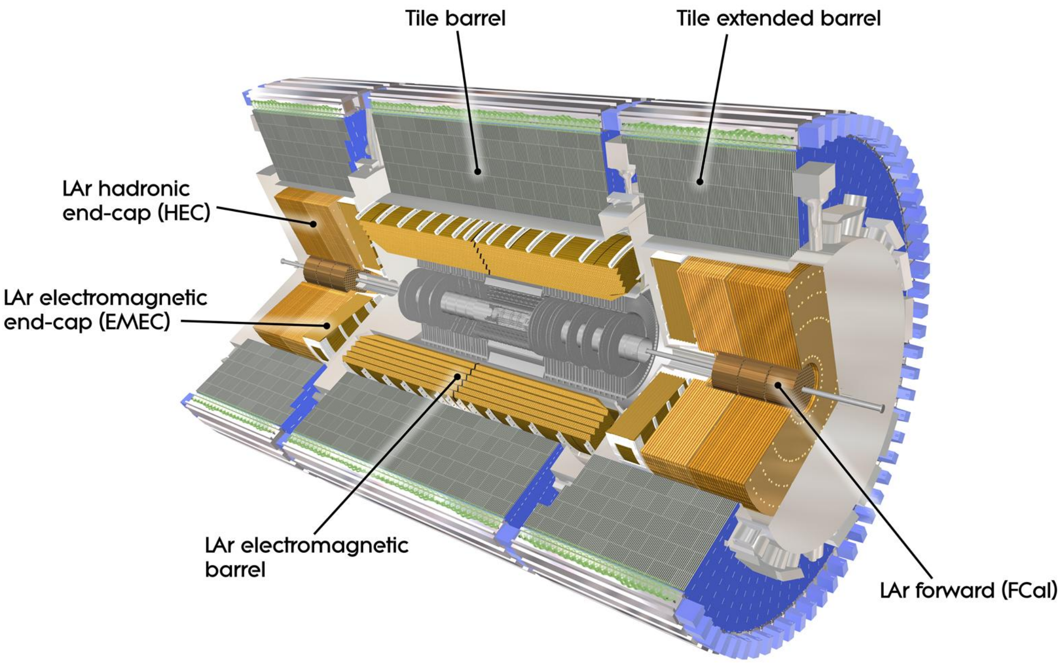

Figure 3.5: Cut-away view of the ATLAS calorimeter system [16].

Electromagnetic calorimeter

The electromagnetic (EM) calorimeter (ECal) is a high-granularity calorimeter to better measure photon and electron showers. ECal uses lead plates as the passive absorber and liquid argon (LAr) as an active material. The liquid argon was selected as active material due to its linear behaviour, stability, and radiation hardness. The accordion-shaped structure of ECal facilitates fast readout and provides full ϕ symmetry without azimuthal cracks. It consist of a barrel section, covering the pseudorapidity range $|\eta| < 1.475$, and two end-caps region covering $1.375 < |\eta| < 3.2$ in two coaxial wheels. There is a crack region between $1.375 < |\eta| < 1.52$ because of the additional material needed to cool the inner detector. This region is usually excluded from physics analyses requiring a precise measurement of electrons. Analysis described in this thesis also veto the crack region.

High energy photons and electrons when enters the passive absorber, produce electromagnetic shower containing many low energy electrons and positrons. Usually electrons emit a photon via bremsstrahlung, while on the other hand photons converts into electron-positron pair (photon conversion), which can in turn undergo bremsstrahlung. The cascade of charged particle ionise liquid argon (active material) sandwiched between the layers, producing an electric current that is measured by readout electrodes to induce a signal which determines the energy measurement.

Hadronic calorimeter

As the name suggests, the hadronic calorimeter (HCal) aims to stop hadrons (i.e. pion, proton, neutron) within its volume and measure the deposit energy. The fragmentation and hadronization of quarks and gluons form these hadrons, gather in a narrow cone called ”Jet”. Without loss of significant energy Jets can pass trough the ID and ECal. The hadronic calorimeter is further divided in three sub-detectors.

The **Tile Calorimeter** is placed directly outside the ECal. Its barrel region is divided into a central section that covers $|\eta| < 1.0$ and two extended barrels cover which range $0.8 < |\eta| < 1.7$. The tile calorimete uses steel as absorber and plastic scintillating tiles as active medium. Hadrons in the first step lose energy mainly through nuclear interactions with the absorber producing a hadronic shower. Charged particles produced in hadronic shower create fluorescence photons by passing through the plastic scintillators (active medium). The long fibres at the end of each tile carried the light to the photomultiplier tubes to convert them to an electric signal whose intensity is proportional to the original particle’s energy.

The **LAr hadronic end-cap calorimeter** (HEC) consists of two independent wheels per end-cap. Located directly behind the end-cap electromagnetic calorimeter it covers $1.5 < |\eta| < 3.2$, overlapping slightly with the Tile calorimeter. Each wheel consist of 32 wedge-shaped modules. HEC uses liquid argon as active material similar to that of the EM calorimeter, but have copper plates as the absorbing material.

The **LAr forward calorimeter** (FCal), is placed at $3.1 < |\eta| < 4.9$ which cover highest values of the $|\eta|$. The FCal uses LAr as the active medium has three layers of separate modules. The first using copper as the absorber is optimized for electromagnetic measurements while the latter two use tungsten to measure predominantly the energy of hadronic interactions.

3.2.4 The muon spectrometer

The muon spectrometer (MS) is the outermost part of ATLAS detector, responsible for identification and measurement of muon momentum, as well as providing a muon trigger. Muons are particles that transverse undetected through the ID and Calorimeter. The muon momentum is determined by measuring the track curvature by a system of tracking detectors placed in magnetic field generated by three toroidal magnets. One provide the magnetic field in the barrel region $|\eta| < 1.4$, while the other two provide in end-cap ($1.6 < |\eta| < 2.7$) at both ends of the barrel. In ($1.4 < |\eta| < 1.6$) namely the transition region, the magnetic field is provided by combination of barrel and end-cap magnets.

The muon spectrometer is made up of 4,000 individual muon chambers employing four different technologies for four sub-systems. Two of which are responsible for high precision tracking: Monitored Drift Tubes (MDTs) and Cathode Strip Chambers (CSCs) while the other two Resistive Plate Chambers (RPCs) and Thin Gap Chambers (TGCs) function as triggers. The layout of the ATLAS muon spectrometer is shown in Figure 3.6.

The MDTs chambers covering range of $|\eta| < 2.7$ is the largest part of the muon system. The main purpose is precise measurement of momentum that is achieved by using three to eight layers of drift tubes, leading to an average resolution of 35 μm per chamber (80 μm per tube). The drift tubes are filled with gas mixture Ar/CO2 (93/7) at a pressure of 3 bar. Each drift tube is 30 mm in diameter with a tungsten-rhenium wire of 50 μm diameter at the center. The electrons resulting from ionization are collected at the central wire. The CSCs are used to cope with higher rates in the forward region ($2.0 < |\eta| < 2.7$). The CSCs are multiwire

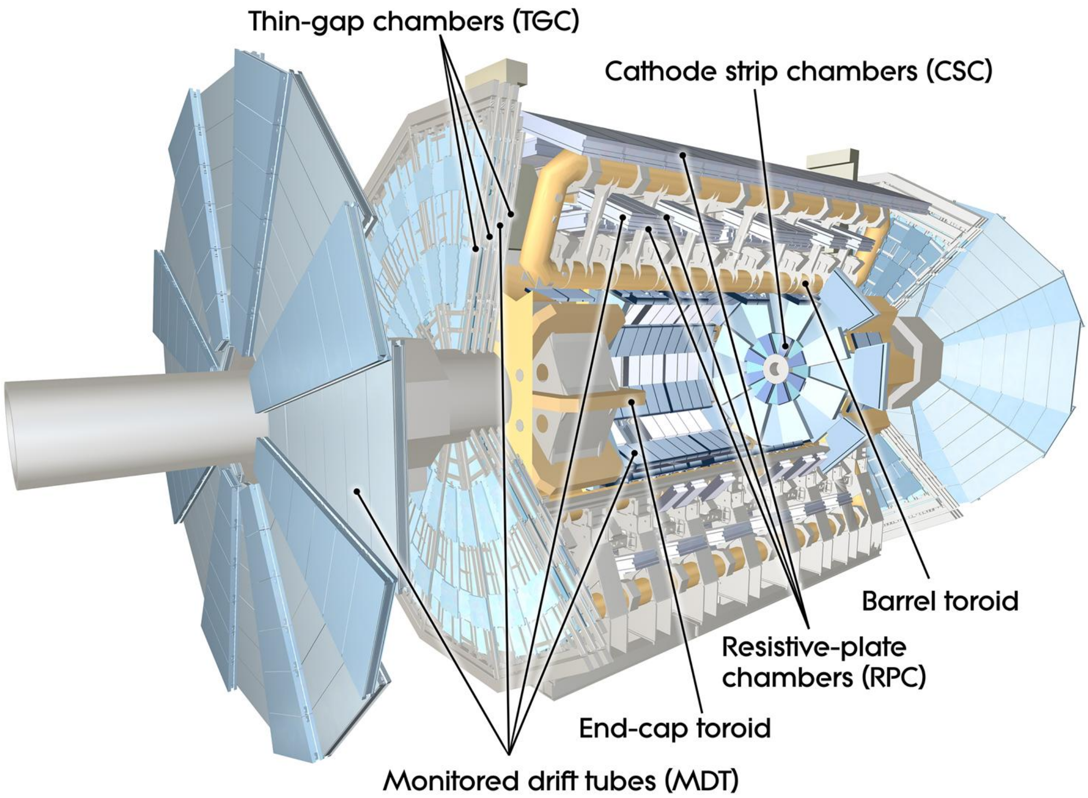

Figure 3.6: Cut-away view of the ATLAS muon spectrometer and its main components [17].

proportional chambers with cathode planes segmented into strips in orthogonal directions. This leads to a good spacial resolution of 40 μm in the bending plane.

The trigger system of the MS is based on the RPC and TGC chambers, provide a fast (15-25 ns) triggering as well as η and ϕ position measurements. In the barrel region $|\eta| < 1.05$, the triggering is provided by the RPC mounted together with MDTs. RPCs are gaseous parallel-plate detectors. Two resistive plates are kept parallel 2 mm apart to each other. The gap is filled with a gas mixture of $C_2H_2F_4/Iso\text{-}C_4H_{10}/SF_6$ (94.7/5/0.3). High voltage between the plates creates uniform electric field. The avalanches is form along the ionizing tracks towards the anode. RPCs are operate in avalanche mode which offers the benefit of higher rate capability and rate-independent time resolution. Muon trigger capability in the endcap region is provided by the TGCs in a pseudorapidity range $1.05 < |\eta| < 2.4$. TGCs are multiwire proportional chambers. Compared to the wire-to-wire gap, the gap between wire and cathodes is very small. The high electric field and the small wire-to-wire distance provide very good timing resolution.

3.3 sTGC production quality control

The ATLAS experiment has planned extensive upgrade in two phases, to cope with the high luminosity that will be delivered by the LHC in this decade. The Phase-I upgrade is currently in finally stage and Phase-II upgrades is scheduled to take place in 2025-2027 time frame during the Long-Shutdown (LS-3). These upgrades will allow the ATLAS experiment to maintain and improve its performance in terms of acceptable trigger rates at low-pT thresholds, pile-up mitigation and detector occupancy for upcoming Run-3 and for the High Luminosity LHC program (HL-LHC) expected to start in 2027. The figure 3.7 shows the time line form LHC to High Luminosity-LHC.

In Phase-I upgrade four areas of the ATLAS detector are updated: the liquid argon (LAr) calorimeter front-end electronics, the Barrel Inner Small layer of muon spectrometer, the TDAQ system and the New Small Wheel detector in MS. The largest Phase-I upgrade project for the ATLAS Muon System was the replacement of the forward muon-tracking region with the so-called New Small Wheels (NSWs) which was completed and installed in November 2021.

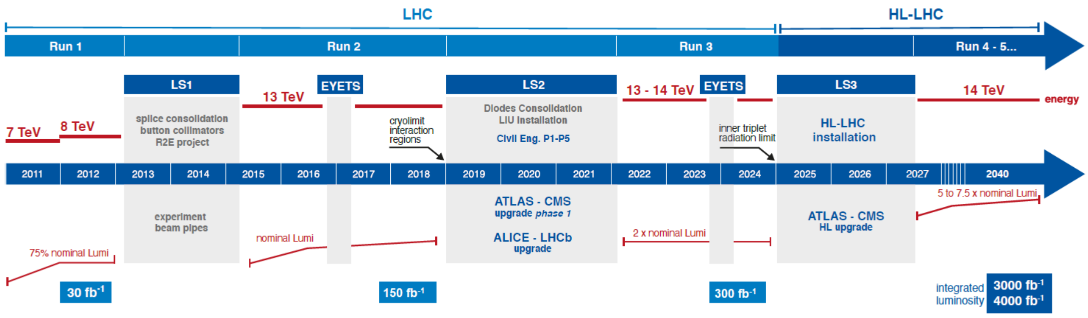

Figure 3.7: Time line of the High-Luminosity LHC. Phase-I upgrade is completed in LS-2 and LHC expected to restart in mid-2022 for Run which is extended by one year. In LS-3, Phase-II of upgrade will be performed. HL-LHC will start to operate in 2027 and will deliver a total integrated luminosity up to 3000 fb^{-1} [18].

The New Small Wheel system consists of two wheels, each of radius 5 m, located in the end-cap region ($1.3 < |\eta| < 2.7$) at both ends of the detector (side A and C). The main objective of NSW is to reduce the muon triggers caused by noise or accidental coincidences in the end-cap region. The old SW chambers, which was based on monitoring drift tubes, also cannot perform bunch crossing identification at rates up to 15 kHz/cm^2. With the NSW, as shown in Figure (right) 3.8 only the hypothetical track A is accepted due to coincidence between the existing detectors (the Big Wheel), and the New Small Wheel. Where as both track B and C are rejected, the track B, producing only hits in the Big Wheel and the track C not originating from the interaction point.

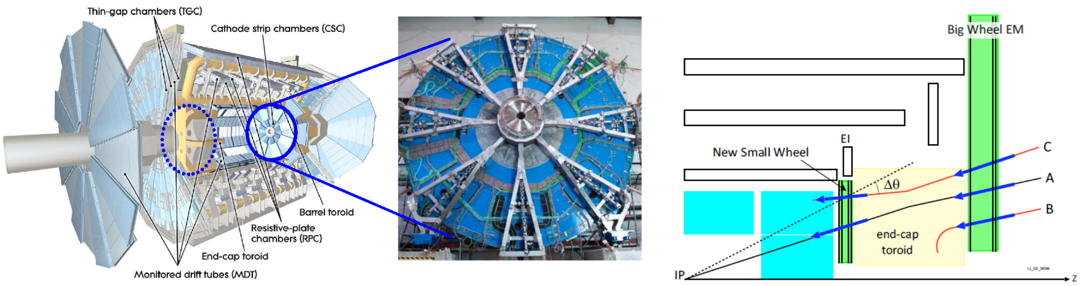

Figure 3.8: Left: Completed New Small Wheels installed in ATLAS cavern in Nov-2021. Right: working principle of the track selection trigger of the NSW (transverse view)[19].

3.3.1 The small-strip Thin Gap chambers (sTGC)

The NSW is based on two technologies: small-strip Thin Gap chambers (sTGC) as primary trigger and Micromegas chambers as the primary precision tracker. The sTGC is mainly dedicated for trigger and bunch crossing identification also provides track measurement with a precision of about 100 μm per chamber and good angular resolution (< 1 mrad). The NSW consist of total 96 sTGC and 64 Micromegas quadruplets. The sTGC quadruplets are of six types, three for large and small sector respectively as shown in Figure 3.9. The shape of each quadruplet is trapezoidal with dimensions between 1-2 m^2. The production and testing took placed in member institutes of the ATLAS collaboration. Shandong University, China was one of the production site.

The sTGC as show in Figure 3.10, is based on the technology of Multi-Wire Proportional Chambers. It consists of a layer gold plated tungsten anode wires of 50 μm spaced by 1.8 mm. The layers of wires plane are sandwiched between two cathode graphite-sprayed planes at a distance of 1.4 mm. The precision cathode plane has strips with a 3.2 mm pitch for precision readout and the cathode plane on the other side has pads for triggering .

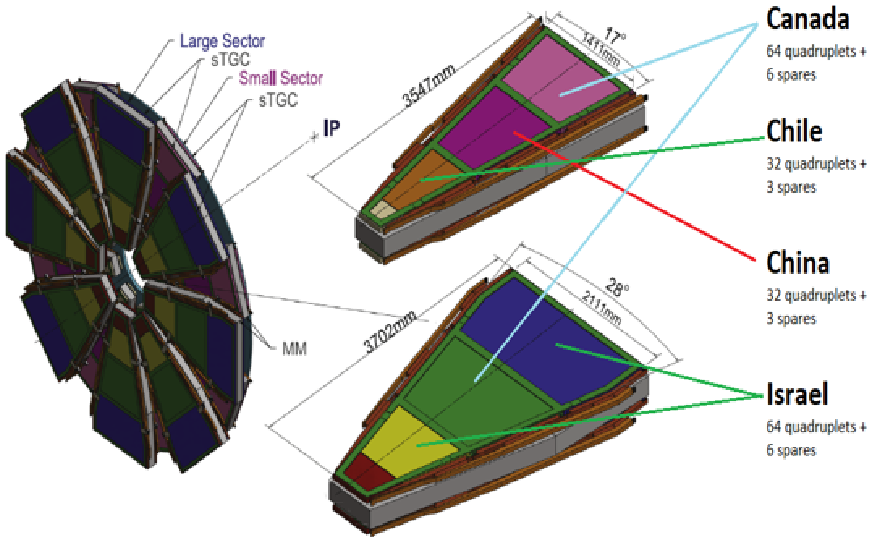

Figure 3.9: Schematic of the small and large sTGC sectors and corresponding production site. [20]

3.4 sTGC irradiation scans with X-ray

sTGC detectors will work in a intense radiation environment during Run-3 and HL-LHC and will be practically inaccessible during these run periods. So there were very strict quality control procedures during chamber production. Before the chambers were fully assembled at CERN, various tests were carried out at early stages at production cites in order to be able to introduce corrections in the production process and to eliminate any technological defects.

In Shandong, I used technique based on the X-ray scanner with direct measurement of the chamber current to check any technological defects such as cathode strip and gap thickness defects, dust particles inside the gap and on the wires, gluing defects, missing wires, wires lost tension etc. Based on the intensity of the x-ray, two kind of tests were performed , High intensity scans: To check problem related to construction procedure and Low intensity scan: To check the uniformity of the gain. Tests were performed on sTGC champers prior to the readout electronics installation. It allowed to test the quality of the chambers, identifying defects and fixing them at early stage.

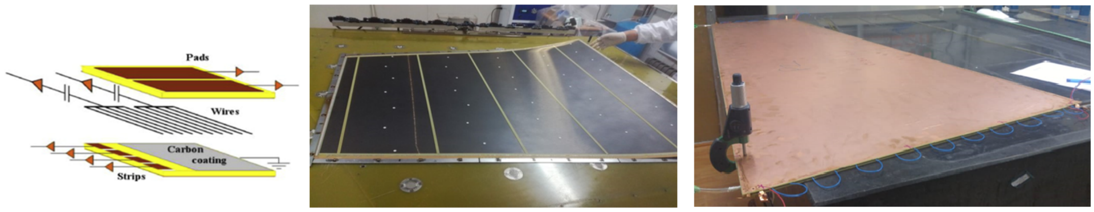

Figure 3.10: Schematic diagram (left) of the basics sTGC structure to Soldering of pads to the sTGC fabrication (right)

3.4.1 Experimental set-up

The X-ray scanner [21] is Computer numerical control (CNC) machine designed to scan the entire sTGC, an area 2220×1410 mm covers the maximum sTGC chamber size. The Amptek $MINI$-X, X-ray tube is used which can operate on 10-40 kV and 5-80μA. CAEN-N1471H high voltage power supply was used to measure the current from anode wires, which is able to measure the current with a precision up to 50 pA. The X-ray tube is mounted on X-Y scan machine show in Figure 3.11, can operate in both directions in a step-sized movement mode (also can be operated with continues movement). The speed can be set in the range of 0.5 -100 mm/s or in step mode with steps 0.5 mm or larger. The scan were performed with *n-pentane* $+ CO_2$ as working gas mixtures. Some test were also performed with only CO_2. The was gas flushed for 20 hours into the chamber before the tests were performed. A special graphical user interface and visualization tool [22], QScanner and QViewer respectively were used to perform the scans and to analyze the results.

3.4.2 Measurement of parameters of scanner

Before performing the whole chamber scan, it was curial to set different scan parameters in order to perform the test efficiently. These parameters includes:

- Measurement of the saturation current
- Hardness of the x-ray
- Distance effect between x-ray and chamber
- Measure the x-ray outshoot cone

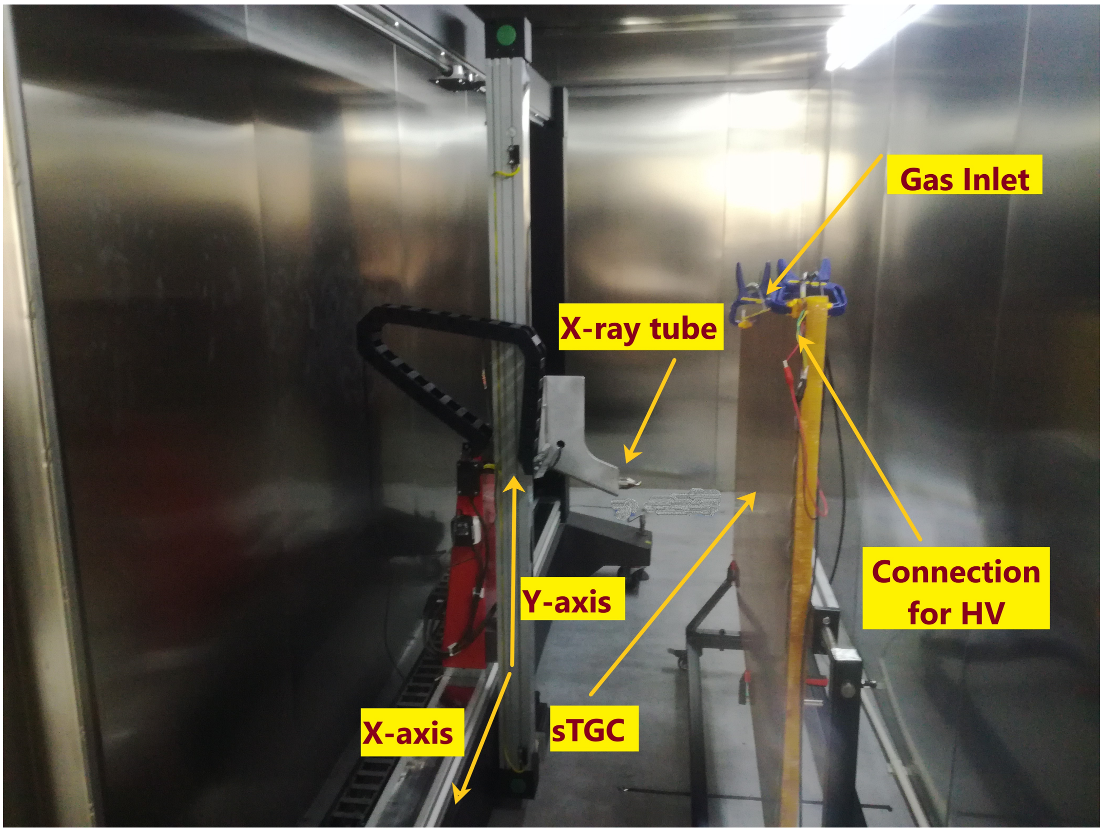

Figure 3.11: X-ray scanner: an X-Y CNC machine designed to scan the entire sTGC area with X-ray tube and to measure the current from anode wires

In order to measure the saturation current of the chamber, the x-ray current is increased from 5 to 30 μA, as a result the chamber current should be move higher. If the chamber is saturated, it should reach current plateau at some point. As show in graph (left) 3.12, As we increase the x-rays current the chamber current increases but did not reach saturation level. There must be a current saturation value at higher voltage, but did not check above 3.2 kV extreme limit, using even higher values are not safe for the chamber.

The effect we want to know from varying the distance of x-rays tube to the chamber is the absorption of x-ray by the atmosphere. Except this we expect the x-ray radiated on chamber is same, the current should be stable. In the graph (middle) 3.12, the chamber current is measured as a function of distance of the chamber form X-ray tube. The current remains almost stable. We use 10 cm as nominal distance of the x-ray tube from the chamber.

To measure the hardness of the x-rays, the HV of the x-ray increased from 5 to 50 kV, keeping the x-ray current at 5 mA, measure the chamber current as function of HV. As shown in graph (right) 3.12, with HV increasing the X-rays penetration power increases, higher current is observed at both 2.9 and 3.0 kV applied to the chamber.

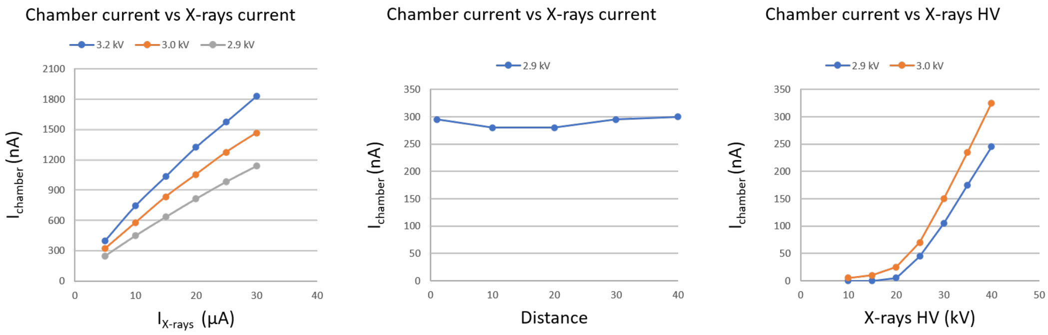

Figure 3.12: Left: measurement of the saturation current, Middle: measurement of distance effect, Right: measurement of the hardness of the x-ray

3.4.3 Full Chamber Scan Result

The tests of sTGC complete chambers irradiated with X-ray source was carried out with CO_2 +*n*-*p* gas flow through chamber for 20 hours. Scans were performed with Standby time = 3 seconds and Collimator size 40 mm (step size 20 mm) at 100 mm distance of the chamber form X-ray tube. The X-ray tube was running at 40 kV with a current of 5.0 μA. The voltage on chamber was set to 3.2 kV. Figure 3.13 show the full scan results for chamber `GS2.C3.9`. The result shows the higher operation stability and lower sensitivity to the electric field non-uniformity. No areas with self-sustaining discharge or hot spots were found. Chamber current due to X-rays remain constant with scanning time ($\approx$ 4 hours). The points below 200 nA are because of fall of X-rays on supporting rods. Base current varies with the scanning time due to environmental effects. For most of cases base current is high in beginning of scan and decrease with time. The results are summarized in table 3.2.

Mean Current (nA)	Base Current (nA)	RMS	Points outside the 20% limit	Points below 20%of mean current	Points above 20%of mean current	# of hot points above 5 σ	Max value of hot point
217.10	84.11	42.06	9.58%	9.10%	0.58%	8	950

Table 3.2: Results for `GS2.C3.9` chamber full scan. The stable current value represents the high operation stability.

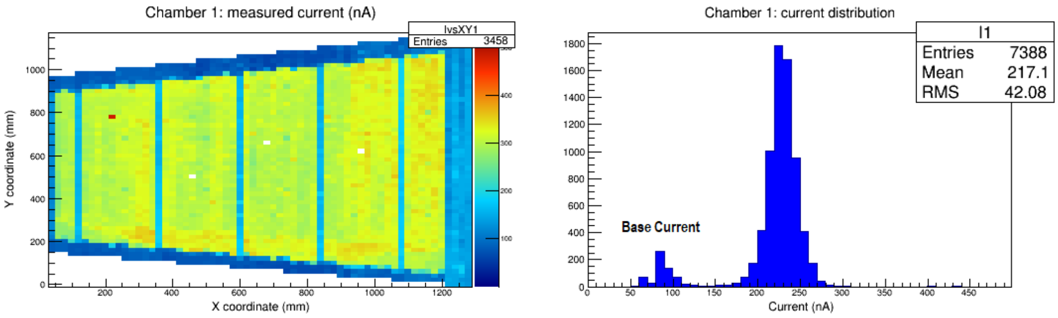

Figure 3.13: Left:Currents map for the chamber operating with CO_2 +*n*-*p* gas mixture. Right:the mean current value

In total 85 sTGC chambers have been tested at the University of Shandong, one of the NSW sTGC construction sites. The test were performed at increased HV, higher than then one later used in ATLAS, to artifically stress test the chambers and so detect any weaknesses. The analysis of gas gain uniformity shows mostly stable results with no large variations in the mean value of current with same working parameters. The current value below the 20% threshold is mostly due the supporting rods. The extracted statistical parameters are stored in the NSW sTGC QA/QC database.

Mean Current (nA)	Base Current (nA)	RMS	Points outside the 20% limit	Points below 20%of the mean current	Points above 20%of the mean current	# of hot points above 5 σ	Max value of hot point
282.91	71.93	55.68	14.55%	11.50%	3.06%	15.63	2331.18

Table 3.3: Summary of the 85 sTGC chamber scan results.

Chapter 4 Analysis strategy and selections

4.1 Introduction

The production of Higgs bosons in association with a single top quark (tHq production) at the LHC proceeds at leading order (LO) dominantly via two Feynman diagrams: the Higgs boson couples either to the top quark (t) or the W boson, as shown in figure 4.1. In these two diagrams, a light-flavour quark q (i.e. u- or $\bar{d}$-quark) from one of the colliding protons interacts with a b-quark by exchanging a virtual W boson, producing either a Higgs boson and top quark or just a top quark (which radiates a Higgs boson) and a recoiling light-flavour quark (i.e. d- or $\bar{u}$-quark), called the spectator quark. The b-quark comes either directly from another colliding proton in the five-flavour scheme (5FS) or from a gluon splitting in the four-flavour scheme (4FS). In the 5FS the b-quarks are treated as massless in the parton distribution functions, while in the 4FS, the parton distribution functions only contain parton distributions for the quarks lighter than the b-quark and b-quarks are treated as massive.

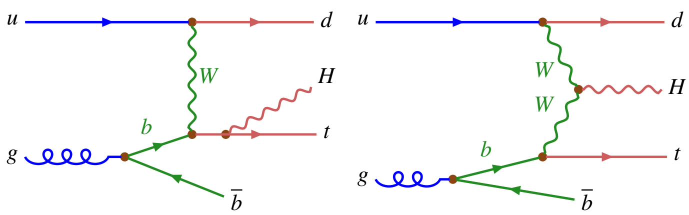

Figure 4.1: Representative dominant Feynman diagrams for the tHq production at LO, in the 4FS. The Higgs boson is either radiated from (a) the top quark or (b) the W boson.

The production cross-section is sensitive to the magnitude as well as the relative sign and phase of the couplings, due to the interference between these two diagrams. Figure 4.2 shows the dependence of the tHq inclusive cross-section with a next-to-leading order (NLO) accuracy to the top-quark coupling y_t [97] in proton–proton (pp) collisions at a centre-of-mass energy of 13 TeV at the LHC. In the SM hypothesis ($y_t = +1$), the interference between these two diagrams is maximally destructive and leads to very small production cross-sections of about 71, 16 and 2.9 fb for the t-, tW- and s-channel, respectively, at $\sqrt{s} = 13$ TeV

[98]. New physics effects could lead to constructive interference between the ttH and WWH couplings and therefore enhance the cross-sections by an order of magnitude or more. In this analysis, the tHq and tWH processes are considered as separate tH productions, while the s-channel production is neglected.

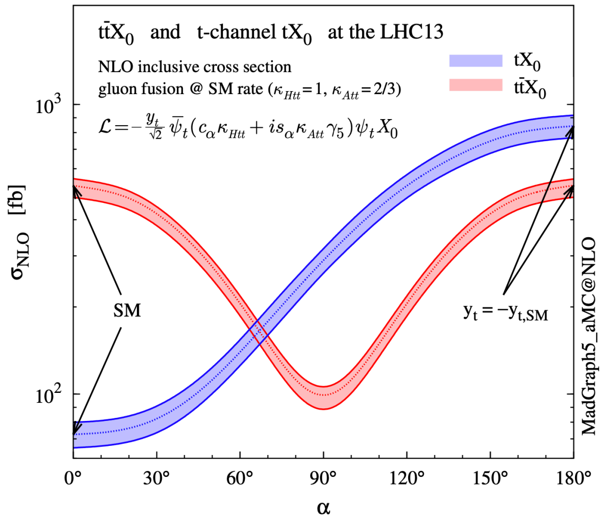

Figure 4.2: NLO cross-sections (with scale uncertainties) for $t\bar{t}X_0$ and t-channel tX_0 productions for pp collision at $\sqrt{s} = 13TeV$ as a function of the CP-mixing angle α, where κ_{Htt} and κ_{Att} are set to reproduce the SM gluon fusion cross-section for every value of α (figure extracted from Ref. [97]).

4.1.1 Analysis strategy

The analyses use an integrated luminosity of 139 fb^{-1} of data collected with the ATLAS detector at $\sqrt{s} = 13$ TeV between 2015 and 2018 at the LHC. The search uses final state distinguished by the number and flavour of leptons. The $2LSS$ is one channel among the multi lepton analyses channels:

- $3L$: three light-flavour leptons without any hadronically decaying τ lepton
- $2LSS$: two same-charge light-flavour leptons without any hadronically decaying τ lepton
- $2L + 1\tau_{had}$: two light-flavour leptons with one hadronically decaying τ lepton
- $1L+2\tau_{had}$: one light-flavour lepton with two hadronically decaying τ leptons

Each channel is analysed separately with its own signal region (SR) and control regions (CRs). A common lepton selection is used for all channels. Tau leptons are included explicitly in the analyses and jets that are identified as tau leptons are removed. In order to ensure that there is no overlap in the events selected in each of the channels, a basic selection to separate the events into the different channels is applied using a `loose` lepton selection. The object definition and `loose` selection for $2LSS$ channel is described in section 4.3.

The v34 [30] of the single-top ntuples [25] which serves to provide a common definition of the basic physics objects used. The multivariate analysis techniques (MVAs) (boosted decision trees (BDTs)) is used to improve the signal to background separation and to define CRs. Cross-section measurements or upper limits are determined by fitting the MVA output in both SRs and CRs using `trexfitter` framework [24]. Even though it is only expect to set an upper limit on the signal strength using the LHC Run 2 dataset a blinding has been applied on the data for MVA outputs. Systematic are pruned by applying thresholds of 1% on shape and 0.5% on normalization.

The tHq ML channels probe the decay of the Higgs boson into a pair of vector bosons (W or Z) or τ leptons. The four channels are sensitive to different decays of the Higgs boson. Table 4.1 reports the percentage of simulated tHq events where the truth Higgs goes ($H \to WW^*, ZZ^*, \tau\tau$). The $3L$ and $2LSS$ channels are mostly probing tHq events where $H \to WW^*$, while the $2L + 1\tau_{had}$ and $2L + 2\tau_{had}$ channels are mainly sensitive to $H \to \tau\tau$ decays.

Channel	$H \to WW^*$	$H \to ZZ^*$	$H \to \tau\tau$
$3L$	69	17	14
$2LSS$	80	3	17
$2L + 1\tau_{had}$	32	5	63
$2L + 2\tau_{had}$	3	1	96

Table 4.1: Percentage of tHq simulated events where the truth Higgs boson decays into $H \to WW^*$, $H \to ZZ^*$ or $H \to \tau\tau$ in each tHq ML channel. The events are those passing the pre-selection requirement defined by the channel. The statistical uncertainty is smaller than 0.1% for all the values in the table.

4.2 Data and Monte-Carlo simulation

In this section the description of data and MC simulations samples used in the analysis is presented. A slimmed and skimmed version [25] of the ATLAS single top group 'TOPQ1' derivations [26] were centrally produced. These common data-sets used in the multi-lepton analyses, were produced with the SingleTop-Analysis package [29]. Following the recommendations of top-quark reconstruction working group [33], all the object calibrations and corrections provided by the combined performance groups are implemented in this package. Using the computing batch systems in different locations (BONN, NORTHGRID, IFIC, BNL) an additional skimming is performed on these data samples. This skimming was done using the `thqloop` framework, where variables of interest for each the analysis channel are computed and after the computation kept only branches required by specific analysis channel from the centrally produced ntuples.

4.2.1 `tHqLoop` set up

The framework called `thqloop` [34] is used to create flat ntuples. It perform the skimming on the single-top ntuples, and to compute extra variables that are required in the multi-lepton analysis. The `thqloop` is an ATLAS-cmake-style package, designed to be compiled with TopLoop in an ATLAS Analysis Release. The algorithm was set-up to save some simple event properties:

- Save the nominal weight
- Save the leading and subleading lepton transverse momenta
- Save the pileup systematic weights (UP and DOWN)
- Save the total number of jets that have transverse momentum higher than 25 GeV and have absolute pseudorapidity inside 2.5.

4.2.2 Data samples

The data event samples used in the analysis are collected by the ATLAS detector from 25 ns pp collisions delivered by the LHC from 2015 to 2018 (full Run-II) at $\sqrt{s} = 13$ TeV. Using unprescaled single-lepton triggers as indicated in the references [35, 36, 37], events were chosen from a common data stream. The registered data were filtered at the luminosity block level using good-runs lists (GRLs) [38]. The GRLs required the data quality (DQ) flags for all detectors and trigger sub-components to be green along with stable beams flag to be true. The amount of data used corresponds to an integrated luminosity of 139 fb^{-1}. Total integrated luminosity uncertainties for each data-taking year vary from 2.0 to 2.4 % [12] . These uncertainties are derived from the calibration of the luminosity scale using x-y beam-separation scans, and using the LUCID-2 detector for the baseline luminosity measurements [40]. The uncertainty in the combined 2015-2018 integrated luminosity is 1.7% [12]. The partial and total integrated luminosities together with their uncertainties and some additional details are given in table 4.2.

Year	Periods	Run numbers	Number of events	Integrated luminosity [pb^{-1}]
2015	D-H,J	276262–284484	220.58M	3219.56 ± 2.1%
2016	A-G,I,K,L	297730–311481	1057.84M	32988.1 ± 2.2%
2017	B-F,H,I,K	325713–340453	1340.80M	44307.4 ± 2.4%
2018	B-D,F,I,K,L,M,O,Q	348885–364292	1716.77M	58450.1 ± 2.0 %
2015–2018	All	276262–364292	4335.99M	138965.16 ± 1.7%

Table 4.2: Integrated luminosity per year with their relative uncertainties. Additionally, run numbers per year are shown.

4.2.3 Simulated event samples

Samples of events generated using Monte Carlo (MC) simulations were produced using different event generators interfaced to various shower/hadronisation generators. The production included three campaign MC16a/d/e [41, 42, 43] of the ATLAS MC Production Group. With the specific ATLAS software architecture (named `Athena`) [44], the trigger and detector simulation is carried out following the event generation stage, either fully utilizing the `Atlfast2` [44] (simply known as AFII) for fast simulation or the GEANT4 [45] framework for a detailed physics description simulation. Detector simulation with GEANT4 is accurate but requires significant CPU resources. The calorimeter shower simulation, the most CPU-intensive part of the simulation, has been replaced by ATLAS with tools that use quicker simulation techniques. AtlFast3 is used to address present and upcoming computational issues as well as the simulation requirements of the ATLAS experiment. It blends parametric approaches with machine-learning techniques. In this analyses, full-simulated (FS) event samples are used as baseline samples unless not available.

The effect of multiple interactions in the same and neighbouring bunch crossings (pileup) was modelled by overlaying the simulated hard-scattering event with inelastic proton–proton (pp) events generated with [46] using the NNPDF2.3LO set of parton distribution functions (PDF) [47] and the third ATLAS set of tuned parameters for minimum-bias events (A3 tune) [48] over the original hard-scattering event. The MC events were weighted to reproduce the distribution of the average number of interactions per bunch crossing ($\langle\mu\rangle$) observed in the data. The $\langle\mu\rangle$ value in data was rescaled by a factor of 1.03 ± 0.04 to improve agreement between data and simulation in the visible inelastic proton–proton (pp) cross-section [49]. In this analyses, samples of events generated using MC simulations were produced for tHq signal and most of the background processes, and are used to evaluate models of efficiency and resolution, and to estimate systematic uncertainties. The event generators and configurations for these MC samples are summarized in table 4.3.

Process	Generator	Parton shower	PDF	MC tune
tHq (ML)	MadGraph5_aMC@NLO 2.6.2	Pythia 8.230	NNPDF3.0NLO	A14
$t\bar{t}(nonallhad)$	Powheg	Pythia 8.230	NNPDF3.0NLO	A14
$W/Z+jets$	Sherpa 2.2.1	Sherpa default	NNPDF3.0NNLO	Sherpa default
$t\bar{t}Z(z\to ll)$	MadGraph5_aMC@NLO 2.3.3	Pythia 8.210	NNPDF3.0NLO	A14
$t\bar{t}W(^{*})$	MadGraph5_aMC@NLO 2.3.3	Pythia 8.210	NNPDF3.0NLO	A14
$WZ/ZZ+jets$	Sherpa 2.2.2	Sherpa default	NNPDF3.0NNLO	Sherpa default
$t\bar{t}H$	MadGraph5_aMC@NLO 2.6.0	Pythia 8.230	NNPDF3.0NLO	A14
tHW	MadGraph5_aMC@NLO 2.6.2	Pythia 8.235	NNPDF3.0NLO	A14
tW	Powheg	Pythia 8.230	NNPDF3.0NLO	A14
$tZ(Z\to ll)$	MadGraph5_aMC@NLO 2.3.3	Pythia 8.230	NNPDF3.0NNLO	A14
$tWZ(Z\to ll)$	MadGraph5_aMC@NLO 2.3.3	Pythia 8.230	NNPDF3.0NNLO	A14
$t\bar{t}WW$	MadGraph5_aMC@NLO 2.2.2	Pythia 8.186	NNPDF2.3LO	A14
$H+W/Z$	Pythia 8.186	Pythia 8	NNPDF2.3LO	A14
$VVV(V=W/Z)$	Sherpa 2.2.2	Sherpa default	NNPDF3.0NNLO	Sherpa default
$tt\bar{t}, t\bar{t}t\bar{t}$	MadGraph5_aMC@NLO 2.2.2	Pythia 8.186	NNPDF2.3LO	A14
$Higgs(ggH/VBF/VH)$	Pythia	Pythia 8.210	CT10	AZNLO CTEQ6L1

Table 4.3: The configurations used for event generation of signal and background processes. The samples were simulated using different generator at leading-order with NNPDF2.3LO, next-to-leading order NNPDF3.0NLO and next-to-next leading order NNPDF3.0NNLO parton distribution function (PDF). 'Tune' refers to the underlying-event tune of the Pythia/Sherpa parton shower generator.

4.3 Objects definition and selection

In this section, description of the procedures used to calibrate, reconstruct and selection of the physical objects (electrons, muons, tau leptons, jets, b-tagged jets and missing transverse momentum) are discussed. These requirements need to identify events with a tHq signature. For data gathered by the ATLAS detector between 2015 and 2018, these approaches adhere to the most recent suggestions made by the top-quark reconstruction working group [57].

4.3.1 Triggers

A hardware-based Level-1 (L1) trigger and a software-based high-level trigger (HLT) make up the ATLAS event trigger system. Due to changing pile-up conditions during the data collection period of Run-II [58], various single-lepton un-prescaled triggers were employed.The table 4.4 shows list of trigger names used in this analysis.

Year	Single-electron trigger	Single-muon trigger
2015	HLT_e24_lhmedium_L1EM20VH HLT_e60_lhmedium HLT_e120_lhloose	HLT_mu20_iloose_L1MU15 HLT_mu50
2016–2018	HLT_e26_lhtight_nod0_ivarloose HLT_e60_lhmedium_nod0 HLT_e140_lhloose_nod0	HLT_mu26_ivarmedium HLT_mu50

Table 4.4: Un-prescaled single-lepton trigger selections of the ATLAS trigger menu per lepton flavour per year. A logical OR is used to aggregate all of these triggers.

An aligned calorimeter cluster for a track is chosen by the electron triggers. The identification criteria for electrons must then be met utilizing a likelihood (LH) discriminant in a multi-variate approach. In this analysis, the following single-electron triggers were used:

- Data collected in year 2015, electrons were triggered by requiring at L1 a transverse energy deposit E_T above 20 GeV, with a reduced calorimeter granularity being considered at this stage. At the HLT, the full granularity of the calorimeter as well as tracking information are available and the reconstructed calorimeter cluster was matched to a track. The trigger electron object was then required to be isolated with `medium` identification (section 4.3.2) and to have $E_T > 24$ GeV.

- In 2016–2018, electrons had to satisfy a `tight` identification at HLT together with an isolation criteria and have $E_T > 26$ GeV.

- In addition to the previous trigger, during all years of Run-II, to avoid efficiency losses due to identification and isolation at high p_T, two additional complementary triggers were used, either selecting `medium` electrons with $E_T > 60$ GeV at HLT or selecting `loose` electrons (i.e. without isolation requirement) with $E_T > 120$ GeV in 2015 and $E_T > 140$ GeV in 2016–2018.

Muons are triggered by matching tracks reconstructed in the muon spectrometer and in the ID. In 2018, muons had to satisfy a loose isolation requirement and have $E_T > 20$ GeV. In 2016–2018, the isolation criterion was tightened and the threshold increased to $E_T > 26$ GeV. As for the electron triggers, during all these years, in order to avoid efficiency losses due to isolation at high p_T another muon trigger without any isolation requirement was available, selecting loose muons with $E_T > 50$ GeV.

Data-to-MC scale factors are applied to simulated events to correct for the different trigger efficiency observed in data with respect to the simulation [59]. The `TriggerMatchingTool` [60] is used to match the trigger lepton to one of the leptons in the event. The presence of at least one trigger-matched lepton in the event is required. Moreover, since the data-to-MC scale factors for the trigger efficiency are derived for leptons having $E_T > 27$ GeV, an additional selection is applied to the trigger matched lepton to satisfy this p_T cut.

Year	Di-electron trigger	Di-muon trigger	Electron+muon trigger
2015	HLT_2e12_lhloose_L12EM10VH	HLT_2mu10	HLT_e17_lhloose_mu14
		HLT_mu18_mu8noL1	HLT_e7_lhmedium_mu24
2016–2018	HLT_2e17_lhvloose_nod0	HLT_2mu14	HLT_e17_lhloose_nod0_mu14
		HLT_mu22_mu8noL1	HLT_e7_lhmedium_nod0_mu24

Table 4.5: Un-prescaled di-lepton trigger selections of the ATLAS trigger menu per lepton flavour per year.

At the earlier stage of analysis (with v30 of SingleTop ntuples) the impact of di-lepton triggers is also studied and found to be negligible. Table 4.5 includes the list of the di-lepton triggers used for this studies. The affect of the di-lepton triggers in preselection regions was studied and compared to the results from using single-lepton triggers and the combination of single- and di-lepton triggers. The preselection regions were defined using different jets and b-tagged jets multiplicity along with $p_T > 27$ GeV and $p_T > 20$ for leading and sub-leading leptons respectively .

Region	Trigger	Signal: tHq	Total Backgrounds	Fakes: (ttbar)	Purity: (S/B (%))	Significance: (S/$\sqrt{B}$)
$nJets \geq 2$; $nbjets = 1$	Single-Lepton Triggers	10.37	11419.63	7790.2	0.091	0.097
	Di-Lepton Triggers	9.38	8976.35	6156.34	0.104	0.099
	Single- and Di-Lepton Triggers	10.51	11542.09	7884.14	0.091	0.098
$nJets \geq 2$; $nbjets = 0$	Single-Lepton Triggers	6.39	27518.41	4744.07	0.023	0.039
	Di-Lepton Triggers	5.79	21407.51	3700.4	0.027	0.040
	Single- and Di-Lepton Triggers	6.48	27756.82	4801.01	0.023	0.039
$nJets \geq 2$; $3 \geq nbjets \geq 2$	Single-Lepton Triggers	3.15	3081.84	2368.85	0.102	0.057
	Di-Lepton Triggers	2.88	2493.95	1867.76	0.115	0.058
	Single- and Di-Lepton Triggers	3.20	3108.85	2388.23	0.103	0.057

Table 4.6: Events yields in different preselection regions for events passing single-lepton triggers only, di-lepton triggers only and the logical OR of single- and di-lepton triggers. The impact of di-lepton triggers found to be negligible.

4.3.2 Electrons

Electron is one of the stable particles that interact primarily via the electromagnetic interaction and is a final state lepton candidate in this analysis. It is therefore crucial to effectively reconstruct electrons originating from the prompt decay of particles and to identify them with high efficiency, along with isolation from misidentified hadrons, electrons from photon conversions, and non-isolated electrons originating from heavy-flavour decays.

The likelihood-based electron identification [61, 62] is used as recommended by the E/gamma CP group. It provides an improved background rejection with respect to the cut-based electron identification. It is possible to support a variety of working points (WPs), each of which corresponds to a distinct level of prompt electron efficiency and non-prompt electron rejection. For the electron selected for the analysis regions, a `tightLH` identification is used while pre-selected electrons require a `looseAndBLayerLH` identification. Pre-selected electrons need to pass $p_{\mathrm{T}} > 10$ GeV, and $|\eta| < 2.47$. Furthermore, a requirement on the electron isolation, corresponding to the `PLImprovedTight` ('Prompt Lepton Improved Veto') isolation WP [63, 64, 65]. This isolation WP is defined by a multi-variate likelihood discriminant combining shower shape and track information to distinguish prompt electrons from electron candidates from hadronic jets, γ-conversions and heavy-flavour hadron decays (section 5.1.1). The reconstructed track associated with the electron must pass the requirements $|z_0 sin(\theta)| < 0.5$mm and $|d_0|/\sigma(d_0) < 5$, where z_0 describes the longitudinal impact parameter (IP) relative to the reconstructed primary vertex, d_0 is the transverse impact parameter relative to the beam axis, and $\sigma(d_0)$ is the uncertainty on d_0. Electron candidates are excluded if their calorimeter clusters lie within the transition region between the barrel and the endcap of the electromagnetic calorimeter, $1.37 < |\eta^{\text{clust}}| < 1.52$. The associated scale factors (SFs) for electron reconstruction, identification, and isolation are applied in MC, to correct for the efficiency differences between data and simulation if applying these requirements [66].

As there are two leptons of the same sign in the final state of this analysis channel, there is significant background contribution from mis-identification of the electrical charge of electrons. In order to reduce the contribution from electron charge mis-identification a specific selection criterion on electron (on top of the above mentioned Identification and Isolation requirements) were applied using 'Electron Charge ID Selector Tool' (ECIDS) [67]. This selection tool based on a boosted decision tree developed by the Egamma Combined Performance group of the ATLAS Collaboration. The BDT discriminator takes electrons with correctly reconstructed charges as signal events and charge-misidentified electrons as background events. To avoid the mismodelling of charge misidentification sources in Monte Carlo, the algorithm is trained using the datasets in $z \to ee$ decays. Input quantities to the BDT are:

- electron p_T and η
- charged transverse parameter (product $Q \times d_0$)
- the ratio of energy measurements taken by the calorimetry and tracking systems (E/p)
- average charge of all tracks matched to the electron weighted by their number of hits in the SCT detector
- $\Delta\phi$ between the cluster position in the second layer of the EMCAL and the momentum-rescaled track, extrapolated from the perigee, times the charge Q

Using `TightLH` electron isolation, the tool provides 40% reduction for the charge-misidentified electrons background as shown in table 5.9.

A fraction of the fake electrons are also due to photon conversions that pass the tight electron selection. Generally, half of those conversions are internal conversions, namely photons with a virtual mass larger than twice the mass of electrons, converting to a pair of electrons at the interaction point. The other half of photon conversion caused by the interaction of photons with the detector material. In order to identify and suppress such false electronic backgrounds, cuts on the `DFCommonAddAmbiguity` and `ambiguityType` variables are applied, as defined by the 'Electron Ambiguity Tool' in the E/gamma derivation framework [69]. The requirement '`ambiguityType` = 0' together with '`DFCommonAddAmbiguity` ≤ 0' corresponds to an selected electron with a veto on internal/material γ-conversion candidates. All optional options of `ambiguityType` and `AddAmbiguity` and their corresponding meanings are listed in table 4.7 .

selection	`ambiguityType`	`AddAmbiguity`
−1	–	no second track
0	electron	a second track but no conversion
1	ambiguousTrackEoverPBetterThanVertexEoverP	internal conversion
2	ambiguousTrackLowPt	material conversion
3	ambiguousTrackLowEoverP	–
4	ambiguousTrackNoPixel	–
5	ambiguousVertexEoverPBetterThanTrackEoverP	–
6	photon	–
7	unknown	–

Table 4.7: All selection options of `ambiguityType` and `AddAmbiguity`.

The requirements for pre-selected electrons to be used in the analysis are summarised in table 4.8 (left).

4.3.3 Muons

Pre-selected muons have to pass $p_{\mathrm{T}} > 7$ GeV, $|\eta| < 2.5$ as used for the overlap removal. The `medium` identification criteria defined by the muon CP group [70] should also be passed. This WP establishes requirements on the number of hits in each Inner Detector and Muon Spectrometer subsystem as well as for the significance of the charge-to-momentum ratio q/p [71, 72]. Following the recommendations from the muon CP group [73] (section 4.4.1), the entire event is

	Pre-selected electron	Pre-selected muon
Identification	`looseAndBLayerLH`	`medium`
Acceptance	p_{T} >10 GeV, $\lvert\eta^{\mathrm{clust}}\rvert$ <2.47	p_{T} >10 GeV, $\lvert\eta\rvert$ <2.5
	except $1.37 < \lvert\eta^{\mathrm{clust}}\rvert < 1.52$	
Impact parameter	$\lvert d_0/\sigma(d_0)\rvert$ <5.0	$\lvert d_0/\sigma(d_0)\rvert$ <3.0
	$\lvert z_0 sin(\theta)\rvert$ <0.5mm	$\lvert z_0 sin(\theta)\rvert$ <0.5mm
Overlap removal	section 4.3.7	
	Electron	**Muon**
Identification	`tightLH`	`medium`
Isolation	`PLImprovedTight`	`PLImprovedTight`
Extra selections	ECIDS, e/γ ambiguity-cuts	

Table 4.8: Summary of the electron and muon object definitions. The selection requirements for actual electrons/muons are applied in addition to the pre-selected objects used for the overlap removal(section 4.3.7).

removed if a muon is flagged as 'bad' due to its insufficient momentum resolution. As for the electrons, on top of the criteria for pre-selected muons, the `PLImprovedTight` isolation is applied for muons used in the analysis regions to suppress the contribution from fake/non-prompt muons [63, 64, 65]. The muon selection criteria are summarised in table 4.8 (right).

The recommended cuts for the longitudinal and transverse IPs are applied. The reconstructed track associated with the muon candidate must have $|z_0 sin(\theta)| <$ 0.5mm and $|d_0|/\sigma(d_0) < 3$. In order to correct for the efficiency differences between data and MC, associated SFs for identification and isolation [70] are applied as multiplicative factors to the MC event weight [71].

4.3.4 Jets

Jets are reconstructed using the anti-k_t jet algorithm [74] on particle-flow objects [75]. The radius parameter of this algorithm is set to $R = 0.4$, as implemented in the `Fastjet` package [76] (denoted as `AntiKt4EMPFlowJets` jet collection). The anti-k_t algorithm reconstruct jets with a four-momentum recombination scheme, using topo-clustersas inputs. Jet energy is calibrated to the hadronic scale with the effect of pile-up removed.

The jet definition and b-tagging requirements (section 4.3.5) are summarised in table 4.9. A 'Jet Vertex Tagger' (JVT) [77, 78] is used to select jets, as recommended by the Jet/$E_{\mathrm{T}}^{\mathrm{miss}}$ CP group [79].The jets are selected with $p_T >$ 20 GeV and within a pseudorapidity range of $|\eta| < 4.5$. In addition, JVT > 0.5 is required for jets $p_T < 60$ GeV and $|\eta| < 2.4$, corresponding to the `Tight` JVT WP. For so-called 'forward jets' with $2.5 < |\eta| < 4.5$ and $p_T < 120$ GeV, a special JVT WP (fJVT < 0.4) is applied in addition to a timing-requirement on the jet [80]. The jet calibration is performed using the standard jet calibration procedure recommended by the Jet/$E_{\mathrm{T}}^{\mathrm{miss}}$ CP group, which corrects the jet energy to match on average the true jet energy at particle level and applies an in-situ correction for data [81].

Table 4.9: Summary of the jet selection criteria and b-tagging.

Pre-selected jet	
Collection	`AntiKt4EMPFlowJets`
Acceptance	$p_{\mathrm{T}} > 20$ GeV, $\|\eta\| < 4.5$
Jet Vertex Tagger	JVT > 0.5 if $\|\eta\| < 2.4$ and $p_{\mathrm{T}} < 60$ GeV
	fJVT < 0.4 if $2.5 < \|\eta\| < 4.5$ and $p_{\mathrm{T}} < 120$ GeV
Overlap removal	See 4.3.7
b-tagging jet	
Acceptance	$p_{\mathrm{T}} > 20$ GeV, $\|\eta\| < 2.5$
b-tagging	`DL1r` algorithm

4.3.5 Identification of b-jets

b-tagging is the process of identifying jets that are produced when b-quarks are hadronized (referred to as "bjets"). The purpose of b-tagging is to distinguish b-jets from other types of jets, such as those produced by gluons or other types of quarks (*light*-jets) or c-quarks (c-jets). The jet flavour identification is performed via algorithms that exploit the decay properties of b-hadrons.

In this analysis the multi-variate b-tagging algorithm `DL1r` is used. The `DL1r` tagger, in order to identify b-jets, combines the information from the impact parameters of displaced tracks and topological properties of secondary and tertiary decay vertices reconstructed within the jet [82, 83, 84] . Jets are considered as being b-tagged if the values of the DL1r discriminant is above a certain threshold, hereafter referred to as WPs. Four WPs are defined for the DL1r tagger, corresponding to the 85% , 77% , 70% and 60% of b-jets being selected in $t\bar{t}$ simulated events. In order to have a thorough understanding of the b-tagging performance, the efficiency of the DL1r tagger is measured in collision data. The measurements of the b-jets efficiency [85] and c-jets mis-tag rate [86] are performed using $t\bar{t}$ events while the *light*-jets calibration relies on events containing a Z boson, using a procedure similar to the one presented in Ref. [87]. The correction factors derived by the calibration analyses are applied to correct the simulated events.

4.3.6 Missing transverse momentum

The negative vector sum of the energy deposits in the calorimeter projected onto the transverse plane is used to recreate the missing transverse momentum, with magnitude $E_{\mathrm{T}}^{\mathrm{miss}}$. Using their individual energy corrections, clusters linked to high-p_{T} jets and electrons are further calibrated. A so-called soft term created from tracks that are associated to the hard-scatter vertex but are not associated to any of the reconstructed objects is also factored into the calculation, along with contributions from the p_{T} of the chosen muons. The soft term is included in order to account for low-momentum particles that are not identified among the final state objects [88]. The $E_{\mathrm{T}}^{\mathrm{miss}}$ is taken as a measurement of the undetectable particles, and is affected by energy losses due to detector inefficiencies and acceptance, and by energy resolution.

4.3.7 Overlap removal

After the objects have been identified, overlaps between them are removed to prevent counting physics objects twice. Pre-selected Loose leptons and jets are used for this procedure. The sequence of operations that are performed to resolve these ambiguities, as implemented in the 'harmonised' option in the AssociationUtils package [89]: Any electron found with a track overlapping with any other electron is removed;If a calorimeter muon found to share a track with an electron is removed; If any electron found to share a track with a muon is removed; Any jet found within a ΔR of 0.2 of an electron is removed; also if any electron subsequently found within ΔR of 0.4 of a jet is removed; jet with fewer than 3 tracks associated to it found within ΔR of 0.2 of a muon is removed; Any jet with fewer than 3 tracks associated to it, which has a muon inner-detector track ghost-associated to it, is removed; and in the last if any muon subsequently found within ΔR of 0.4 of a jet is removed.

4.4 2LSS selection strategy

In this section the summary of the basic selection strategy presented. It covers the event pre-selection used in the analysis along with an introduction to the expected main background sources. To distinguish signal from background processes, multi-variate analysis (MVA) methods (see 4.4.4) have been employed. The results depend on the discrimination power provided by MVA using a set of variables. First, the generic event cleaning is covered, then the specific selections are discussed.

4.4.1 Event cleaning

The following selection criteria are used to determine which events are taken into account for the analysis. The cuts are applied sequentially and in the list's specified order. Reference [90] provides more information regarding the event cleaning recommendations.

- **Good Run List:** events must be recorded in a luminosity block that is part of the GRLs listed in section 4.2.2. This requirement is applied only for data events [91].
- **Calorimeter cleaning:** events with error-flags indicating temporary non-functionality of the LAr or tile calorimeter are removed [92].
- **Primary vertex:** events are required to have at least one reconstructed primary vertex (corresponds to `xAOD::VxType::PriVtx`) with at least two associated tracks with $p_{\mathrm{T}} > 400$ MeV.
- **Trigger:** events have to be selected by at least one of the single lepton triggers (electron or muon) described in section 4.3.1.
- **Jet cleaning:** events are required to pass the `LooseBad` set of jet cleaning requirements recommended by the Jet/$E_{\mathrm{T}}^{\mathrm{miss}}$ group [93]. The jet cleaning is intended to remove events with significant energy deposits in the hadronic

and electromagnetic calorimeters from instrumental effects, cosmic rays or non-collision particles. Therefore, an event is rejected if any pre-selected jet ($|\eta| < 4.9$, after the overlap removal) fails the jet quality criteria.

- **Bad muon veto:** following the recommendations from the Muon CP group [73], events containing muons with poor momentum resolution ($\sigma(q/p)/|q/p| > 0.2$) are rejected [71].

4.4.2 Event pre-selection

A pre-selection region is defined by requiring the presence of exactly two light leptons (electrons or muons) with a minimal p_{T} threshold of 10 GeV. The charge of the two leptons is required to have the same sign. The transverse momentum cut is then tightened for the light leptons in order to maximise the signal acceptance and minimise the background contamination. The light leptons are ordered based on their transverse momentum, with the leading lepton having a p_{T} >27 GeV and the sub-leading lepton having $p_{\mathrm{T}} > 20$ GeV. Events with hadronically decaying tau leptons are rejected. The number of jets (including both central and forward jets, as defined in Table 4.9) is required to be between one and six. The 70% working point of the `DL1r` tagger is used to select b-jets. The number of b-jets is allowed in the range between one and three. A loose cut on the $E_{\mathrm{T}}^{\mathrm{miss}}$ is applied with a minimal cut of 5 GeV and an upper cut of 800 GeV. The Table 4.10 shows the event yields of the different processes contributing to the preselection region as predicted by the MC simulation.

4.4.3 Background composition

Several background processes contribute to the 2LSS channel, they can be either reducible or irreducible. A reducible background is most commonly the result of an experimental inefficiency, therefore it can be reduced by improving the experimental performance such as object identification and reconstruction. The most important sources of reducible background are the $t\bar{t}$, W/Z+jets and single-top (t-, tW- and s-channel) processes. These processes can pass the pre-selection requirement due to the presence of fake or non-prompt leptons in the final state. Fake or non-prompt light leptons are objects mis-identified as electrons or muons. They can originate from different sources like electrons/muons from

Process	Yields
tHq	9.96 ± 0.09
tWH	4.43 ± 0.14
charge-flip electrons	6962 ± 8
μ_{HF}	256 ± 8
e_{HF}	131 ± 4
e_{Co}	322 ± 12
Other fakes	126 ± 11
ttW	726.2 ± 2.4
ttZ	164.1 ± 1.0
ttH	125.7 ± 0.4
tZq	82.4 ± 0.7
diboson	294.8 ± 3.2
tWZ,Triboson,s-channel, $t\bar{t}t$, $\bar{t}t\bar{t}t$ VH	47 ± 4
Total background	9242 ± 19

Table 4.10: 2LSS channel pre-selection region yields as predicted by the MC simulation. The uncertainty is statistical only.

meson decays, electrons from γ-conversions (e_{Co}) or from heavy-flavour (μ_{HF} or e_{HF}) hadron decays with associated production of a W or Z boson which decay subsequently to leptons. More details about this background type and how it is estimated in this analysis are given in section 5.2.1. Electrons with mis-identified electric charge ('charge-flip') represent a sizeable source of reducible background. Details about this background type and how it is addressed in this analysis are given in section 5.3.

An irreducible background is a process which final state is identical to the signal under study, hence its contribution is usually harder to reduce. The most important irreducible backgrounds for this channel is the ttW process followed by ttZ, ttH, and diboson production. Other and minor backgrounds are tWZ, tri-boson production, other Higgs boson production modes such as the associated production with a vector boson, VH, vector-boson fusion, and three and four top quark production ($t\bar{t}t$, $\bar{t}t\bar{t}t$).

4.4.4 Multi-variate analysis

In order to exploit the relations of different variables and optimize the signal/background separation process for this channel multi-variate analysis (MVA) methods have been employed. The response variable of the multivariate analysis algorithm is used to define regions enriched in either signal or background. The *XGBoost* python package is used to develop several binary-classifier Boosted Decision Trees (BDTs), which target the tHq: main signal, $t\bar{t}$: as it mostly contributes to non-prompt background, ttW: main irreducible background and Diboson: as used for validation region. Implementation of the BDTs used in the analysis is based on the TMVA package [95] implemented in the ROOT data analysis framework [94]. The BDTs are trained using events passing the pre-selection criteria described in section 4.4.2.

A set of discriminant variables are used as input for the BDTs training. Utilizing transverse momentum, the leptons are arranged, the leading lepton ℓ_1 is the lepton with the highest p_{T} and sub-leading lepton ℓ_2 is the lepton with the softest p_{T}. Leading b-jet is the jet that meets the b-tagging criteria and has the highest transverse momentum. Spectator jet j_s, is the jet that fails the b-tagging condition while maximizing the invariant mass with the leading b-jet. Any jet with $|eta| > 2.5$ is referred to as a forward jet j_f. If a forward jet has the highest transverse momentum among all of the forward jets, it is said to be leading. Every jet with $|\eta| < 2.5$ is referred to as a center jet. Numerous variables are built using the aforementioned leptons and jet definition.

The list of variables used in each BDT is optimised with an iterative approach based on the impact they have in the BDT performance (parametrised by the *Gain* and on the correlation with the other variables. The full set of input variables used in the four BDTs are listed in table A.1, with BDT(tHq), BDT(ttbar), BDT(ttW), and BDT(Diboson) using 28, 19, 29, and 27 variables, respectively, for a total of 52 variables across the four BDTs. Variables are ranked based on their *Gain* value, with high ranking corresponding to high *Gain* values. The relevant ranking plots for the three BDTs is shown in figure 4.3. The three input variables with the highest *Gain* are shown in the figure 4.4 for the four BDTs. The plots shows data and simulation in the preselection region. A cut on the $BDT(tHq) < 0.8$ on data is applied to ensure the blinding of data sensitive to tHq process.

The ROC curve of a BDT is defined as the true positive rate as a function of the false positive rate. The ROC curve quantifies both the separation power and the accuracy of a BDT. In this analysis, the *K-folding* cross-validation method is used to cross check the stability of the BDTs and the possible presence of overtraining. Moreover, the *K-folding* cross-validation method allows to verify that the training performed over a sub-sample of events is representative of the full sample. The ten ROC curves resulting from the $k-$fold cross-validation steps for the four BDTs are shown in figure 4.5. All the ROC curves show a similar behaviour, demonstrating the robustness of the BDTs. The area under the ROC curve, `ROC_AUC`, and the `log_loss` of the BDTs are reported in table 4.11. `ROC_AUC` quantifies the separation power of the BDT (a perfect separation corresponds to AUC ROC=1) while the `log_loss` estimates the correctness of the labeling (a perfect labeling corresponds to log loss=0).

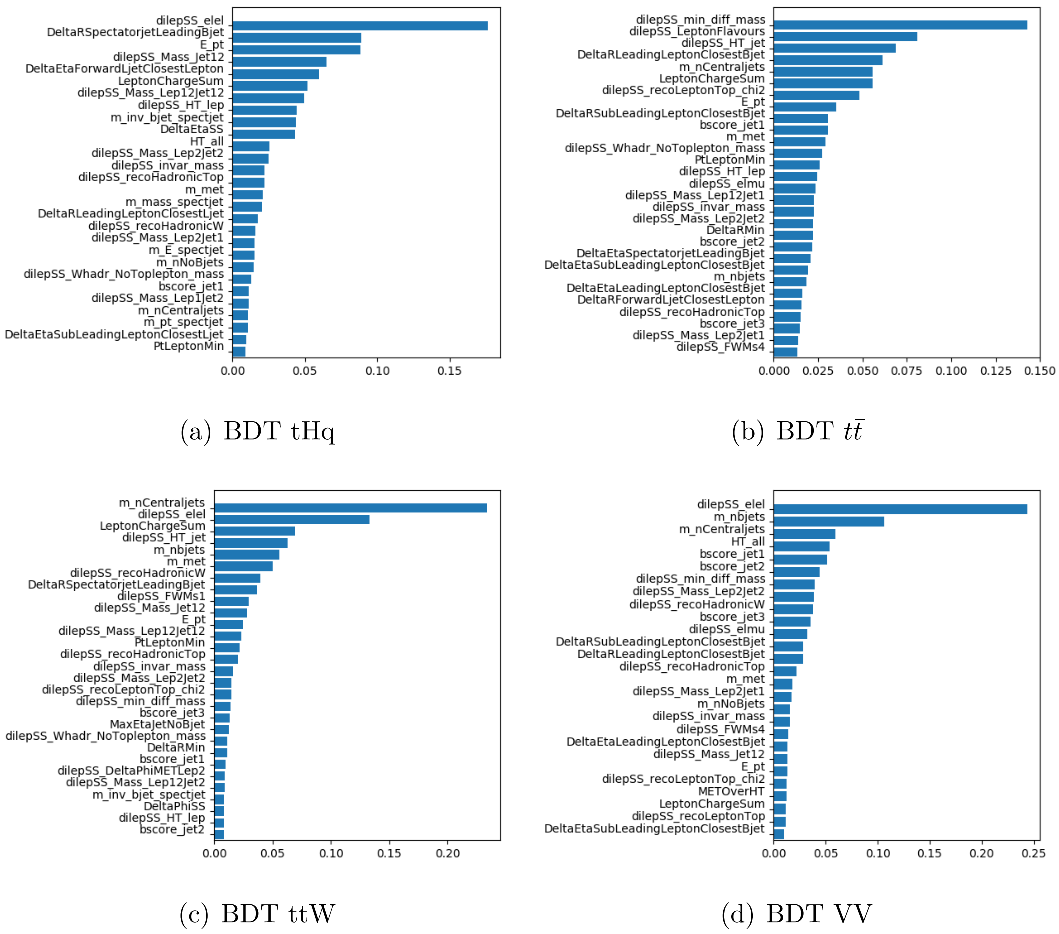

Figure 4.3: Ranking of variables for each BDT. The x-axis corresponds to the value given by the *Gain*.

The BDT parameters are optimized using the Genetic Algorithm (GA) [96] method after the list of input variables is specified. The resulting BDT scores are shown in figure 4.6. Overall a good separation between the target process and the total background is achieved. The comparison between data and prediction for the same distributions is shown in figure 4.7, where a good agreement between

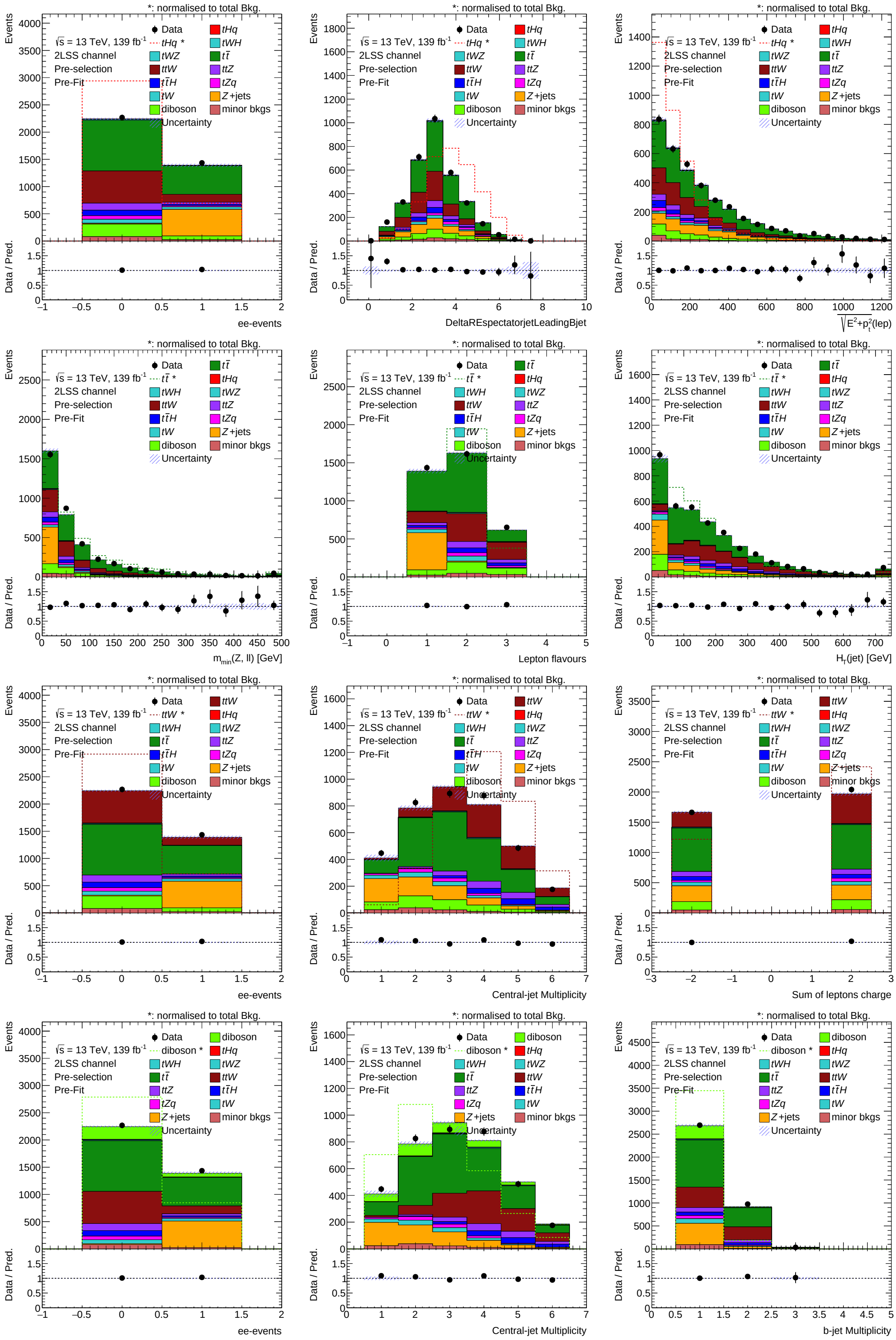

Figure 4.4: The three input variables with the highest *Gain* for BDT(tHq) (1st row), BDT($t\bar{t}$) (2nd row), BDT(ttW) (3rd row) and BDT(VV) (4th row).

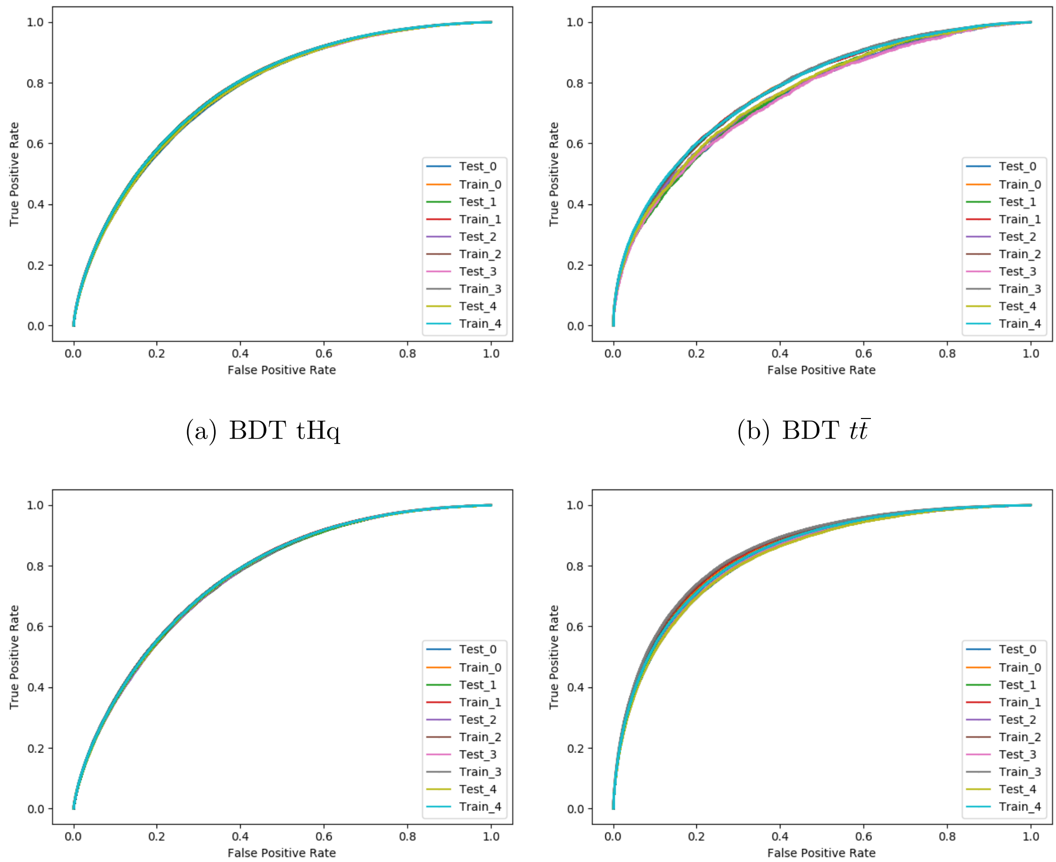

(a) BDT tHq (b) BDT $t\bar{t}$

(c) BDT ttW (d) BDT VV

Figure 4.5: The ten ROC curves resulting from the k-fold cross-validation steps for the four BDTs.

	BDT(tHq)	BDT($t\bar{t}$)	BDT(ttW)	BDT(diboson)
`ROC_AUC`	0.718 ± 0.002	0.673 ± 0.005	0.677 ± 0.001	0.745 ± 0.003
`log_loss`	0.565 ± 0.002	0.434 ± 0.001	0.568 ± 0.002	0.401 ± 0.001

Table 4.11: Values of the `ROC_AUC` and the `log_loss` given by each BDT. The errors associated are given by the statistical error from the $k-$fold cross-validation method.

data and simulation can be seen.

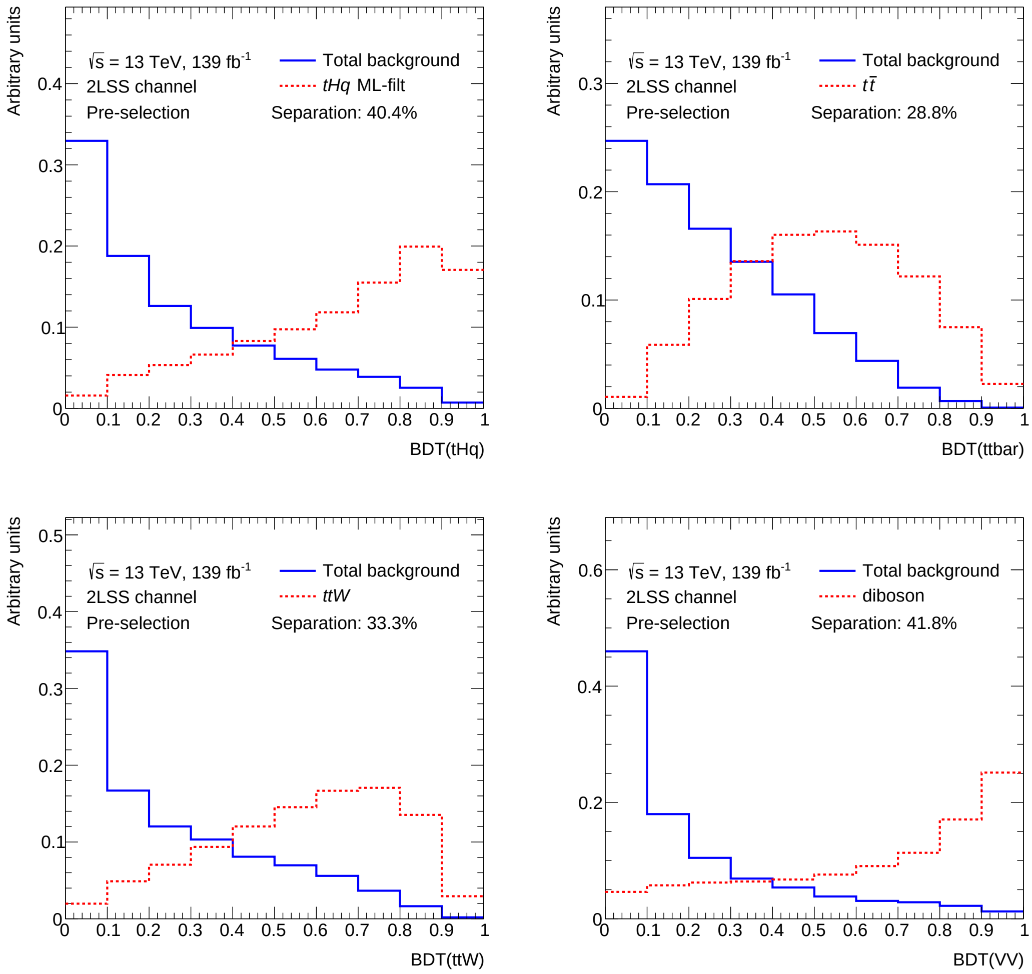

Figure 4.6: BDT score for each BDT in the 2LSS channel. The target process (red dashed lines) and the background samples (blue solid line) are normalised to the same area. In each case the background sample is defined as any sample which is not target.

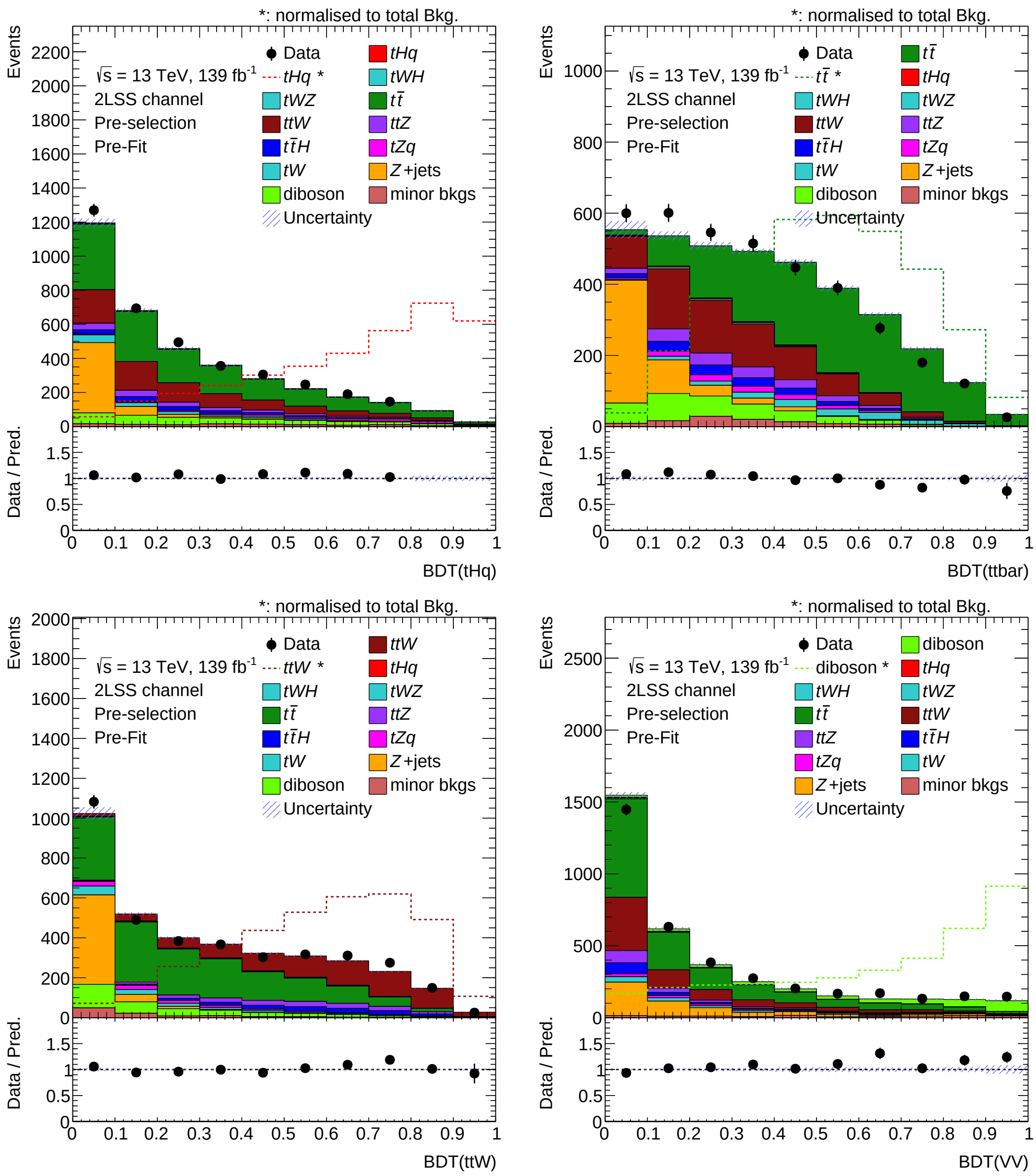

Figure 4.7: BDT score for each of the BDT. A cut on the $BDT(tHq) < 0.8$ on data is applied on data to blind SR-like events. The dashed lines represent the target process of each BDT.

Chapter 5 Background Estimation

The regions determined in the study for the 2LSS channel are described in the section 5.1 of this chapter, along with a categorization method for the MC prompt and non-prompt leptons. The selections used to define the signal region, four control regions and one validation region of this analysis are discussed. The 'Template Fit Method' section 5.2.1, is used as a baseline method to estimate the fake/non-prompt lepton background while the 'Matrix Method' described in section 5.2.2, is used to cross-check the fake-lepton predictions. A data-driven method used to estimate the charge mis-identified leptons background is described in section 5.3. The contribution from irreducible background and its prediction is explained in the last section of this chapter.

5.1 Analysis regions definition

In the analysis, several regions are defined in the 2LSS channel. The SR is required to derive the signal strength $\mu(tHq)$ and is created to maximize the tHq contribution where as the CRs target the main background processes. A mixture of cuts on the BDT outputs (defined in 4.4.4) are used to defined the regions. Some selections also based on a given flavour for the two leptons in the final state or cutting on H_T. The effective ambiguity cut explained in 4.3.2, that reduce the contribution from γ-conversion, is applied to all the electrons. The definition of this cut is inverted for CR(el_{Co}) in order to have more contributions of electrons from γ-conversion in this particular region. Statistically speaking, the regions discussed here are orthogonal to one another. The selections applied to define the SR, CRs and VR is summarized in table 5.1. Three CRs, CR(μ_{HF}), CR(el_{HF}) and CR(el_{Co}) are defined to estimate fake/non-prompt leptons background. These control regions for fake leptons background are chosen so that each region have should have more contribution from specific non-prompt leptons classification based on MC truth information. These sample classification include process $t\bar{t}$, tW, Zjets and Wjets. One control region '$CR(ttW)$' is defined to target the main irreducible ttW background and one validation region VR(VV) is defined to cross-check the data-to-mc modelling of irreducible background which targets the diboson process. In the phase space comparable to the one investigated in the SR, an estimate of the ttW process is derived using the CR(ttW). Section 5.4 contains more information on the modeling of ttW in its CR. The pie charts 5.1, summarised composition of the background in each region and the table 5.2 shows the event yield of the analysis in these regions.

Region	BDT score	Ambiguity cut	Jets	l_1-l_2 flavour	Other
SR	$BDT(tHq) > 0.85$ $BDT(ttbar) < 0.5$ $BDT(ttW) < 0.6$ and $BDT(VV) < 0.8$	yes	-	-	-
CR(μ_{HF})	$BDT(tHq) < 0.85$ $BDT(ttbar) > 0.3$ $BDT(ttW) < 0.6$ and $BDT(VV) < 0.9$	yes	-	μ-μ	-
CR(el_{HF})	$BDT(tHq) < 0.85$ $BDT(ttbar) > 0.3$ $BDT(ttW) < 0.6$ and $BDT(VV) < 0.9$	yes	-	μ / e-e	$H_T(l) < 225$ (GeV)
CR(el_{Co})	$BDT(ttbar) > 0.3$	inverted	-	μ / e-e	M(ll) < 150 (GeV)
CR(ttW)	$BDT(ttW) > 0.6$ $BDT(ttbar) < 0.3$	yes	-	-	-
VR(VV)	$BDT(tHq) < 0.85$ $BDT(ttbar) < 0.5$ $BDT(ttW) < 0.6$ and $BDT(VV) > 0.9$	yes	-	-	-

Table 5.1: The analysis regions selection cuts for 2LSS channel.

5.1.1 MC classification scheme for the identification of prompt and non-prompt leptons

In order to distinguish between fake leptons coming from various underlying processes, prompt electrons/muons as well as non-prompt/fake leptons from various sources are identified and classified in MC. The `TruthClassification` [100] tool provided by the ATLAS Isolation and Fake Forum [63], classify electrons and muons based on their type and origin.

Lepton origin:

Describe from where lepton belongs. The (non-exhaustive) examples below each correspond to a certain origin value:

– W, Z, t, H or τ

– charmed or bottom hadrons, $c\bar{c}$ /$b\bar{b}$ mesons or J/ψ

– BSM particles (SUSY, lepton-quark, . . .)

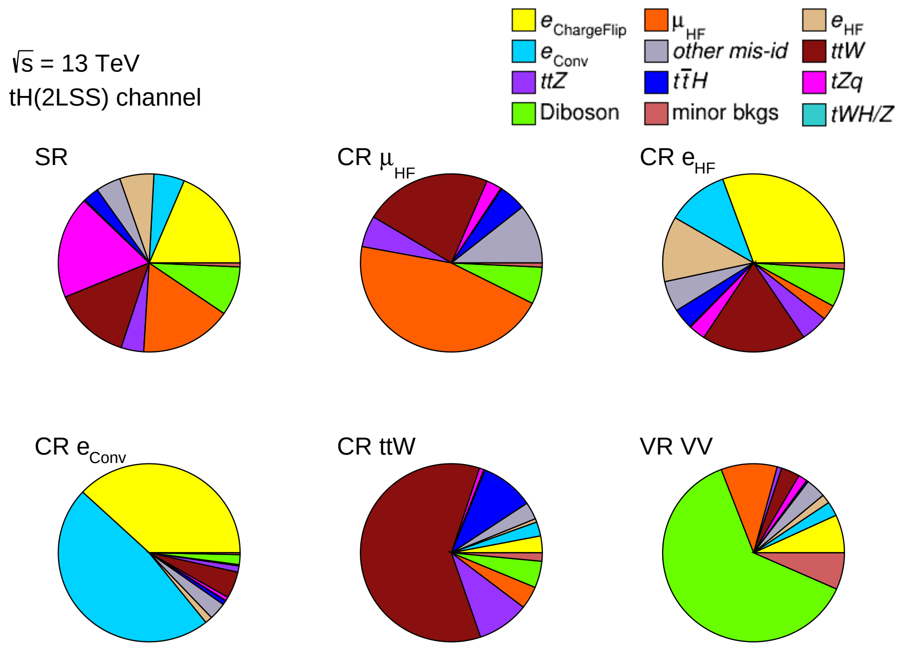

Figure 5.1: Background composition in the 2LSS channel SR and CRs. The minor background contribution includes tWZ, triboson, singletop s-channel, three and four tops production and VH, ggH and VBFH Higgs production modes.

	SR	CR muHF	CR eHF	CR eConv	CR ttW	VR VV
tHq	2.15 ± 0.04	0.57 ± 0.02	2.11 ± 0.04	0.067 ± 0.007	0.40 ± 0.01	0.197 ± 0.012
tWH	0.09 ± 0.01	0.258 ± 0.034	1.03 ± 0.07	0.032 ± 0.012	0.66 ± 0.06	0.022 ± 0.012
el chargeflip	2.5 ± 0.6	0.00 ± 0.00	190 ± 6	42.7 ± 2.8	8.1 ± 1.1	3.9 ± 1.1
muHF	7.4 ± 0.9	62.7 ± 3.0	19.7 ± 1.9	0.24 ± 0.23	11.1 ± 1.2	10 ± 4
eHF	2.8 ± 0.6	0.00 ± 0.00	85.6 ± 3.3	1.3 ± 0.4	1.7 ± 0.5	1.6 ± 0.5
eConv	2.5 ± 1.3	0.00 ± 0.00	80 ± 4	46.2 ± 2.8	6.9 ± 1.1	2.5 ± 2.8
Other	2.0 ± 0.5	14.9 ± 2.1	40 ± 7	3.0 ± 0.7	8.5 ± 1.1	3 ± 6
ttW	6.27 ± 0.23	31.4 ± 0.5	133.8 ± 1.0	4.68 ± 0.18	162.7 ± 1.2	3.21 ± 0.16
ttZ	1.83 ± 0.10	7.84 ± 0.20	35.5 ± 0.4	1.09 ± 0.09	25.2 ± 0.4	0.79 ± 0.06
ttH	1.29 ± 0.04	6.69 ± 0.09	26.83 ± 0.19	0.774 ± 0.032	25.85 ± 0.20	0.293 ± 0.019
tZq	8.45 ± 0.21	3.84 ± 0.14	21.56 ± 0.34	0.66 ± 0.06	2.18 ± 0.11	1.56 ± 0.09
Diboson	4.05 ± 0.29	9.3 ± 0.4	50.0 ± 1.1	1.74 ± 0.20	13.1 ± 0.4	60.8 ± 1.8
minor bkgs	0.33 ± 0.05	1.06 ± 0.09	8.1 ± 1.3	0.32 ± 0.07	4.13 ± 0.05	6.5 ± 2.0
Total background	39.6 ± 1.5	138.0 ± 3.5	692 ± 11	103 ± 4	270.1 ± 2.6	94 ± 5

Table 5.2: Yields of the analysis in SR and different control regions. The sample classified into different fake categories (el chargeflip, μ_{HF}, eHF, eConv and other). The minor backgrounds includes tWZ,Triboson,s-channel, SM4top,ttt, WH, and ZH precess depending on small contribution for event yield in SR. The uncertainties are the statistical only.

Lepton type:
Refers to broader classifications based on a certain origin combination (which was already established by the arrangement of the list above). Leptons are divided into three categories:
– Isolated/prompt: originating from electro-weak boson (including t, H, τ)
– Non-isolated/non-prompt: originating from charmed or b-flavored hadrons
– Background: all the rest

The main aim of the tool is to categorize leptons into different background classes, which are used to measure the true real/fake efficiency, the true charge flip rates and also for investigation on lepton truth-compositions in the signal and control regions of analysis. This tool is interfaced to the `MCTruthClassifier` [101] package and uses its definitions, however it provide to only a reduced set of categories to the user, according to the physics process leading to prompt or non-prompt/fake leptons. The different lepton categories are defined following the recommendations from the egamma and MCP groups, as well as studies performed by the ATLAS Isolation and Fake Forum (IFF [104]) . The following categories for light leptons (electrons and muons) are defined:

Prompt electrons:

An electron is referred as 'prompt electron', if its truth-type = 2, e.g. the type of its e/γ mother-particle belongs to an isolated electron. Also if an electron or its mother-particle originates from an FSR photon (or bremsstrahlung) which afterwards converted, is too referred to as an isolated electron. The E/gamma CP recommendations for electron classification [102] contain this directive. Additionally, electrons from prompt quarkonium decays (e.g $b\bar{b}/c\bar{c} \to e^+e^-$) are also falling into this category.

Prompt muons:

A muon is categorized as a 'prompt muon' if its truth-type (truth-type=6) corresponds to an isolated muon and it comes from a prompt source (such as W/Z bosons, top quarks, or the Higgs boson). The Muon CP recommendations provide more details [103]. Same as in the case of electron, muons from prompt quarkonium decays are considered as prompt.

Prompt γ-conversions:

If the truth-type relates to a background electron (= 4) and it derives from a photon conversion or an electromagnetic process, the electrons (IFF class 5) that result from the 'γ-conversions' of prompt photons are recognized. Additionally, this category is populated if the origin is a prompt photon conversion or an unhadronized photon and the truth type (== 14/16) relates to an isolated or background photon. By looking at the truth-type and origin of the first non-$GEANT4$ mother-particle, it also includes two-step processes like $H \rightarrow \gamma\gamma$ and $\gamma \rightarrow e^+e^-$. Background electrons from γ-conversions (with this info also for the e/γ first mother) with the last mother PDG-ID a photon or an electron are entering in this category.

Charge-flip electrons:

It is possible to distinguish between prompt electrons with correctly assigned and incorrectly identified charge (referred to as 'charge-flip'). If the first non-$GEANT4$ mother particle's charge is different from the electron's reconstruction-level charge, the electron is said to be charge-flipped (for further information can be found at [102]).

Electrons from muons:

If an electron's truth-type (truth-type=3/15) corresponds to a non-isolated electron or photon and its truth-origin is a muon, the electron is categorized as a 'electron from muon'. The contribution from this source should be negligibly small if the overlap removal between electrons and muons is carried out correctly (see Ref. [89]). Additionally, this category contains also electrons from muon bremsstrahlung.

Electrons/muons from τ-decays:

If the truth-type of the leptons corresponds to a non-isolated muon (truth-type=7) or a non-isolated electron/photon (truth-type=3/15) and its truth-origin is a τ-lepton, they are classified as non-isolated electrons and muons from hadronic τ-decays ('electron from τ'). Additionally, the situation in which τ-leptons emit a photon that subsequently transforms into an electron-position pair (($\tau \to \tau\gamma$, $\gamma \to e^+e^-$) is also falling under this heading. To do this, it is necessary to determine whether the lepton is the result of γ-conversions and whether the first e/γ mother particle is a non-isolated electron or photon that originates from a τ-lepton. Electrons and muons from leptonic tau-decays are entering the prompt categories in this classification scheme.

b- and *c*-hadron decays:

Heavy-flavour (HF) electrons and muons can come from *b*-hadron decays or *c*-hadron decays. It is determined whether an electron's or a muon's truth origin relates to a charm-meson or baryon (*c*-type) or a bottom-meson or baryon (*b*-type). The first e/γ mother-particle origin for electrons is also checked, and it must be of the b/c type for either the e/γ mother- or final-state particle.

Light-flavour decays:

It is possible to identify leptons created by light-flavour (LF) jets by determining whether their truth-type (truth-type=17) matches a hadron type. Additionally, a truth-type is deemed to be of the light-flavour if it is a background electron, muon, or photon (truth type = 4/8/16) that comes from a light-meson, a strange-meson, or a light/strange-baryon. The scenario of an intermediary γ-conversion for background electrons (such as $\pi^0 \to \gamma\gamma$, $\gamma \to e^+e^-$) and Dalitz-decays are also taken into account for this category.

Unknown leptons:

If any of the aforementioned classes cannot be applied to a lepton, it will be placed in the category 'Unknown'. Leptons should never belong to this category, ideally. Or, at the very least, their influence on the analysis should to be minimal.

5.1.2 Justification of classification scheme

The default classification used in the `TruthClassification` package differs slightly from the lepton classification system defined in section 5.1.1. In particular, all electrons are regarded as γ-conversion electrons if their truth-origin value is 5. These electrons can be somewhat categorized as 'prompt' according to the default classification system because they can come from FSR photons. Although the default prescription is, for a general application, recommended by the e/gamma group (see Ref. [102]), for the particular phase-space and object definitions of the tHq analysis, these electrons behave more like non-prompt objects.

When examining the lepton efficiencies which is defined as $N(tight)/N(loose)$, shown in figure 5.2, it is clear that electrons with a truth-origin of 5 that are deemed 'prompt' by the `TruthClassification` package have significantly lower efficiencies than other prompt lepton sources (such as those directly originating from W or Z bosons) and are, in-fact, more related to γ-conversions. The same is true for electrons with either applied (Figure 5.2 (left)) or with inverted (5.2 (right)) e/γ ambiguity-cuts (see 4.3.2) ambiguity-cuts. As a result, the slightly modified classification method described in the preceding section is employed since the behavior of these efficiencies suggests that the default classification system is not entirely applicable for the particular situation in the tHq analysis.

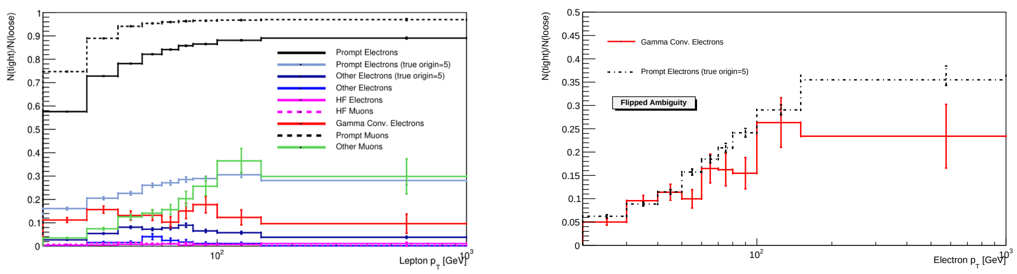

Figure 5.2: Comparison of lepton efficiencies, for different prompt- and fake-leptons categories: (left) shows the efficiencies for prompt and non-prompt electrons/muons with different definitions. (right) shows the efficiencies for γ-conversion electrons and electrons with truth-origin $= 5$ for inverted e/γ ambiguity-cuts.

5.2 Non-prompt lepton background

Lepton candidates are reconstructed from signals in the inner tracker, calorimeters, and muon spectrometer. Identification criteria are then applied to suppress candidates originating from physical objects other than leptons from the hard scattering process of the event. Objects that are misidentified as electrons or muons are known as fake or non-prompt leptons. They can come from a variety of sources, including light jets that mistakenly produce detector signatures resembling light leptons, electrons/muons from meson decays and electrons from γ-conversions. The majority of times, non-prompt leptons originate from heavy-flavour (HF) hadron decays, with associated production of a W or Z boson that further decays to leptons. A semi-data-driven technique known as the 'Template Fit Method' is used to estimate the contributions of non-prompt/fake electrons or muons in the analysis. In this sense, 'semi-data-driven' refers to methods where the kinematic distributions (or 'shapes') are simulated by MC while the overall normalization of the fake-lepton contribution is acquired from data. 'Fully data-driven' approaches aim to completely avoid using simulation. The Template Fit Method's is used as nominal method for non-prompt/fake lepton background estimation while fully data-driven strategy known as the 'Matrix Method' [105], is used as cross-check, which is explained in section 5.2.2.

5.2.1 Template Fit Method

In order to estimate fake/non-prompt light leptons, the template fit method is used. The template fit method is a semi-data-driven approach, it uses MC sample's truth information to define several categories of fake leptons and their general descriptions of fake kinematics, but it derives the normalization of each type of fake lepton from data. These normalization factors (also called as correction factors) are utilized to correct the fakes from the MC estimates.

The normalization factors for muons from HF: $k\mu_{HF}$, electrons from HF:kel_{HF}, and electrons from γ-conversion:kel_{Co} are extracted using three CRs. The CRs' composition is displayed in figure 5.1. In each of these regions, the H_T variable is employed as template, and its binning is optimized to have statistical uncertainty at the bin level that is less than 20–25%. The misidentified lepton normalization factors are estimated using a binned profile likelihood fit. A conservative uncertainty of 50% is applied to the normalisation of the 'other mis-identified leptons' category.

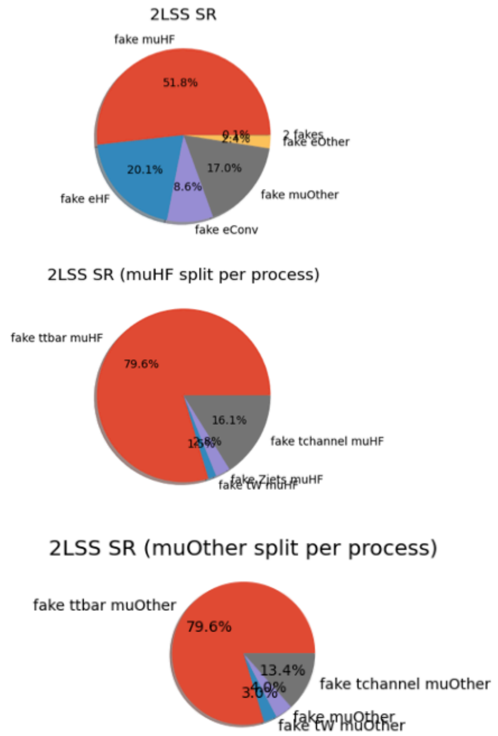

Figure 5.3: Fake leptons composition in signal region split by lepton origin (top left) and physics process for electrons from HF (top right), muons from HF (middle left), electrons from γ conversion (middle right) and muons other (bottom left).

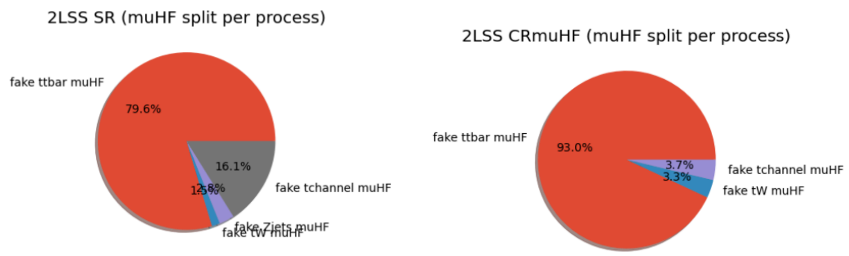

Figure 5.4: Comparison of physics processes giving a μ_{HF} in the SR (left) and CR(μ_{HF}) (right) in the 2LSS channel.

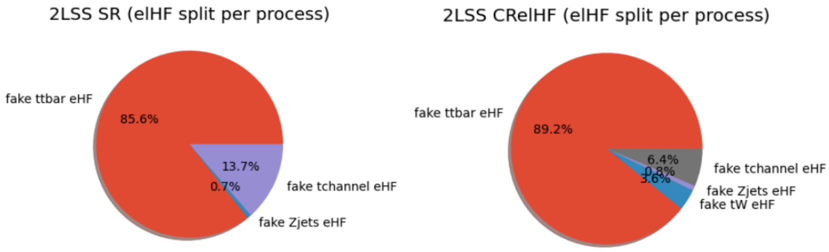

Figure 5.5: Comparison of physics processes giving an el_{HF} in the SR (left) and CR(el_{HF}) (right) in the 2LSS channel.

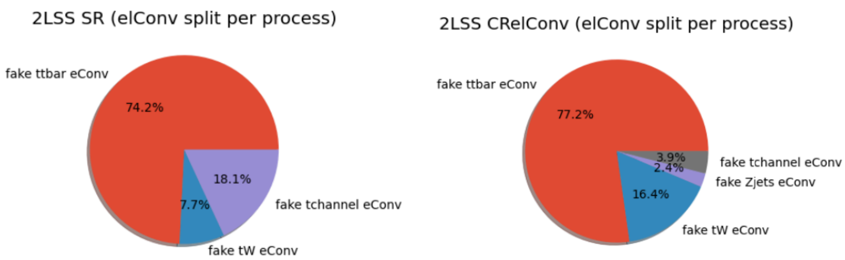

Figure 5.6: Comparison of physics processes giving a el_{Co} in the SR (left) and CR(el_{Co}) (right) in the 2LSS channel.

Mis-identified leptons composition in SR and CRs

In the signal region of the analysis, different components of the fake lepton background are summarized in Figure 5.3, separated by lepton origin (HF, γ conversion, or others), and physics process (ttbar, Zjets, tW and single-top t-channel). For all of the fake lepton origins, it turns out that ttbar is the main physics process causing the fake lepton background. The fraction of events being produced by ttbar, Zjets, tW and single-top t-channel processes is showed for HF muons in their devoted $CR(\mu_{HF})$ in figure 5.4, for HF electrons in respective $CR(el_{HF})$ figure 5.5 and for γ-conversion electrons in $CR(el_{Co})$ in figure 5.6. It is observed that the contributions of ttbar, Zjets, tW, and single-top t-channel in the various CRs are comparable to those in the SR. It can be said that the phase space being explored by the CRs specified for the Template Method and the one in the SR are similar.

Variables used for templates

The variables used to produce the template in each region are determined by the extent to which they can distinguish between the major backgrounds and the target fake lepton category figure 5.7 (in these regions diboson and ttW). The binning is optimized to have a statistical uncertainty for each bin that is less than 20 to 25 percent.

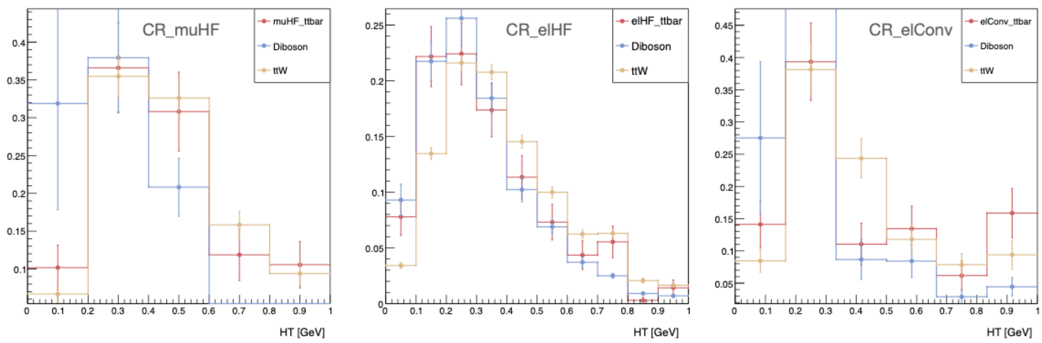

Figure 5.7: Template Method variable used in the CR(μ_{HF}) (left), CR(el_{HF}) (centre) and CR(el_{Co}) (right). The red curve shows the target fake lepton category in that particular CR, the blue curve shows diboson events while the yellow curve shows ttW events.All histograms are normalised to unity. The uncertainty is statistical only.

Template Fit Method results

The agreement between data and prediction before ('pre-fit') and after ('post-fit') the fit is shown in figures 5.8 and 5.9. The fit is performed using binned profile likelihood fit as explained in section 6.2. Post-fit distributions represent a good agreement, with χ^2 probability larger than 80% for the fake control regions. The electron charge flip background is estimated using separate data-driven technique explained in section 5.3.

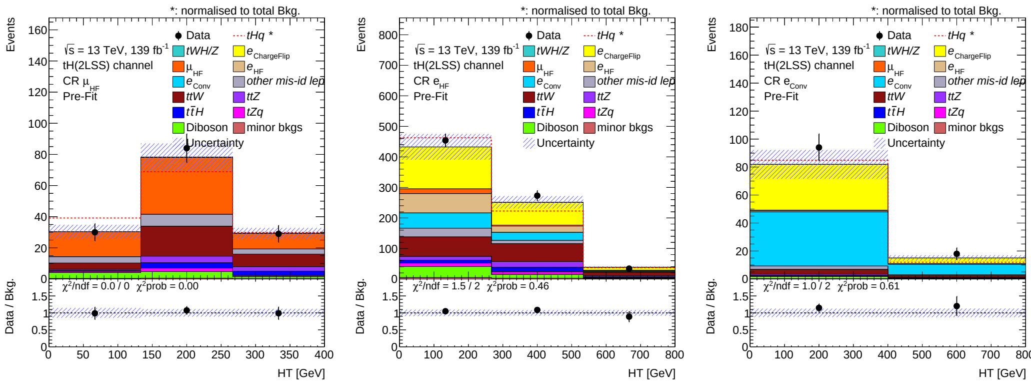

Figure 5.8: Pre-fit plots of the CR(μ_{HF}) (left), CR(el_{HF}) (centre) and CR(el_{Co}) (right) used in the Template Fit Method mis-identified lepton background estimation.

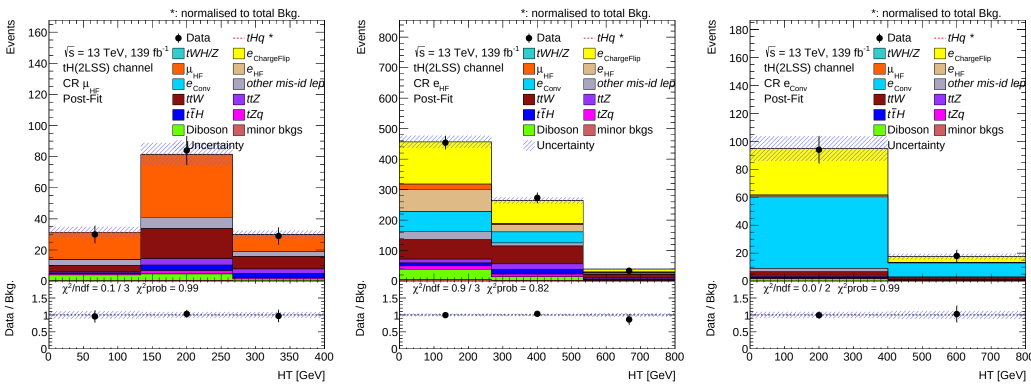

Figure 5.9: Post-fit plots of the CR(μ_{HF}) (left), CR(el_{HF}) (centre) and CR(el_{Co}) (right) used in the Template Fit Method mis-identified lepton background estimation.

In order to have an estimate of the dependence of the fake lepton background estimation from the MC shape of the Template Method variable a one-bin fit is performed and the results are compared in Figure 5.10 (red). Additionally, a check on the effect of the ttW mis-modelling on the Template Method is undertaken considering the significant contribution of the ttW process in the CRs examined by the Template Method. The fit takes into account the CR(ttW) and a normalization factor for ttW. The result are shown in figure 5.10 (blue). The test shows stability and good closure of the results produced with the Template Fit Method: the normalisation factors are robust against the dependency on the shape of the fitted variables and the correction factors of the ttW process. The resulting values of the normalisation factors are shown in figure 5.10. The normalisation factors values for different control regions are found to be compatible with unity within 2σ.

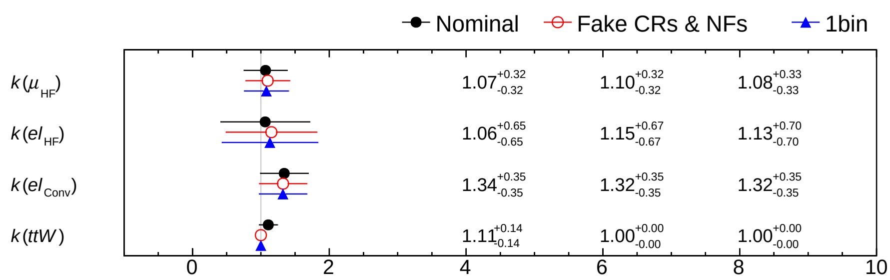

Figure 5.10: Normalisation factors for the μ_{HF}, el_{HF} and el_{Co} categories in the designed CRs. The uncertainty includes statistical and systematic effects. The black points show the results fitting over a binned distribution in all the CRs, the red points show the same fit result but fitting only on the fakes CRs while the blue points show the results without relying on the variables shape.

5.2.2 Non-prompt lepton estimation via the Matrix Method

As compared to the MC template method which is a semi-data drive, the 'Matrix-Method' [105, 106] is a fully data-driven technique, works as a suitable cross check for the Template Fit method results. The matrix method depend on defining two tiers of lepton selection criteria, called the *baseline* and *tight* criteria. The leptons passing the nominal selection cuts are referred to as *tight* leptons. These are the events selected with the same criteria as in the SRs. Where as baseline criteria accept all of the tight lepton candidates as well as an additional set of candidates with a looser selection requirements. The selection criteria is based on identification, isolation and impact parameter requirements defined in table 5.3. The ID WP is relaxed to **looseAndBLayerLH** for the looser electron selection. No isolation requirements are applied for electrons and muons in the looser selection.

	Loose electron	Loose muon
Identification	`looseAndBLayerLH`	`medium`
Acceptance	p_{T} >10 GeV, $\lvert\eta^{\mathrm{clust}}\rvert$ <2.47	p_{T} >10 GeV, $\lvert\eta\rvert$ <2.5
	except $1.37 < \lvert\eta^{\mathrm{clust}}\rvert < 1.52$	
Impact parameter	$\lvert d_0/\sigma(d_0)\rvert$ <5.0	$\lvert d_0/\sigma(d_0)\rvert$ <3.0
	$\lvert z_0 sin(\theta)\rvert$ <0.5mm	$\lvert z_0 sin(\theta)\rvert$ <0.5mm
	Electron	Muon
Identification	`tightLH`	`medium`
Isolation	`PLImprovedTight`	`PLImprovedTight`

Table 5.3: Summary of the electron and muon object definitions. The selection requirements for actual electrons/muons are applied in addition to the pre-selected objects used for the overlap removal (4.3.7).

Leptons that pass the baseline criteria but not the tight criteria are referred as *loose* leptons. The fraction of real(fake) leptons in the baseline sample that pass the tight criteria is know *Real(fake)* efficiency. The real and fake efficiencies are denoted by ϵ_r and ϵ_f respectively. The real/fake efficiencies for electrons and muons are measured in dedicated control regions enriched in fake/real leptons. Both fake and real efficiencies are parametrised in p_T and $|\eta|$ of the respective electron or muon. By knowing the efficiencies, a simple counting of the numbers of lepton candidates that satisfy the baseline and tight criteria provides an estimate for the number of fake/non-prompt leptons. The fundamental notion underlining the matrix approach can be efficiently presented in a simplified scenario where only one lepton is taken into account. The relationship between the numbers of baseline and tight leptons and the composition of the sample in terms of real and fake/non-prompt leptons is shown via a system of two equations:

$$\begin{aligned} N^t &= \epsilon_r N_r^b + \epsilon_f N_f^b \\ N^l &= \not\epsilon_r N_r^b + \not\epsilon_f N_f^b \end{aligned} \tag{5.1}$$

In matrix form:

$$\begin{pmatrix} N^t \\ N^l \end{pmatrix} = \begin{pmatrix} \epsilon_r & \epsilon_f \\ \not\epsilon_r & \not\epsilon_f \end{pmatrix} \begin{pmatrix} N_r^b \\ N_f^b \end{pmatrix}$$

where $\epsilon_r(\epsilon_f)$ represent the efficiency for a real (fake) lepton to pass tight selection, and $\not\epsilon_r \equiv (1-\epsilon_r)(\not\epsilon_f \equiv (1-\epsilon_f))$ represent the probability for a real (fake) lepton to fail tight but still pass baseline selection. N^t and N^l are the numbers of events with tight and loose lepton candidates, N_r^b and N_f^b are the unknown numbers of real and fake/non-prompt leptons in the baseline sample. In matrix notation, the relationship is given by:

$$N_{tl} = M_\epsilon N_{rf}^b \tag{5.2}$$

The name of this method 'Matrix-Method' is due to the fact that the measured numbers (N^t, N^l) and the values of interest (N_r^b, N_f^b) are related via the matrix M_ϵ. In order to determine N_f^b , the inversion of the matrix gives:

$$N_f^b = \frac{1}{(\epsilon_r - \epsilon_f)}[(\epsilon_r - 1)N^t + \epsilon_r N^l)] \tag{5.3}$$

The quantity of interest is the number fake/non-prompt which pass the tight selection N_f^t, is related to the number of such events in the baseline sample N_f^b as in equation 5.4. Similarly, the number of real leptons in the tight sample can be found as in equation 5.5, and we can treat these as elements of a column matrix N_{rf}^t.

$$N_f^t = \epsilon_f N_f^b \tag{5.4}$$

$$N_r^t = \epsilon_r N_r^b \tag{5.5}$$

An improved application of the Matrix Method is described in Ref. [107, 108]. It evaluates the total number of fake electrons and muons entering specific regions via the maximisation of a likelihood function. In this method the elements of N_{rf}^t are treated as free parameters, which are varied to maximize the likelihood of the observed N_{tl} values. The n_{rf}^t values are first transformed to N_{rf}^b using Eqs. 5.4 and 5.5, where the values for the entries in the matrix M_ϵ are determined by averaging the efficiency of the prompt and fake/non-prompt leptons in the baseline sample:

$$M_\epsilon \quad = \begin{pmatrix} \langle\epsilon_r\rangle & \langle\epsilon_f\rangle \\ 1-\langle\epsilon_r\rangle & 1-\langle\epsilon_f\rangle \end{pmatrix}$$

Using Eq. 5.2, the resulting N_{rf}^b values are utilized to determine the N_{tl} expectation values. These N_{tl} expectation values are referred to as $N_{tl,exp}$. The N_{rf}^t parameters are adjusted to maximize the joint Poisson likelihood, subjected to the restriction that they must not be negative.

$$\mathcal{L}(n_{rf}^t) = \prod_i P[N_{tl,obs_i} | N_{tl,exp_i}(n_{rf}^t)] \tag{5.6}$$

where the product is over the elements of N_{tl}, and $P[n|\mu]$ is the Poisson probability for observing n events when μ are expected. The primary advantages of the Poisson likelihood approach are that the result is constrained to be non-negative and provide better approximation of uncertainty particularly in low-statistics samples. Therefore, this method offers a more robust fake-lepton estimation for statistically limited regions, compared to the linear version of the method (as e.g. described in Ref. [109]). The main drawback is that the estimated yield must be calculated for the sample as a whole rather than from a sum of individual event weights, which complicates the process of producing a distribution of the fake lepton yield. In order to overcome this problem the data events that are input to the fake/non-prompt background estimation are weighted using the scaled Poisson distribution.

$$s_{tl} = \frac{\sum_{tl,obs} w_{obs_i}}{\sum_{tl,obs} w_{obs_i}^2} \tag{5.7}$$

The values of N_{tl,exp_i} and N_{tl,obs_i} from Eq. 5.6 are scaled by s_{tl} according to the event weights w_{obs_i}:

$$\mathcal{L}(n_{rf}^t) = \prod_i P[N_{tl,obs_i}/s_{tl}|N_{tl,exp_i}(n_{rf}^t)/s_{tl}] \tag{5.8}$$

In our analysis case, there are two lepton candidates satisfying the baseline selection which could be fakes, the method explained as above can easily be applied by increasing the dimensionality of M_ϵ, N_{tl}, and N_{rf} to 2^{nb}, where nb is the number of baseline lepton candidates in each event(which in our case is =2)

$$\begin{pmatrix} N^{tt} \\ N^{tl} \\ N^{lt} \\ N^{ll} \end{pmatrix} = \begin{pmatrix} \epsilon_{r,1}\epsilon_{r,2} & \epsilon_{r,1}\epsilon_{f,2} & \epsilon_{f,1}\epsilon_{r,2} & \epsilon_{f,1}\epsilon_{f,2} \\ \epsilon_{r,1}\not\epsilon_{r,2} & \epsilon_{r,1}\not\epsilon_{f,2} & \epsilon_{f,1}\not\epsilon_{r,2} & \epsilon_{f,1}\not\epsilon_{f,2} \\ \not\epsilon_{r,1}\epsilon_{r,2} & \not\epsilon_{r,1}\epsilon_{f,2} & \not\epsilon_{f,1}\epsilon_{r,2} & \not\epsilon_{f,1}\epsilon_{f,2} \\ \not\epsilon_{r,1}\not\epsilon_{r,2} & \not\epsilon_{r,1}\not\epsilon_{f,2} & \not\epsilon_{f,1}\not\epsilon_{r,2} & \not\epsilon_{f,1}\not\epsilon_{f,2} \end{pmatrix} \begin{pmatrix} N_{rr}^b \\ N_{rf}^b \\ N_{fr}^b \\ N_{ff}^b \end{pmatrix}$$

In order to obtain the number of fakes in signal region as a function of observables, the matrix can be inverted and the final number of fakes in the signal region N_f^t , i.e. the total number of two tight events with at least one fake lepton, can be obtained by:

$$N_f^t = (\epsilon_{r,1}, \epsilon_{f,2})N_{rf}^b + (\epsilon_{f,1}, \epsilon_{r,2})N_{fr}^b + (\epsilon_{f,1}, \epsilon_{f,2})N_{ff}^b \tag{5.9}$$

Fake and real efficiency measurement

The probability of an electron or muon passing the nominal electron/muon requirements are known as the fake and real lepton efficiencies (fake/real rates). They are given by the *tight* over *loose* ratio: N^t/N^l. A dedicated control region defined in table 5.4 is used to measure the fake efficiencies. This CR is orthogonal to the SR and all other CRs in the analysis by applying requirement on all jets $|\eta| < 2.5$. A 'tag-and-probe method' is used to measure the fake lepton efficiencies in data. For the 'tag' lepton a high p_T cut and very stringent isolation requirements are applied and the remaining 'probe' lepton is used for the efficiency measurement. Along with the p_T and isolation, the tag lepton is required to be selected by one of the single-lepton triggers, as listed in section 4.3.1. The strict criteria are applied to the tag lepton to make it more likely to be a prompt lepton and, as a result, make the probe lepton more likely to be a fake.

Region	N_ℓ	Tag lepton	N_{jets}	$N_{b\text{-jets}}$	$\lvert\eta\rvert_{\text{jets}}$
CR(fake-e)	$= 2$ ($e\mu$)	μ, $p_T > 40$ GeV , $\max(p_T^{\text{cone20}}, E_t^{\text{cone20}})/p_T < 0.01$	≥ 1	≥ 1	< 2.5
CR(fake-μ)	$= 2$ ($e\mu$)	e, $p_T > 40$ GeV, $p_T^{\text{cone30}}/p_T < 0.01$	≥ 1	≥ 1	< 2.5

Table 5.4: Definition of the fake-lepton control regions used for the electron CR(fake-e) and muon CR(fake-μ) fake efficiency measurements.

To get an unbiased efficiency measurement, prompt background contributions entering these CRs are evaluated in MC and subtracted from the data. Additionally, based on the MC estimation, the contribution from charge-flip electrons in the $e\mu$(SS) region is subtracted. Studies on the truth composition of the fake/non-prompt leptons showed that the main source of fake/non-prompt leptons in the SRs arises from HF events, which are also the dominant source in the regions used for the measurements (after subtracting prompt lepton contributions and the charge-flip contribution for electrons). The e/gamma and Muon CP groups' recommendations [111, 112] are used to determine the real efficiency. The efficiencies are measured at truth-level and multiplied with the ratio of the SFs for *tight* and *loose* leptons:

$$\varepsilon = \varepsilon_{\text{truth}} \times \frac{\text{SF}(\textit{tight})}{\text{SF}(\textit{loose})}, \qquad \text{SF} = \frac{\varepsilon_{\text{Data}}}{\varepsilon_{\text{MC}}}. \tag{5.10}$$

The real efficiencies at truth-level ($\varepsilon_{\text{truth}}$) are obtained from $Z \to ee/\mu\mu$. The only events used where the electrons/muons classified as 'prompt' by the `TruthClassification` [100] package. The fake and real efficiency are measured binned in $|\eta|$ and p_T of the respective probe electron/muon. The bin ranges are shown in table 5.5. A finer binning can be used for the real efficiencies than for the fake efficiencies measurement because of the high statistics in the MC simulation.

Bin ranges	Lepton p_T [GeV]	Lepton $\|\eta\|$
Real eff. (e)	$[0, 7, 12, 20, 35, 50, \infty]$	$[0, 0.7, 1.37, 1.52, 2, 2.47]$
Real eff. (μ)	$[0, 7, 12, 20, 35, 50, \infty]$	$[0, 0.5, 1, 1.5, 2, 2.5]$
Fake eff. (e/μ)	$[10, 15, 20, 30, \infty]$	$[0, 1.0, 2.0, 2.5]$

Table 5.5: The p_T and $|\eta|$ bin ranges chosen for the fake and real efficiency measurements. The '∞' stands for an inclusive last bin. The binning for the fake efficiencies is chosen to be the same for electrons and muons whereas, for the real efficiencies, a slightly different $|\eta|$ binning has been chosen due to the transition region ($[1.37, 1.52]$).

Figures 5.11 shows the fake efficiencies for electrons (left) and muons (right), where as the electron/muon real efficiencies are shown in figure 5.12. The one-dimensional distributions shown in these figures are projections of the two-dimensional distributions and provide a better illustration of the p_T and $|\eta|$ dependencies of the efficiencies. The fake efficiencies lie in most bins between 1 and 2%, and mostly stable against the lepton p_T and $|\eta|$. There is a slight increase of the values for electrons with high p_t. MC-based fake efficiencies (blue) are also computed for validation purposes, that is mostly compatible which the values obtained from data (black). The real efficiencies starting at around 50% (30%) for muons (electrons) with ≤ 10 GeV, but increase for larger transverse momenta of the leptons. For leptons with p_T larger than 50 GeV, the real efficiencies reach between 90 and 95%. There is a slight decrease of the electron efficiencies for higher $|\eta|$ values, which is an expected behaviour for the isolation WP used in this analysis. The one-dimensional real efficiency distributions for different b-jet multiplicities demonstrate the stability of the truth-level real efficiencies against the number and type of extra jets in the events.

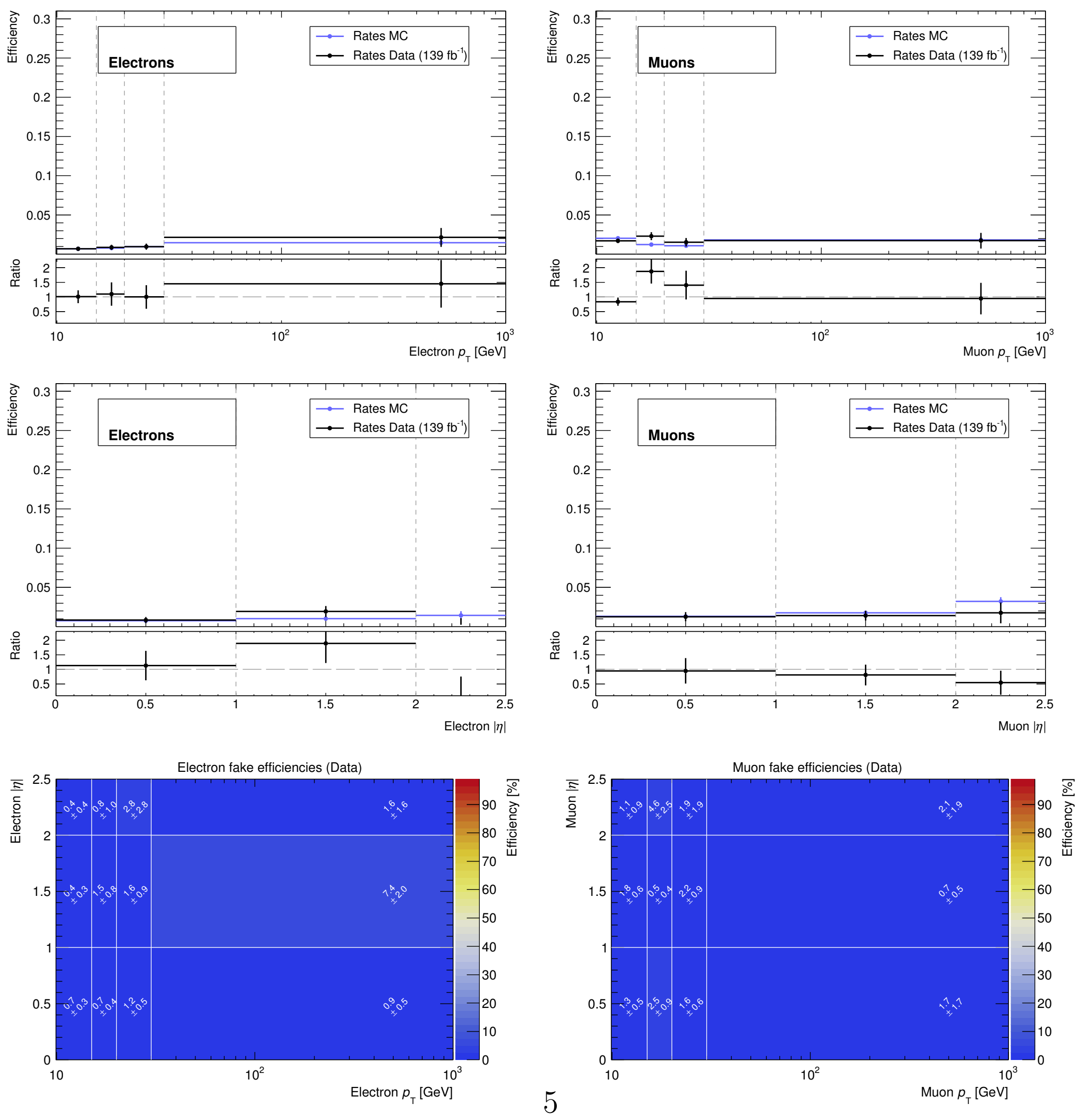

5

Figure 5.11: Fake efficiencies for electrons (left) and muons (right), binned in the lepton p_T (top row), $|\eta|$ (middle row) and in both parameters (bottom row). The one-dimensional parameterisations show the fake efficiencies measured in data (black) and for validation purposes, the MC-based fake efficiencies (blue). The errors include only the statistical uncertainties of the measurements.

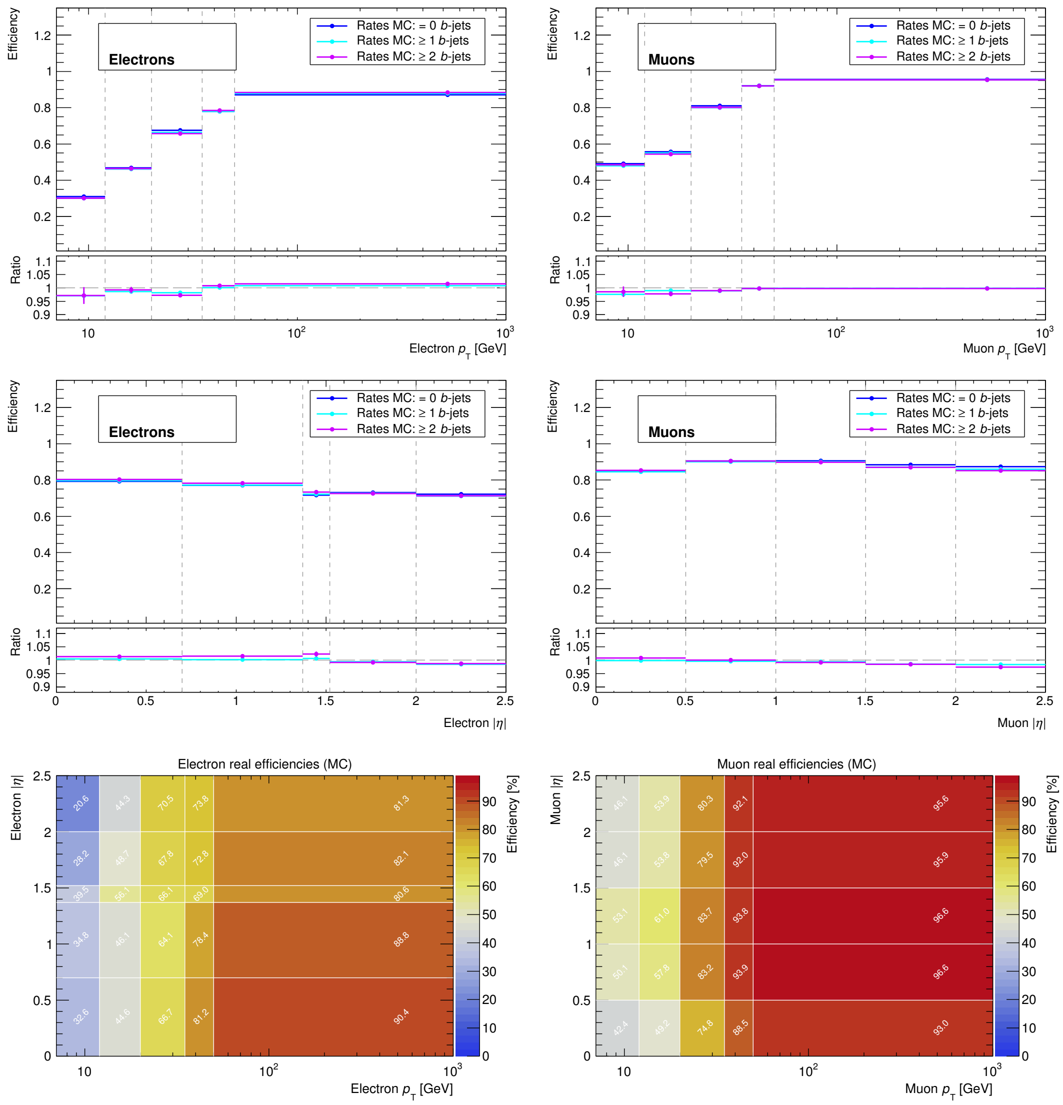

Figure 5.12: Real efficiencies for electrons (left) and muons (right), binned in the lepton p_T (top row), $|\eta|$ (middle row) and in both parameters (bottom row). The errors include only the statistical uncertainties of the measurement.

Validation of the method

A set of regions is defined to validate the fake estimates obtained from this method. These regions include 2LSS pre-selection (section 4.4.2) region, the dedicated CR(μ_{HF}), CR(el_{HF}) for 2LSS analysis (as defined in table 5.1) and two set of validation region based on number of jets/b-jets. The definitions of these regions are shown in table 5.6.

Region	Definition	Fake lepton fraction
2LSS pre-selection	2LSS, p_T^{ℓ} (1st/2nd) = 27/20 GeV $N_{\text{jets}} \in [1,6]$, $N_{b\text{-jets}} \in [1,3]$, $E_T^{miss} \in [5,800]$ GeV	$\approx$ 20%
CR(μ_{HF}) CR(el_{HF})	As defined in table 5.1	60–65%
CR(fake-e/μ)	As defined in table 5.4	$\approx$ 25%
VR($1b3j$)	$N_{\text{jets}} = 3$, $N_{b\text{-jets}} = 1$	$\approx$ 20%
VR($1b3j$-no Z)	$N_{\text{jets}} = 3$, $N_{b\text{-jets}} = 1$, $\lvert m_{OSSF} - m_Z \rvert > 10$ GeV	$\approx$ 40%

Table 5.6: Definition of the validation regions to test the Matrix-Method predictions.

The total expected event yields (i.e. prompt MC plus Matrix-Method fakes) can be compared to data in these regions as shown in table 5.7. In this table, the fake leptons produced by MC (section 5.1.1) are replaced with the fakes estimated from the Matrix Method. The estimation coming from the Matrix Method do not include charge-flip, as the charge-flip contributions is subtracted before the fake rate measurement. In the majority of regions, there is an agreement level of roughly 10% between the data and the overall SM prediction.

Comparisons of the results obtained with the Matrix Method to the the MC-based fake-lepton prediction is also performed. The results as presented for some simple kinematic variables (H_T, N_{jets}, p_T of the second lepton) are shown figures 5.13 and 5.14. No severe mis-modelling of these distributions with the fake estimation from the Matrix Method is observed. Systematic uncertainties of the fake lepton predictions from the Matrix Method lie between 15 and 40%. The differences between data and the estimates shown in table 5.7 are covered by the uncertainties assigned to the method.

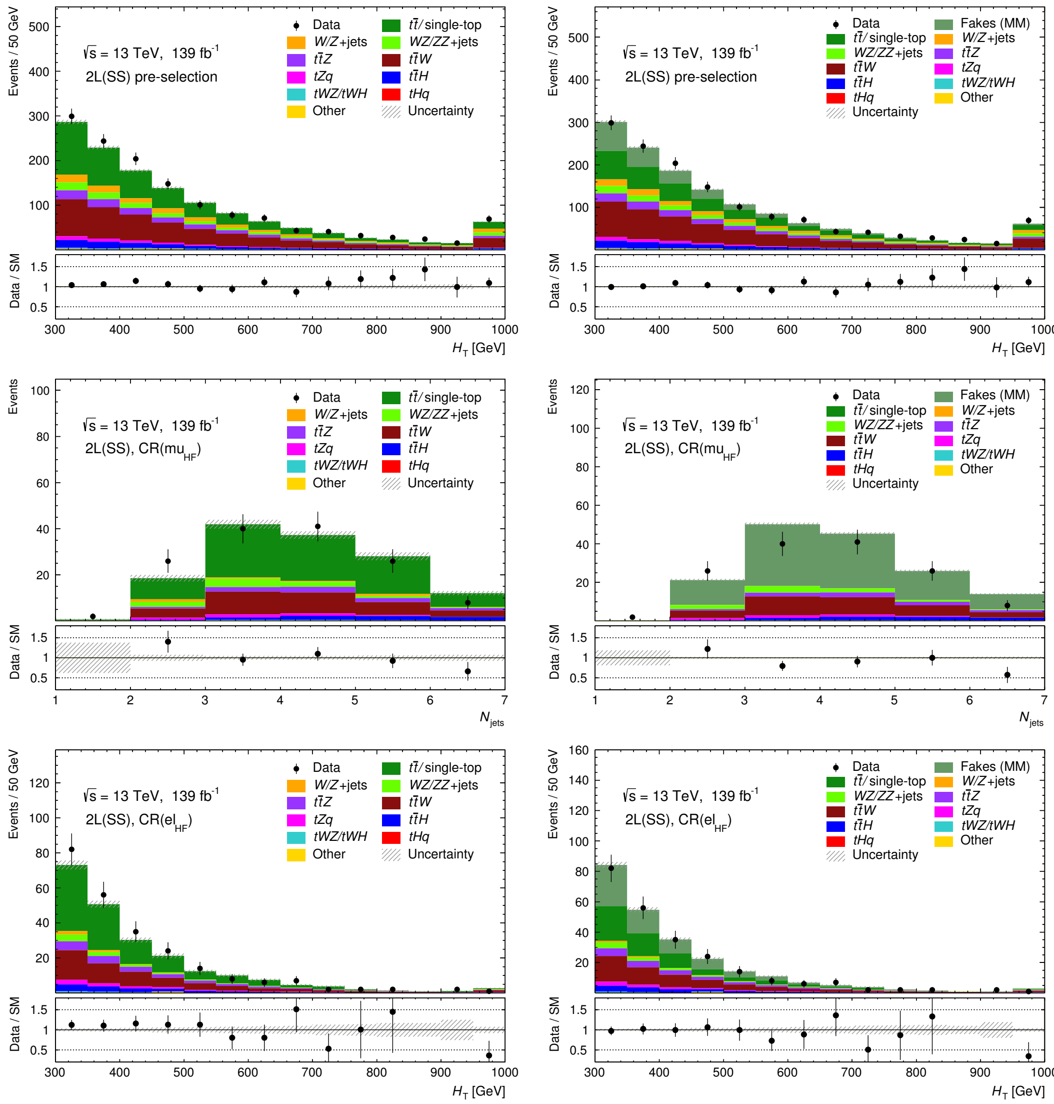

Figure 5.13: Figures (left) show the fake leptons estimated from MC (mainly ttbar, Zjets and Wjets), whereas (right) shows the same distribution with the fake lepton estimation obtained from the Matrix Method. The shaded error-bands include only the statistical uncertainties of the SM predictions. The top row shows H_T in the pre-selection region. Middle plots shows jet-multiplicity in CR(μ_{HF}) and the bottom H_T in CR(el_{HF}).

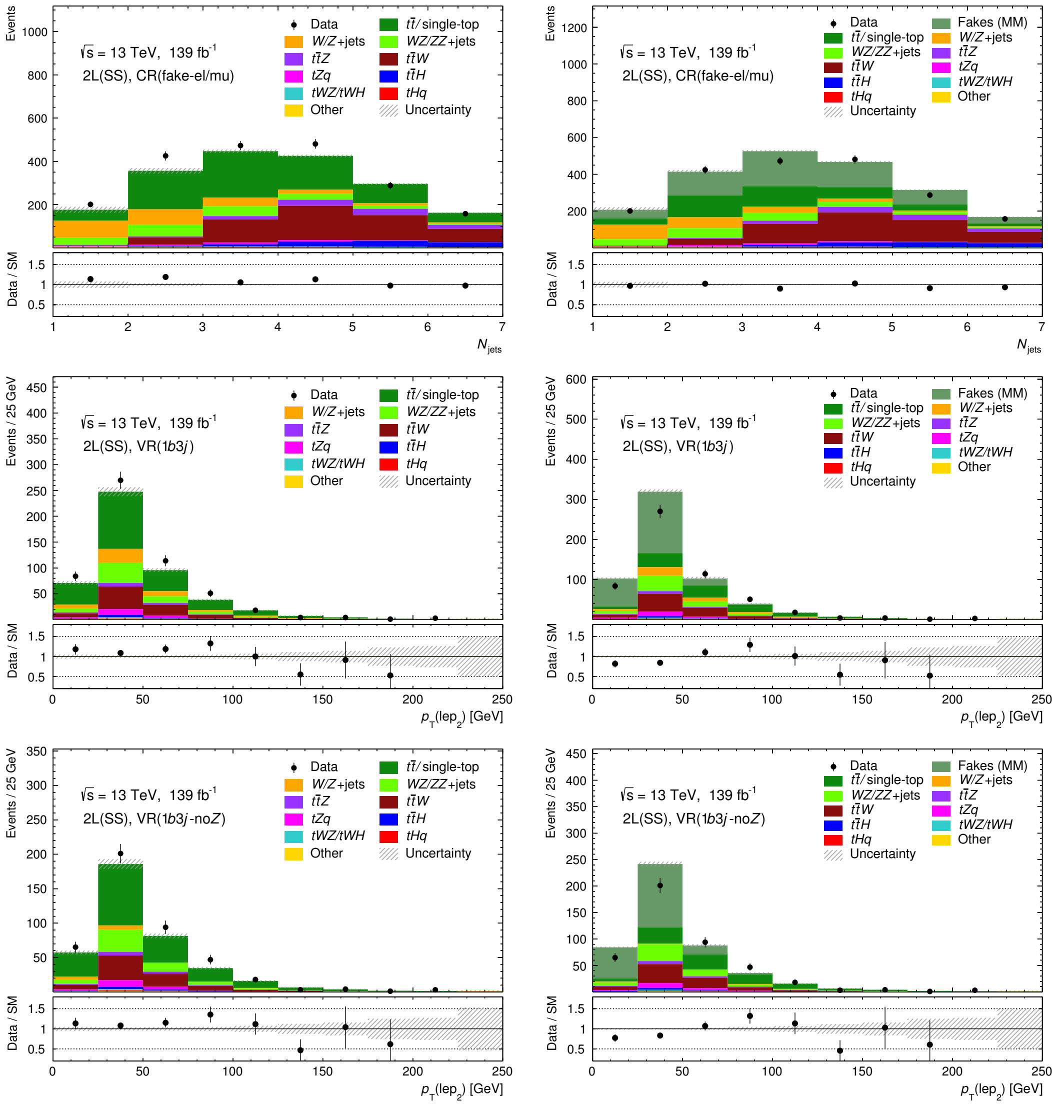

Figure 5.14: Figures (left) show the fake leptons estimated from MC (mainly ttbar, Zjets and Wjets), whereas (right) shows the same distribution with the fake lepton estimation obtained from the Matrix Method. The shaded error-bands include only the statistical uncertainties of the SM predictions. The top row shows the jet multiplicity in CR(fake-e/μ). The middle row shows p_T of the sub-leading lepton in VR($1b3j$), while the bottom shows p_T of the sub-leading lepton in VR($1b3j$-no Z).

	2LSS pre-sel.	CR(μ_{HF})	CR(el_{HF})	CR(fake-e/μ)	VR($1b3j$)	VR($1b3j$-no Z)
WZ/ZZ+jets	279 ±2	9.01 ± 0.40	49.5 ± 0.4	181 ± 1	68.1 ± 0.5	58.5 ± 0.4
ttZ ($Z \to ll$)	158 ± 1	7.79 ± 0.20	35.3 ± 0.4	96.9 ± 0.7	13.0 ± 0.2	11.3 ± 0.2
ttW	702 ± 2	31.4 ± 0.4	134 ± 1	479 ± 2	84.5 ± 0.5	73.5 ± 0.5
tZq ($Z \to ll$)	76.8 ± 0.1	3.82 ± 0.14	20.7 ± 0.3	26.2± 0.4	18.1 ± 0.1	15.5 ± 0.1
ttH	122 ± 1	6.65 ± 0.09	26.6 ± 0.2	83.2 ± 0.3	7.69 ± 0.10	6.50 ± 0.08
tWH/tWZ	22.1 ± 0.2	0.± 0.03	4.87 ± 0.07	13.8 ± 0.1	3.48 ± 0.02	3.03 ± 0.02
tHq	9.70 ± 0.02	0.58 ± 0.01	2.11 ± 0.04	3.58 ± 0.05	1.91 ± 0.04	1.62 ± 0.03
ttbar/single-top	602 ± 4	0.46 ± 0.26	196 ± 4	372 ± 5	109 ± 4	102 ± 4
W/Z+jets	289 ± 3	0.00 ± 0.00	18.7 ± 0.8	206 ± 3	48.0 ± 1.0	9.63 ± 0.51
Other	24.2 ± 0.2	0.12 ± 0.02	3.81 ± 0.06	17.9 ± 0.2	3.72 ± 0.21	3.25 ± 0.15
Fake leptons	981 ± 5	96.4 ± 1.2	380 ± 3	618 ± 3	243 ± 2	198 ± 2
SM total	3266 ± 8	157 ± 2	871 ± 6	2098 ± 7	601 ± 5	483 ± 5
Data	3212	143	761	2026	549	436

Table 5.7: The numbers of observed data and expected background events (prompt MC process and the fake leptons estimated from the Matrix Method) for the validation regions in the 2LSS channel. Only statistical uncertainties of the MC samples are shown here.

Lepton truth-composition in fake lepton control region

The truth-origin for various types of fake/non-prompt electrons and muons entering the SRs can be compared to the types of fake/non-prompt leptons present in the regions used for the fake efficiency measurements. The truth-classification is based in the classification scheme from the `TruthClassification` [100] tool and explained in detail in section 5.1.1. Figure 5.15 shows the truth-compositions of fake electrons (left) and muons (right) in the CR used for the fake efficiency measurement. Only the fake leptons passing the nominal selection criteria described in table 4.8 are shown. The truth-compositions are shown inclusively (a,b) (The 'Electron/muon $|\eta|$' in the x-axis title is not relevant, as only one, inclusive $|\eta|$ bin is used for these plots) and parametrised in the p_T of the leptons using the binning from table 5.5. The dominant fake source for muons is HF fakes, whereas for electrons it is a mixture of fakes coming from HF and γ-conversions (with an increasing γ-conversion-fraction for higher electron p_T).

Uncertainties associated with Matrix Method

A systematic uncertainty can be assigned to account for the differences between the fake lepton truth-compositions in the region used for the fake efficiency

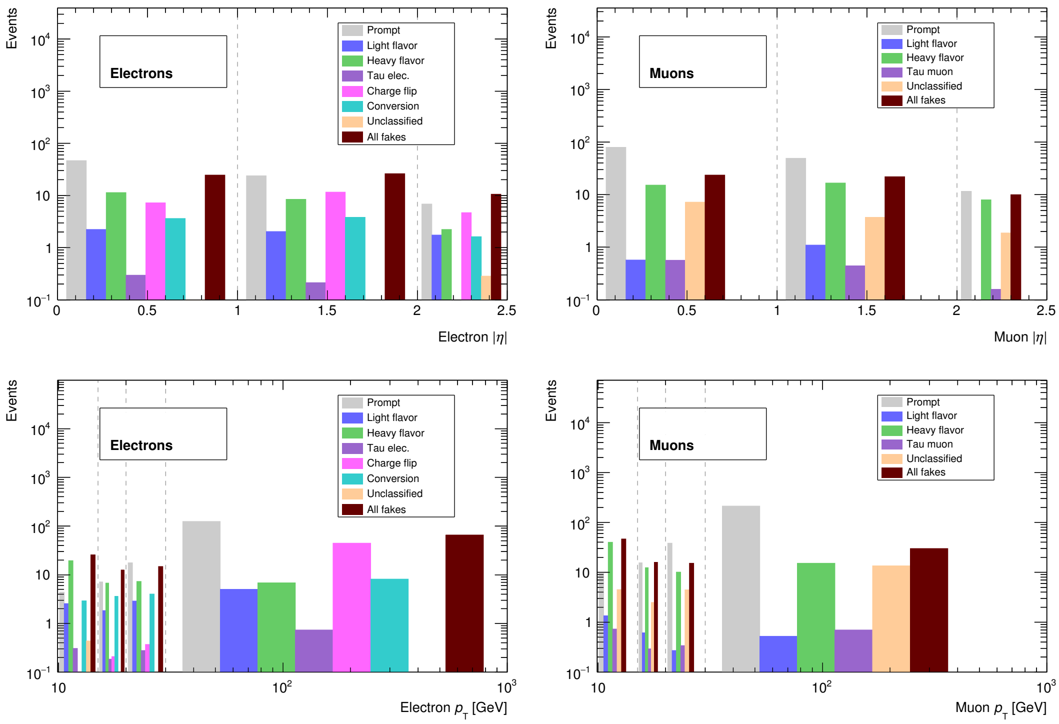

Figure 5.15: Truth composition for fake electrons and fake muons, shown inclusively (top row) and binned in the fake lepton p_T (bottom row) in the region used for the fake efficiency measurement. The contributions from leptons classified as ‘prompt’ and ‘charge-flip’ are subtracted prior the efficiency calculation. The entry ‘all fakes’ refers to the sum of all different fake/non-prompt lepton sources.

measurement and the SRs of the 2LSS channels. The definitions of the SRs can be found in section 5.1. Figures 5.16 shows the p_T-binned truth-composition of the fake leptons in the SRs. Compared to the composition observed in the CR (shown in figure 5.15), the dominant fake lepton sources are very similar: for muons, the dominant contributions in both the CR and the SRs is arising from HF muons, whereas for electrons, it is a mixture of HF electrons and γ-conversions (with an increasing γ-conversion fraction for higher electron p_T). The uncertainty account for the residual differences in the electron/muon truth-composition is quantified by computing the fake efficiencies at truth-level(The truth-level fake efficiencies are computed by deriving the fake efficiencies in MC, but only considering leptons classified as fake or non-prompt (applying the classification scheme described in section 5.1.1).) in the CR, as well as the SRs and using the relative differences between them as uncertainties. It should be noted that with this approach, not just the differences in the lepton truth-composition, but also any other SR/CR differences (e.g. differences in E_T^{miss}, H_T or N_{jets}, $N_{b\text{-jets}}$) are taken into account.

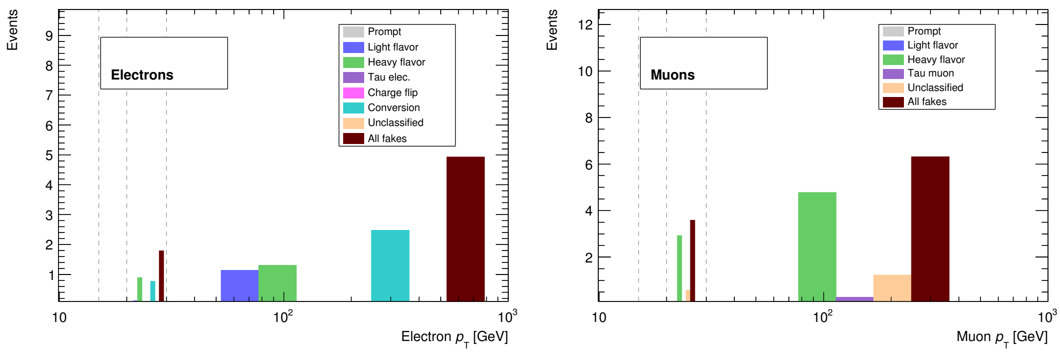

Figure 5.16: Truth-compositions of fake leptons in the SRs. The compositions are shown for electrons (left) and muons (right) binned in the respective lepton p_T.

The plots in figure 5.17 shows the truth-level fake efficiencies for electrons and muons (binned in lepton p_T) for the CR (blue) and SR (red). Figure 5.18 shows the same plots without any binning applied. The relative differences between the efficiency-values (in percent) are shown on the ratio plots below. The differences between the CR and the SRs lies between 5 and 35%, but depend on the lepton flavour (electron/muon) the p_T of the leptons and the SR. As the p_T-binned values have typically large statistical uncertainties for themselves, it was decided to use the inclusive (non p_T-binned) values to finally quantify an uncertainty. As it is shown in figure 5.18, the inclusive values imply an uncertainty of around

25% (electrons) and 30% (muons) which has to be applied to the nominal fake efficiencies measured in data to account for CR/SR differences.

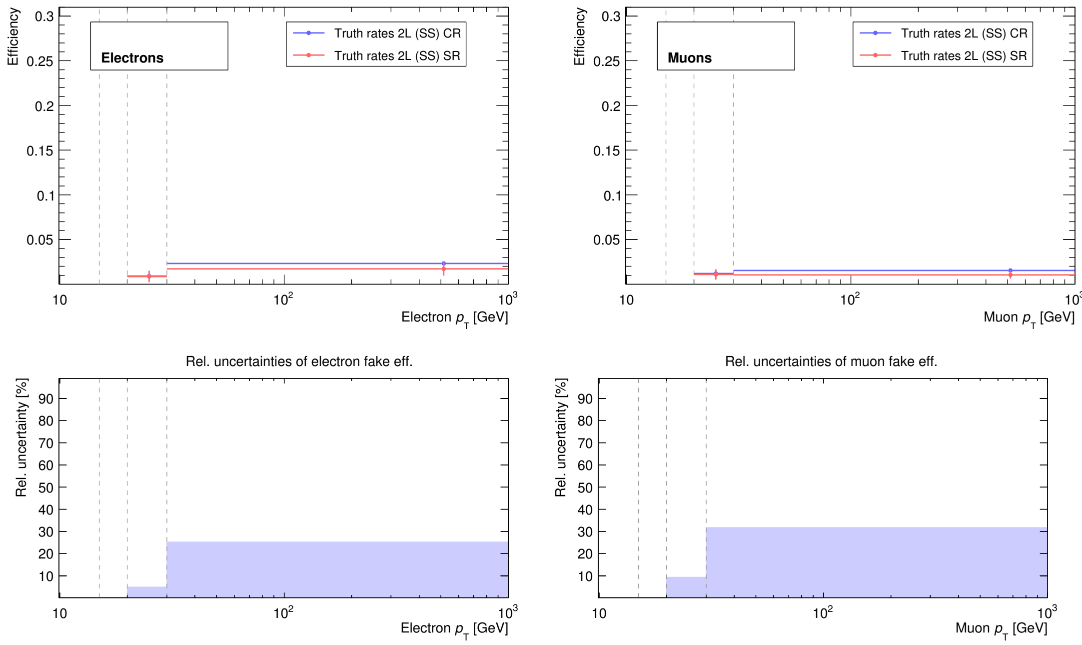

Figure 5.17: Truth-level fake efficiencies (binned in lepton p_T) for electrons (left) and muons (right) derived in the CR (blue) and the 2LSS SR (red). The ratio plots at the bottom show the relative differences between the efficiency-values in percent.

5.2.3 Comparison of Non-prompt lepton estimation from Template Fit Method and Matrix Method

The estimated contributions of fake/non-prompt leptons in the CR(μ_{HF}) and CR(el_{HF}), as well as in the SR given by the (nominal) Template Fit Method can be compared to the alternative estimations given by the Matrix Method (section 5.2.2). This comparison is shown in table 5.8. A good agreement is found in CR(μ_{HF}) between the estimation provided by the two methods while a small tension is observed in CR(el_{HF}) where the TFM provides a smaller estimate than the MM. The uncertainties of the estimates include both, statistical and systematic uncertainties (section 5.2.2 for more details on the MM uncertainties). Within their uncertainties both methods deliver compatible results, with the uncertainties of the MM predictions being slightly larger than those from the TFM.

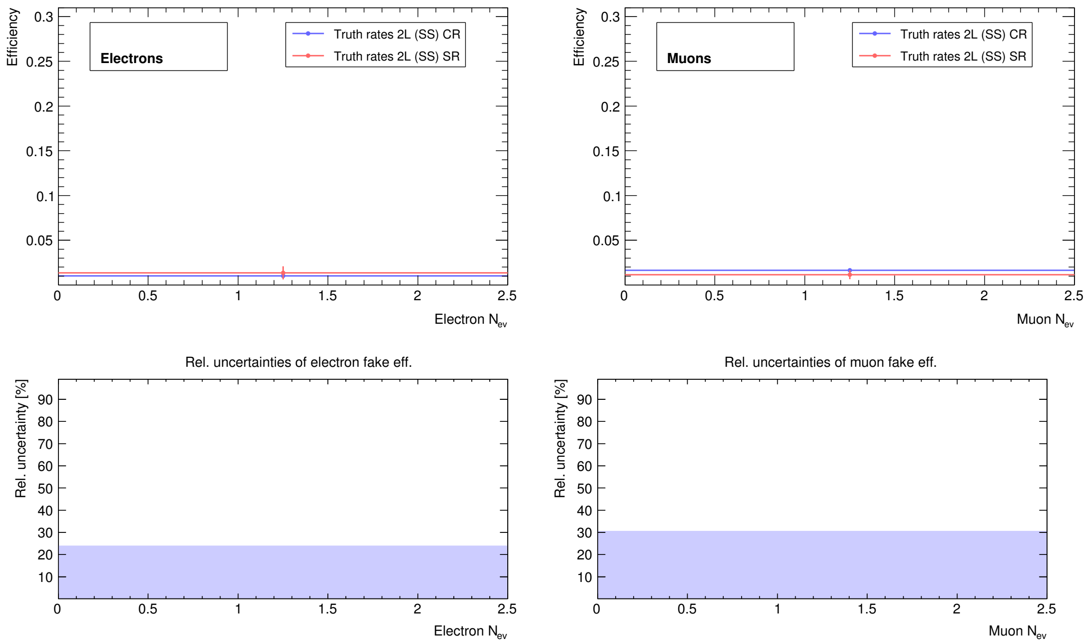

Figure 5.18: Truth-level fake efficiencies (inclusive) for electrons (left) and muons (right) derived in the CR (blue) and the 2LSS SR (red). The ratio plots at the bottom show the relative differences between the efficiency-values in percent.

	CR(μ_{HF})	CR(el_{HF})	SR
μ_{HF}	67 ± 18	21 ± 6	8.0 ± 3.1
el_{HF}	0 ± 0	90 ± 50	3.0 ± 2.1
el_{Co}	0 ± 0	106 ± 28	3.4 ± 1.7
Fakes (other)	14 ± 11	39 ± 25	1.9 ± 1.7
TFM Fake leptons	81.0 ± 21.1	256.0 ± 65.9	16.3 ± 4.4
MM Fake leptons	96.4 ± 28.9	380 ± 95	24.6 ± 7.3
MC Fake leptons	78 ± 13.4	225.7 ± 30.1	14.7 ± 3.6

Table 5.8: Comparison of fake lepton estimates with the MM and TFM methods in CR(μ_{HF}) and CR(el_{HF}), as well as in the SR. The uncertainties of the estimates include statistics, as well as systematic uncertainties. The two methods are also compared with the prediction provided by the MC.

5.3 Charge mis-identified (QMisID) leptons estimation

Charge-flip events are present in the 2LSS channel and originate mainly from the ttbar process. There are two different ways by which these charge flip events contaminate ee and $e\mu$ regions:

- hard bremsstrahlung plus asymmetric conversion ($e^{\pm} \to e^{\pm}\gamma^{*} \to e^{\pm}e^{+}e^{-}$);
- mis-measurement of the electron track-curvature.

For the p_T range relevant to this analysis muon charge-flip is negligible. The dedicated ECIDS tool is used which leads to an improved rejection of electrons with mis-identified electrical charge. Table 5.9 shows the impact of using PLIV, ECIDS and ambiguity cuts on leptons in the 2LSS pre-selection region defined by requiring $N_{\text{jet}} \geq 1$ and $N_{bjet} \geq 1$.

	Change in signal (tHq)		Background reduction
PLV to PLIV	9.8	10.3	Hadron decay 10%
ECIDS	10.3	10.1	Charge flip 40%
Ambiguity flag	10.1	9.9	Charge flip 8%, γ conversion 2%

Table 5.9: The tight lepton working points and their effect on signal and backgrounds.

The charge flip events remaining after applying ECIDS cuts are estimated by a data-driven method. This approach relies on measuring the probability that an electron can have its charge wrongly assigned. These rates are measured using a data sample selecting Z events where $Z \to e^{+}e^{-}$ ($e^{+}e^{+}, e^{-}e^{-}$ in case of charge flip). A likelihood-based method is used to obtain the charge-flip rates.

5.3.1 QMisID background estimation strategy

Final states with a true opposite-sign lepton pair e.g. ($t\bar{t} \to b\bar{b}W^{+}W^{-} \to b\bar{b}e^{+}e^{-}\nu\bar{\nu}$) can be reconstructed in three possible ways:

- $e^{+}e^{-} + X$ without any charge mis-identification, with probability $(1-\epsilon)^2$;
- $e^{+}e^{-} + X$ with two electrons having charge flip, with a probability of ϵ^2;

- $e^{\pm}e^{\pm}$ when only one of the two electrons is mis-identified, with a probability of $2\epsilon(1-\epsilon)$.

ϵ is the rate of `QMisID` for a single electron. For N true opposite-sign events, the number of reconstructed events will be:

$$\begin{aligned} N_{OS} &= (1-2\epsilon+2\epsilon^2)N \\ N_{SS} &= 2\epsilon(1-\epsilon)N \end{aligned} \tag{5.11}$$

In this way, by knowing the `QMisID` rate ϵ, the estimated number of same-sign events N_{SS} can be computed from the measured number of opposite-sign events N_{OS}. For the ee, where ϵ_i and ϵ_j are the `QMisID` rates for each of the two electrons:

$$N_{SS} = \frac{\epsilon_i+\epsilon_j-2\epsilon_i\epsilon_j}{1-\epsilon_i-\epsilon_j+2\epsilon_i\epsilon_j} N_{OS} \tag{5.12}$$

and for $e\mu$ channels:

$$N_{SS} = \frac{\epsilon}{1-\epsilon} N_{OS} \tag{5.13}$$

5.3.2 QMisID rates estimating with the likelihood method

Electrons from the leptonic decay of the Z boson ($Z \to ee$) are used to measure the charge mis-identification. These rates are derived from the data events in the m_{ee} region around the reconstructed Z-boson peak. The expected number of same-sign events $\bar{N}^{ij}_{SS}$ with electron pairs falling in the bin combination i, j can be written as a function of the number of events N^{ij} as follows:

$$\bar{N}^{ij}_{SS} = N^{ij}(\epsilon_i+\epsilon_j-2\epsilon_i\epsilon_j) \tag{5.14}$$

If all the same-sign events in the Z peak are products of electron charge mis-identification, then N^{ij}_{SS} is described by a Poisson distribution:

$$f(N^{ij}_{SS}|\bar{N}_{SS}(\epsilon_i\epsilon_j)) = \frac{[\bar{N}^{ij}_{SS}]^{N^{ij}_{SS}} e^{-\bar{N}^{ij}_{SS}}}{N^{ij}_{SS}!} \tag{5.15}$$

which is integrated into a likelihood:

$$L(\vec{\epsilon})|N_{SS} = \prod_{i,j} f(N^{ij}_{SS}|\bar{N}_{SS}(\epsilon_i\epsilon_j)) \tag{5.16}$$

that can be maximised (minimisation of $-2\ln L$) to obtain the rates that best describe the data.

Table 5.10: Binning scheme for the calculation of the QMisID rates.

η bin	0	1	2	3
$\|\eta\|$ range	[0, 1.37]	[1.37, 1.52]	[1.52, 2.0]	[2.0, 2.5]
p_T bin	0	1	2	
p_T range	[20, 90]	[90, 130]	[130, 1000]	

5.3.3 $|\eta|$ and p_T binning

The QMisID rates derived from the data with the likelihood method for tight electron definitions and parametrised as a function of $|\eta|$ and p_T. The binning must be optimised to best describe the dependence of the rates. Different η and p_T binning combinations are studied for QMisID rates starting form finner bin selection to the inclusive binning as in figure 5.19. The estimated number of same-sign events (QMisID x OS) remains almost the same for QMisID derived with different η and p_T binning combinations but we observed large uncertainty evaluated form MIGRAD [114] on QMisID rates derived with small η and p_T binning combinations. On the other hand, for QMisID rates derived with more inclusive η and p_T bins, the shape agreement for different variables is degraded.

Therefore, four different regions have been identified in η and three in p_T. These regions have been used to define the η and p_T binning shown in table 5.10. The rates are presented as a function of $|\eta|$ and parametrised in p_T can be shown in figure 5.20. As a function of $|\eta|$ the rates are related to the material distribution of the pixel in the inner detector. In the central region of the detector where the material budget is smaller, the rates are also smaller. The track resolution also has the best performance in this region. Moving to the outer part of the inner detector (higher $|\eta|$ values), the amount of material the electrons transverse through increases which result in increase the number of trident electrons, and therefore the mis-measurement of the charge. The QMisID rate increases with electron p_T, since at high p_T a slightly curved track can induce a charge-measurement error.

5.3.4 Uncertainties on QMisID rates

Three sources of systematic uncertainties have been taken into account in the QMisID rates. The final uncertainty on the rates is the quadratic sum of these contributions:

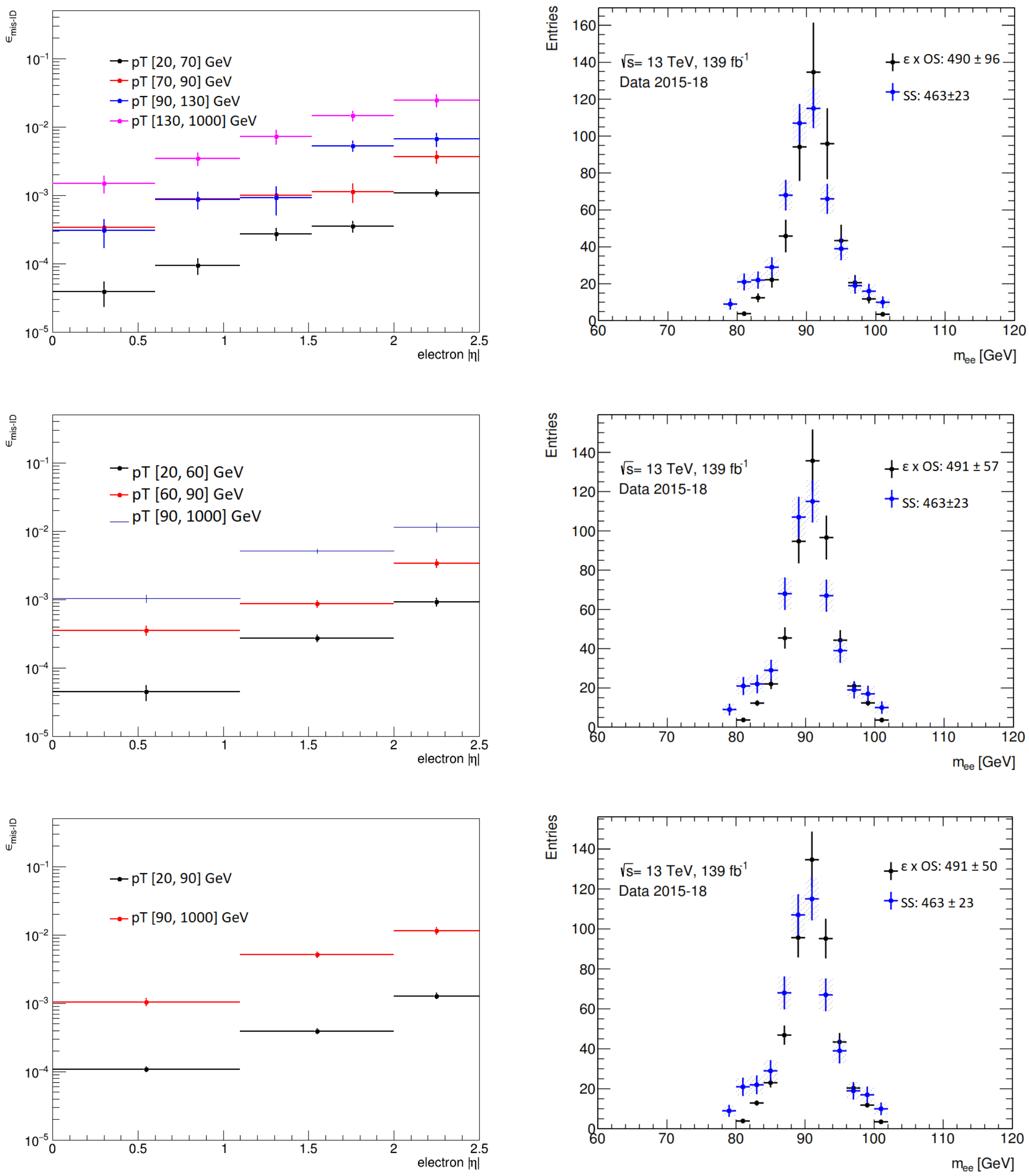

Figure 5.19: Left: The `QMisID` rates derived with different η and p_T binning combinations. Right: The data closure performed with `QMisID` rates using the cross-ponding η and p_T binning combinations.

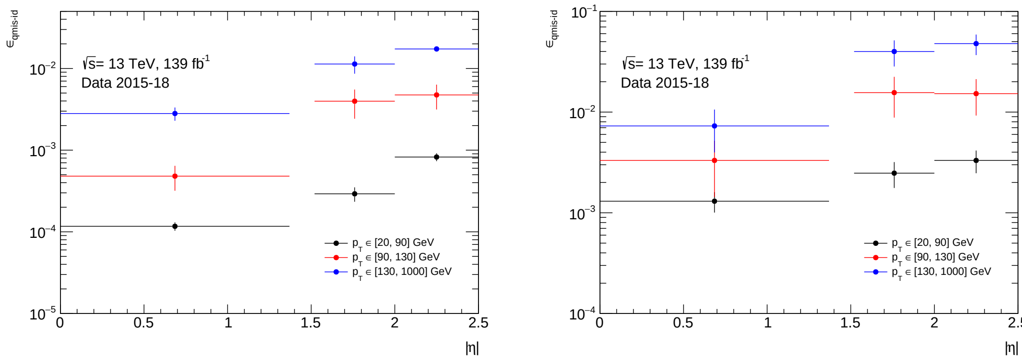

Figure 5.20: Electron `QMisID` rates derived from the data with the likelihood method. The rates are presented as a function of $|\eta|$ and parametrised in p_T. (a) `QMisID` rates computed with the ambiguity flag applied, used to estimate `QMisID` background in all 2LSS region except CR(elConv) (b) `QMisID` rates computed with the inverted ambiguity flag, used to estimate `QMisID` background in CR(elConv)

- Uncertainty from the likelihood method which depend on the statistical size of the control region of the data in which the rates are estimated.
- The variation of the rates due to the variation of the m_Z window, detailed explanation in section 5.3.5.
- The difference between `QMisID` rates derived from likelihood method to the rates based on the MC truth information with simulated $Z \to e^+e^- +$ jets events, more detail explanation in section 5.3.6.

5.3.5 The variation of the rates due to Z window

The likelihood method uses only Z signal events in the m_Z window. Therefore, background coming from other processes (e.g. fake electrons) where the di-lepton invariant mass corresponds to the one of the Z boson needs to be subtracted. This background can be estimated from the side-bands of the Z-mass window. In this side-band method we divide invariant mass of Z boson in three regions, A, B and C. The central region B corresponds to the Z peak. The upper A and lower C sidebands are defined with widths equal to the m_Z window so that we can obtain the background from the average yield, the number of events in the A region, n_A and the number of events in the C region n_C, and remove this from total number of events in the peak region B, n_B. This way Z signal events:

$$N_Z = n_B - \frac{n_A + n_C}{2} \tag{5.17}$$

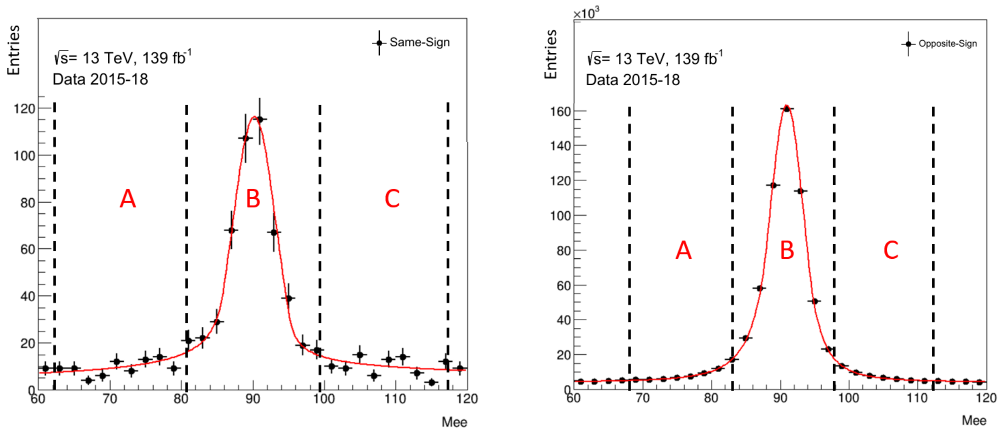

Figure 5.21: Comparison of the invariant mass m_{ee} between (a) same-sign and (b) opposite-sign data events around the Z-peak for tight selection. The peak for same-sign electrons is shifted with respect to opposite-sign electrons.

The likelihood method uses measured same-sign and opposite-sign Z signal events in order to compute the `QMisID` rates. No selection other then inverting the sign requirement for opposite-sign is used. For same-sign electrons the Z-peak is shifted to lower values with respect to opposite-sign electrons (Figure 5.21). That may introduce in some mis-measurement of the rates. Therefore, regions used by the side-band method are defined separately in the same-sign and opposite-sign distributions. These regions are determined by the fit results using the mean value k and the standard deviation σ. The Z-signal region B is defined as $k \pm 3\sigma$, where the regions A and C are defined so that they have the same width as the central region, i.e. 6σ. The variation of the rates due to the variation of the Z-peak region by 1σ, as shown in figure 5.22, is taken into account as a systematic uncertainty.

5.3.6 Validation of the likelihood method

The likelihood method is used as a baseline to compute the `QMisID` rates which needs to be validated. This validation is performed by comparing the `QMisID` rates derived from likelihood method to the rates based on the MC truth information (truth-matching) methods. The simulated $Z \to e^+e^- + \text{jets}$ events

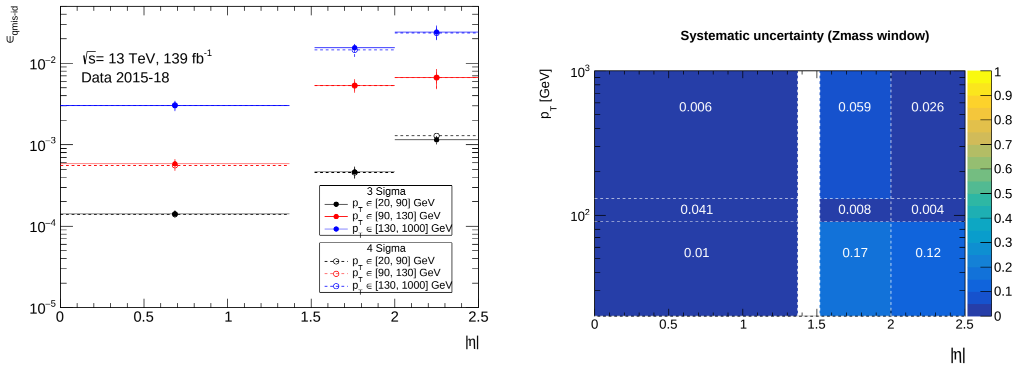

Figure 5.22: (a) Electron QMisID rates derived from the data with the likelihood method for different m_Z window (b) Ralitive uncertainty on rates due to variation of m_Z window by 1 σ: ($|\epsilon_{4\sigma} - \epsilon_{3\sigma}|/\epsilon_{3\sigma}$)

are used for the validation. The comparison is shown in figure 5.23, as a function of $|\eta|$ and parametrised in p_T. There is no significant disagreement between both of the approaches. Differences between the rates extracted from both methods are considered as a source of systematic uncertainty.

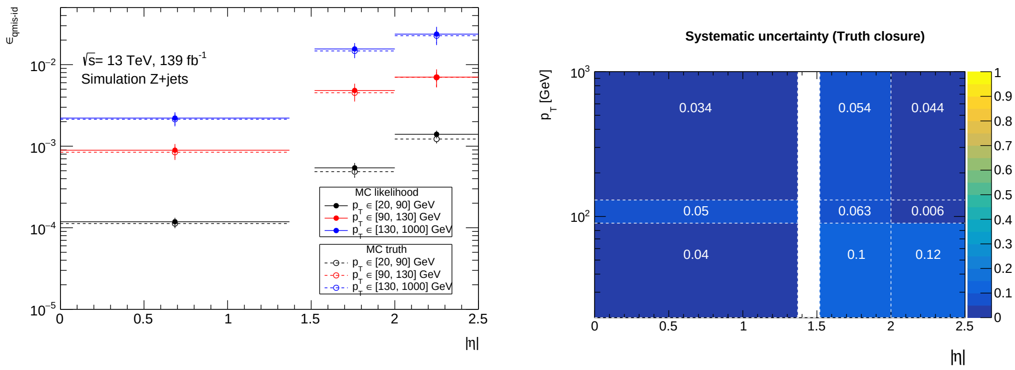

Figure 5.23: (a) Comparing MC QMisID rates derived from likelihood method to the rates based on the MC truth information (b) Relative uncertainty ($|\epsilon_{MCtruth} - \epsilon_{Likelihood}|/\epsilon_{Likelihood}$)

5.3.7 QMisID event yield

The event yields with charge-flip electrons are obtained by weighting the opposite sign event with QMisID weights ($W_{\texttt{QMisID}}$). The opposite sign events are obtained by the same 2LSS pre-selection (just inverting the sign requirement). Table 5.11 shows charge-flip electron event yield predictions in the 2LSS preselection region split in flavour compositions. Figure 5.24 compares the invariant mass distribution for (a) MC predictions and the (b) data-driven estimates of charge-flip electron. A fair agreement between the Monte Carlo and data-driven predictions is observed. The comparison is also shown in figure 5.25 for fake CRs used in 2LSS channel.

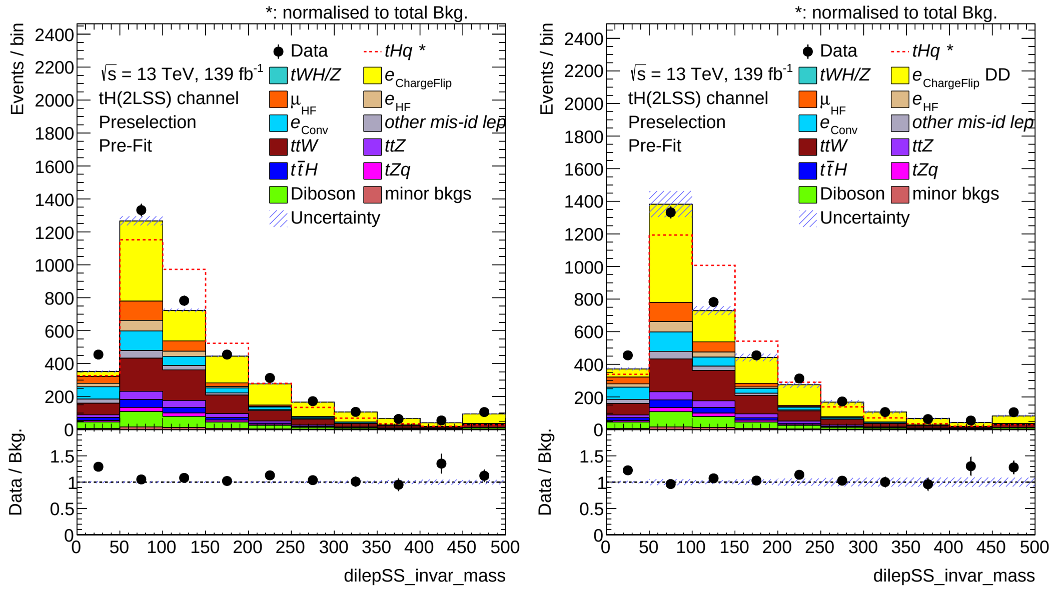

Figure 5.24: Invariant mass distribution for (a) MC predictions and the (b) data-driven estimates of charge-flip electrons.

Predictions	Pre-selection	ee	$e\mu$
Monte Carlo (MC)	1260 ± 27	801 ± 26	461 ± 8
Data-driven (DD)	1380 ± 190	920 ± 120	460 ± 70
MC/DD	0.91	0.87	1.00

Table 5.11: Data-driven charge-flip electron event yields in the pre-selection region, which is further split according to the lepton flavour composition. As a comparison, MC predictions and the ratio between data-driven estimates and MC predictions are given.

5.3.8 Closure test

The closure test is performed by comparing the estimated number of same-sign ee events to the measured number of same-sign events. The estimated number

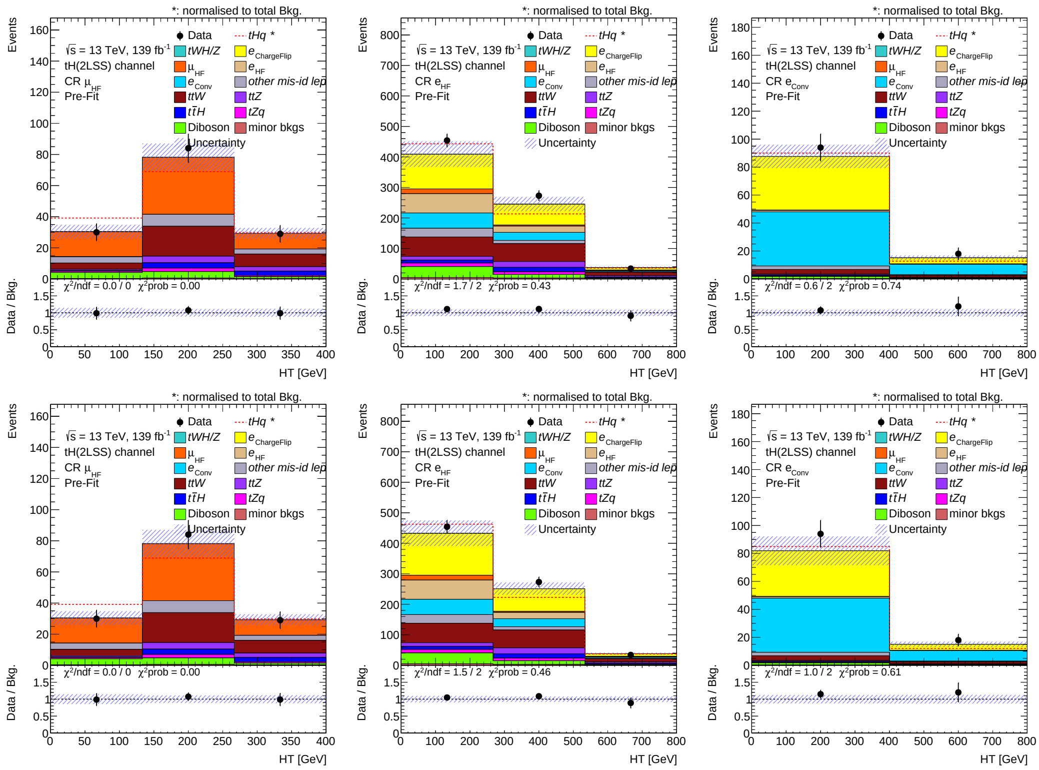

Figure 5.25: Pre-fit plots of the CRs used in the 2LSS channel, comparing the first row with MC `QMisID` to the bottom row with DD `QMisID` .

are obtained by using the QMisID weights '$W_{\texttt{QMisID}}$' on opposite-sign events. Figure 5.26 (a) shows a comparison between the expected distribution of m_{ee} in the data with the observation (the latter also contains contributions from non-prompt electrons). After subtracting the non-prompt electron background using the sidebands, the measured number of same-sign events in the m_Z window is found to be 463, while the expectation from the likelihood method is 491 $\pm$ 57. The closure test is also performed using simulated $Z \rightarrow e^+e^- +$ jets as shown in figure 5.26 (b). For MC closure the measured number of SS events founds to be 404$\pm$27 while the expectation by using the $W_{\texttt{QMisID}}$ on opposite-sign events is 417$\pm$57.

5.4 ttW background studies

The ttW irreducible background contributes 17% to the SR predicted yields. The nominal prediction used is $aMC@NLO+Pythia8$.. The prediction provided by the available simulation was found not be in agreement with data in previous

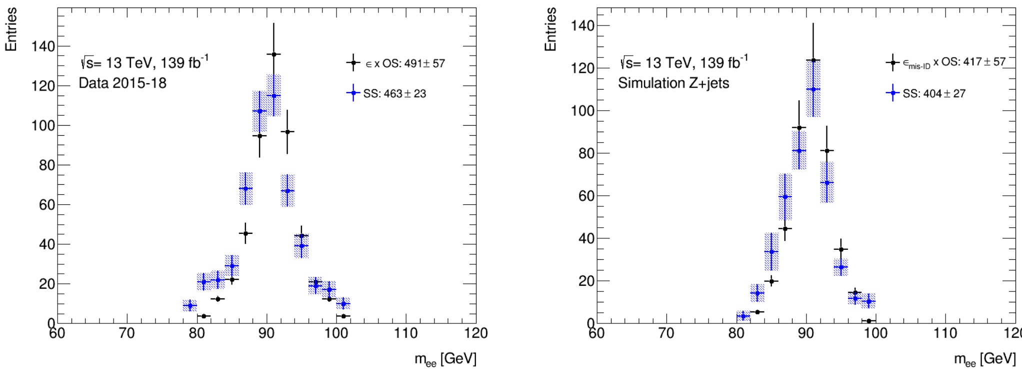

Figure 5.26: The closure test performed using Data (a), and MC (b), comparing the measured number of same-sign events to the re-weighted opposite-sign events.

measurements, such as Ref. [115]. A similar observation is found in this analysis in the regions enriched with ttW events. For this reason an in-suit estimation is performed where a normalisation factor for ttW is derived from data. The distribution of the number of jets and b-tagged jets in the CR(ttW) is shown in figure 5.27. In CR(ttW) a disagreement between data and prediction is observed in both the multiplicity of jets and the distribution of number of b-tagged jets.

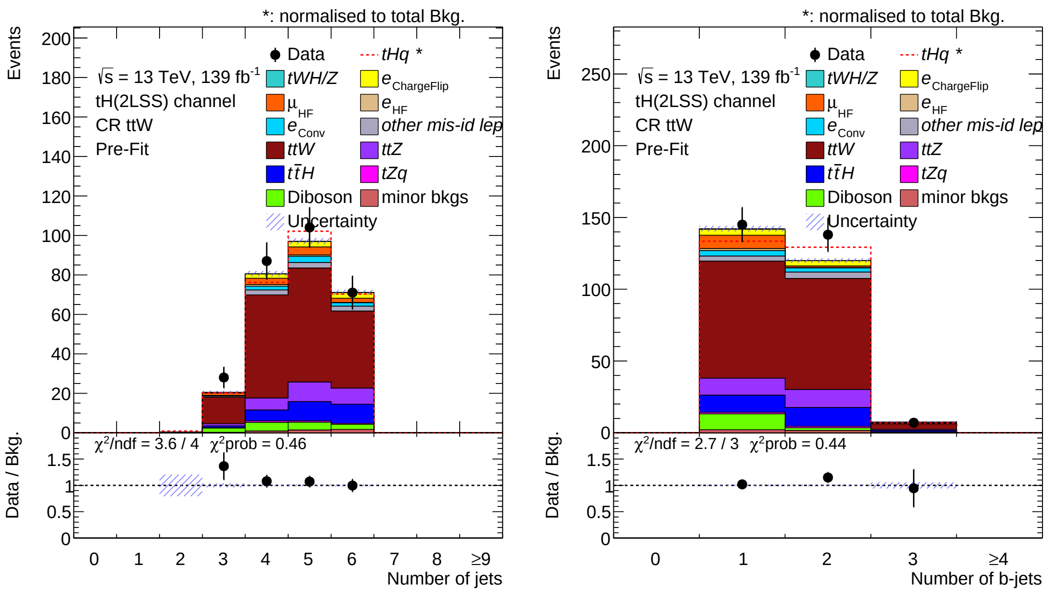

Figure 5.27: Distribution of number of jets and number of b-tagged jets for data and prediction in the CR(ttW). The uncertainty is statistical only. The ttW prediction is derived using $aMC@NLO + Pythia8$.

5.4.1 Comparison of the $aMC@NLO + Pythia8$ and $Sherpa2.2.10$ predictions

The prediction given by the nominal $aMC@NLO + Pythia8$ simulation and the $Sherpa2.2.10$ simulation for the the ttW multiplicity of the jets and b-tagged jets and H_T is shown in figure 5.28. In CR(ttW) the $Sherpa2.2.10$ simulation predicts 6% fewer events than $aMC@NLO + Pythia8$.

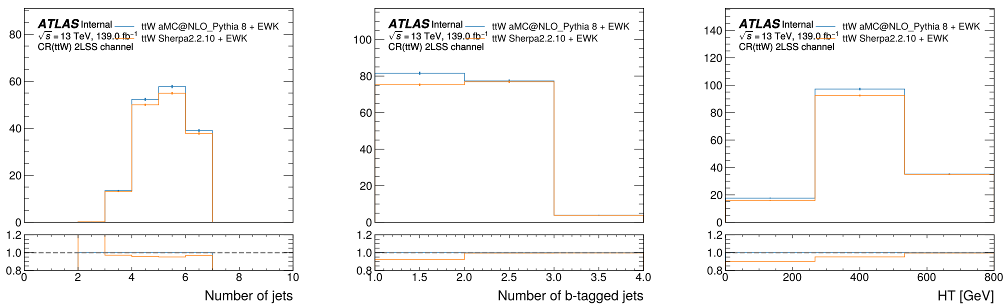

Figure 5.28: Distribution of number of jets, number of b-tagged jets and H_T in the CR(ttW). Comparison of $aMC@NLO+Pythia8$ (blue) and the $SHERPA2.2.10$ (orange) simulations. The uncertainty is statistical only.

The distribution of the number of jets and b-tagged jets in the CR(ttW) is shown in figure 5.29. Here the data and total prediction are compared, where the ttW prediction is derived using the $Sherpa2.2.10 + EWK$ simulation. No significant difference between the data-to-simulation modelling is observed with respect to figure 5.27. Finally, the BDT(tHq) distribution for the two ttW predictions in the 2LSS SRs is shown in figure 5.30.

5.4.2 Statistical fit on $aMC@NLO + Pythia8$ and $Sherpa2.2.10$ predictions

A statistical only fit is run over the CRs data to compare the ttW correction factor derived using the $aMC@NLO+Pythia8$ and $Sherpa2.2.10$ prediction. All the CRs are included in the fit and the $k(ttW)$ together with the mis-identified leptons correction factors are estimate from data. The fit results are shown in figure 5.31. The normalisation factors derived are compatible within their uncertainties for the $aMC@NLO + Pythia8$ and $Sherpa2.2.10$ cases.

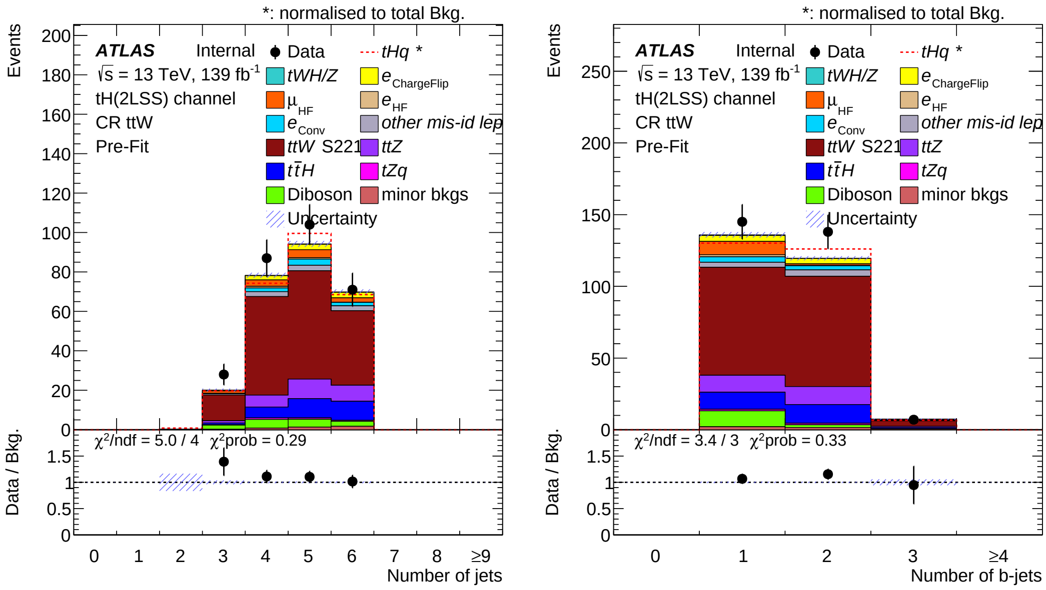

Figure 5.29: Distribution of number of jets and number of b-tagged jets for data and prediction in the CR(ttW). The uncertainty is statistical only. The ttW prediction is derived using $aMC@NLO + Pythia8$.

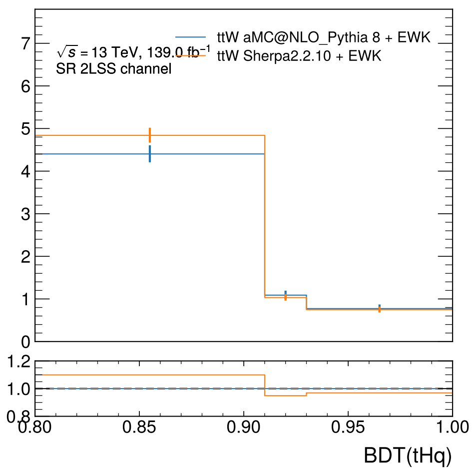

Figure 5.30: BDT(tHq) distribution in SR.The uncertainty is statistical only. The ttW prediction from $aMC@NLO + Pythia8$ and $Sherpa2.2.10$ are compared.

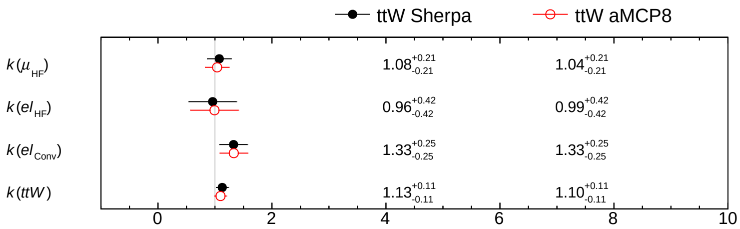

Figure 5.31: Normalisation factors derived from statistical only fit in the CRs data. The results derived using *aMC@NLO* + *Pythia*8 (red) and the *Sherpa*2.2.10 (black) for the ttW prediction are compared.

Chapter 6 Uncertainties and Statistical analysis

A profile likelihood fit is used in this analysis to extract the signal strength from the data. Various studies are performed to validate the input distributions and the performance of the fit. This chapter opens with discussion on sets of uncertainties which are related to the analysis mainly experimental systematics, signal and background modelling theoretical systematics. Then a theoretical description of the profile likelihood fit method. Some of the studies performed to test the nominal model of the signal and the background, are presented. Finally, results of a fit to the data are shown and compared to expectations.

6.1 Experimental and theoretical uncertainties

The signal and background predictions in both signal and control regions are affected by a number of different sources of uncertainty. These are related to the reconstruction of physics objects in the detector, the techniques used to determine the expected size of the backgrounds and modelling of the signal and background process. Experimental (detector-related) uncertainties can arise from the reconstruction of physics objects in the detector. These uncertainties are applied as recommended by the different CP groups. Modelling uncertainties are evaluated in three ways: comparing the nominal prediction to an alternative prediction; varying the internal parameters of the nominal simulation; or varying the predicted cross-section within the theoretical uncertainty. All systematic uncertainties are summarized in table 6.1, which lists the main systematic categories and the number of their components. Furthermore, whether the systematic uncertainty affects only the normalization or also the shape is specified.

The systematic variations included are: the theoretical uncertainties on the cross-sections of the background processes, the modelling uncertainties of the main background processes ($t\bar{t}$, ttW and ttH), the variations of the flavour tagging performance, the pile-up variation, the JVT efficiency variation, the muon and electron isolation and identification uncertainties the jet energy scale and resolution uncertainties and the luminosity uncertainty. Finally, the uncertainty from the data-driven estimation of the charge flip electron background is included.

Systematic uncertainty	Type	Comp.
Experimental uncertainties		
Luminosity	N	1
Pileup modeling	SN	1
Physics Objects		
Electrons	SN	7
Muons	SN	15
Jet energy scale	SN	30
Jet energy resolution	SN	13
Jet vertex tagger	SN	1
Forward Jet vertex tagger efficiency	SN	1
$E_{\mathrm{T}}^{\mathrm{miss}}$	SN	3
b-tagging		
Efficiency	SN	45
Mis-tag rate (c)	SN	20
Mis-tag rate (light)	SN	20
Signal and background modeling		
Signal		
tH cross-section	N	2
tH modeling	SN	4
Background		
$t\bar{t}$ modelling	SN	6
$t\bar{t}H$ modelling	SN	6
$t\bar{t}H$ cross-section	N	2
Single top modelling	SN	15
ttW and ttZ modelling	SN	2
ttW and ttZ cross-section	N	4
Other Backgrounds		
cross-section	N	18
Template fit uncertainties	SN	1
Electron charge misassignment	SN	1

Table 6.1: List of systematic uncertainties included in the analysis. An 'N' means that the uncertainty is taken as normalisation-only for all processes and channels affected, whereas 'SN' means that the uncertainty is taken on both the shapes and the normalisation. Some of the systematic uncertainties are split into several components for a more accurate treatment: the number of such components is indicated in the column labeled as 'Comp.'

6.2 Statistical analysis

The analysis's objective is to quantify the tHq process. This is accomplished by taking the signal strength—defined as the ratio between the observed cross-section: $\mu(tHq) = \sigma(tHq)^{obs}/\sigma(tHq)^{SM}$ and the SM prediction—and extracting it from the data. The tHq signal strength is extracted by means of binned profile likelihood fits performed using the TRExFitter [24] package. All the regions defined as in section 5.1 are included in the fit. Together with the POI $\mu(tHq)$ four normalisation factors are derived from the fit on data for the main backgrounds: three for the mis-identified leptons background, as described in section 5.2.1, $k(\mu_{HF})$, $k(el_{HF})$, $k(el_{Co})$, and one for the irreducible background ttW. Systematic uncertainties are included in the fit in the form of Gaussian nuisance parameters (NPs). The sections that follow provide an introduction to the main ideas behind the parameter estimation approach.

6.2.1 Likelihood function

Any type of data analysis involves the use of a data set or sample x of observed attributes, which one attempts to relate to some theoretical quantities $\vec{\theta}$ (usually parameters of a model). For specific values of its parameters $P(x|\vec{\theta})$, scientific models must provide a probability to witness some data. This probability is then expressed as a likelihood function for the specified observed data x^{obs}:

$$L(\vec{\theta}) = P(x^{obs}|\vec{\theta}) \tag{6.1}$$

One can estimate a parameter by using the likelihood. It can be demonstrated that the resulting values of the parameters $\hat{\vec{\theta}}$ are good approximations of their true values $\vec{\theta}^{true}$ [116] after finding its global maximum over all parameters. Although there may be bias in the estimated parameters, this bias vanishes in the large sample limit. The Maximum Likelihood method is the name given to this parameter estimate technique. Being invariant under a variable transformation is one of its characteristics. As a result of searching for the function's extreme, the derivation at that point over all parameters produces zero:

$$\frac{\partial L(\vec{\theta})}{\partial \vec{\theta}}|_{\hat{\vec{\theta}}} = 0 \tag{6.2}$$

The estimator $\hat{\vec{\theta}}$ from equation 6.2 cannot typically be expressed directly, thus computational methods are employed to scan the parameter phase space and identify the maximum value of the likelihood. In actual applications, a log-likelihood (or log-likelihood, LL) is utilized in its place. Given that the logarithm is a monotonic function, it has no impact on parameter estimation, and equation 6.2 still holds if the likelihood is changed to the log-likelihood.

6.2.2 Variance of the parameter estimator

Without understanding of an estimator's uncertainty, its value is useless. There are various methods for figuring it out. One method relies on the likelihood's second derivative, which yields an estimator of variance V_{ij} [117], where θ_i and θ_j are two parameters:

$$\hat{V_{ij}} = 1/(-\frac{\partial^2 \log L}{\partial \theta_i \theta_j})|_{\hat{\theta}_i \hat{\theta}_j} \tag{6.3}$$

$$\Delta\hat{\theta}_i = \sqrt{\hat{V}_{ii}} = 1/\sqrt{-\frac{\partial^2 \log L}{\partial\theta_i^2})}|_{\hat{\theta}_i} \tag{6.4}$$

This can be used to calculate the uncertainty of a parameter θ_i as in equation 6.4. This method uses a quadratic approximation in the maximum of the log-likelihood and only involves computing the second derivative at one point, but it produces strictly symmetrical uncertainty. Only in the large sample limit does this approximation hold exactly, and neither generally does for a small number of events. A graphical method as shown in figure 6.1 is a more accurate way to estimate the error and can provide distinct values for the upper $\Delta\hat{\theta}_i^{up}$ and lower $\Delta\hat{\theta}_i^{down}$ uncertainty using the following relation.

$$\log L(\hat{\theta}_i + \Delta\hat{\theta}_i^{up}) = \log L(\hat{\theta}_i + \Delta\hat{\theta}_i^{down}) = \log L(\hat{\theta}) - 1/2 \tag{6.5}$$

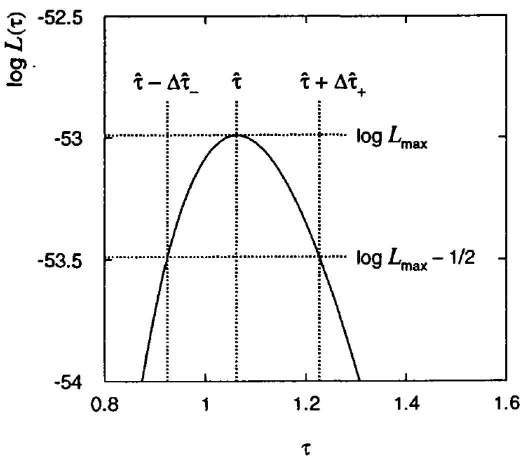

Figure 6.1: The log-likelihood as function of its parameter [116]

6.2.3 Binned maximum likelihood

The measured data are frequently analyzed using histograms, which are binned distributions. Each bin i has a specific number of data events n_i, and the theoretical prediction provides a mean number of events in each bin $v_i(\vec{\theta})$, which again depends on some fundamental model parameters $\vec{\theta}$. As a result, the data in each bin have a Poisson distribution $P_{Poisson}(n, v_i)$, and multiplying the probabilities in each bin yields the overall probability of observing the given data. This results in the following log-likelihood:

$$\log L(\vec{\theta}) \propto \sum_{i}^{N_{bins}} [-v_i(\vec{\theta}) + n_i \log v_i(\vec{\theta}) + ...] \tag{6.6}$$

where N_{bins} is the distribution's bin count, and the terms that don't depend on $\vec{\theta}$ are eliminated. As the likelihood's absolute value holds no information and only the derivation or relative difference with respect to the maximum has to be known, this is done to make the computation simpler.

6.2.4 Parameter of interest and profile likelihood

In this analysis, there are several parameters, the signal strength μ_{tHq} is the most essential parameter in the tHq model since it determines the amount of measured signal. Typically, this parameter is known as an interest parameter (POI). Due to the fact that the remaining parameters' values are not always significant, they are referred to as nuisance parameters (NPs). The value of the POI is determined using the maximum likelihood method. However, because the POI interferes with other factors, it cannot be directly utilized to make conclusive assertions about, for example, the significance or the limits of the measurement. Through profiling, which eliminates the dependence on the nuisance parameters in the large sample limit, this dependence on the other factors can be reduced to a minimum.

The likelihood is initially specified as $L(\mu, \vec{\theta})$, where $\vec{\theta}$ and μ denotes the NPs and the POI respectively. The following definition applies to the profile likelihood [118], which is solely dependent on the parameter of interest.

$$L_P(\mu) = L(\mu, \hat{\hat{\theta}}(\mu)); \frac{\partial L(\mu, \vec{\theta})}{\partial \vec{\theta}}|_{\hat{\hat{\theta}}(\mu)} = 0 \tag{6.7}$$

Through the calculation of POI $\mu(tHq)$, we are unable to obtain information on the degree of agreement between the data and the background-only or signal-plus-background hypothesis. As a result, the analysis's hypothesis testing [117] is based on the profiled likelihood ratio $\lambda(\mu)$, which is defined as

$$\lambda(\mu) = \begin{cases} \frac{L(\mu,\hat{\hat{\theta}}(\mu))}{L(\hat{\mu},\hat{\theta}(\mu))}, & \hat{\mu} \geq 0; \\ \frac{L(\mu,\hat{\hat{\theta}}(\mu))}{L(0,\hat{\theta}(0))}, & \hat{\mu} < 0 \end{cases} \tag{6.8}$$

The denominator is the unconditionally maximized likelihood when $\mu \geq 0$, and the numerator maximizes the likelihood for a particular value of μ. The

$\mu < 0$ is refer to avoiding complications in the computations in the case of deficit of signal-like events. Depending on the tested hypothesis, different test statistics t_μ are defined to test a particular of μ. The test statistics for the observed data is referred to as t_μ^{obs}. The probability of an outcome that is equal to or more extreme than the observed is known as the p-value for a given observation, under a specific hypothesis:

$$p_\mu = \int_{t_\mu^{obs}}^{\infty} f(t_\mu|\mu, \hat{\hat{\theta}}(\mu))dt_\mu \tag{6.9}$$

where $f(t_\mu|\mu, \hat{\hat{\theta}}(\mu))$ is the sampling distribution of the test statistics. Small $p-$ values provide evidence against the test hypothesis, and they are frequently translated into the normal significance Z value. In case of any excess in data, the test statistics q_0 is defined as follows:

$$q_0 = \begin{cases} -2\ln\lambda(0), & \hat{\mu} > 0; \\ 0, & \hat{\mu} \leq 0 \end{cases} \tag{6.10}$$

To determine whether the data are consistent with the background only hypothesis $\mu = 0$:

$$p_0 = \int_{q_0^{obs}}^{\infty} f(q_0|0, \hat{\hat{\theta}}(0))dq_0 \tag{6.11}$$

where p_0 is the probability that a test statistic equal to or greater than the observed results from the background-only (or in the absence of a signal) hypothesis. In the ATLAS experiment, discovery is declared if the background only hypothesis is rejected at the 5σ level, which corresponds to a probability of a false positive of approximately 3×10^{-7}.

For purposes of establishing an upper limit on the single strength μ, a test statistics q_μ is used.

$$q_\mu = \begin{cases} -2\ln\lambda(\mu), & \hat{\mu} \geq \mu; \\ 0, & \hat{\mu} < \mu \end{cases} \tag{6.12}$$

The Confidence Level of signal CL_s is employed to set these limits.

$$p_\mu = \int_{q_\mu^{obs}}^{\infty} f(q_\mu|\mu, \hat{\hat{\theta}}(\mu))dq_\mu, p_b = \int_{\infty}^{q_0^{obs}} f(q_0|0, \hat{\hat{\theta}}(0))dq_0 \tag{6.13}$$

The 95% CL upper limits on μ:

$$CL_s(\mu) = \frac{p_\mu}{1 - p_b} \leq 5\% \tag{6.14}$$

6.2.5 Asimov dataset

An Asimov dataset can be used to calculate the expected significance and other attributes based on the nominal model's prediction: A `pseudodata` reflecting the statistics of the real data that is produced so that all estimators match their true value. Its creation is simple in the case of a histogram-based analysis, such as in the case of this analysis. The predicted distribution is simply taken, and each bin is given an uncertainty based on its yield (corresponding to the Poisson distribution). The likelihood is built similarly to other types of data. The true values for all parameters will then be provided by the profile likelihood fit that is done to such a dataset. Additionally, it offers a rough estimate of the degree to which the data ought to be able to constrain different nuisance parameters.

6.2.6 Implementation of additional uncertainties

The strategy outlined in the preceding sections simply accounts for statistical variations in the data and presumes an accurate forecast. The yield in each bin is actually affected by systematic uncertainty as well. Typically, systematic uncertainties are calculated for every Monte Carlo sample separately. To keep the conversation straightforward, the following assumes that the prediction v represents a single sample and that the uncertainties are calculated relative. The modified predictions for each sample must then be added together in order to generalize to numerous samples.

In this analysis, the source of each uncertainty is assumed to follow a Gaussian distribution. The theoretical prediction v_i is then transformed into a new version v_i^{new} by the systematic variations. For each systematic j, a nuisance parameter α_j is defined, which has a Gaussian distribution with a mean of 0 and a width of 1. This nuisance parameter is used to execute the systematic variations. The predicted value shifts by $v_i(\mu, \vec{\theta})S_i^j\alpha_j$ assuming that S_i^j is the relative magnitude of uncertainty for each bin.

$$v_i^{new}(\mu, \vec{\theta}, \vec{\alpha}) = v_i(\mu, \vec{\theta})(1 + \sum_j^{N_{syst}} S_i^j\alpha_j) \tag{6.15}$$

N_{syst} stands for the overall count of systematic uncertainty (see section 6.1). The likelihood is then extended with additional Gaussian factors, $\propto \exp\,(-\alpha_j^2/2)$

that represent a penalty on the possible values of the α_j. This results in the following expansion of the log-likelihood in equation 6.6:

$$\log L(\mu, \vec{\theta}, \vec{\alpha}) = \sum_{i}^{N_{bins}} [-v_i^{new}(\mu, \vec{\theta}, \vec{\alpha}) + n_i \log(v_i^{new}(\mu, \vec{\theta}, \vec{\alpha}))] - \sum_{j}^{N_{syst}} \alpha_j^2/2 \quad (6.16)$$

where, excluding constants, the last component is just a logarithm of the Gaussian terms. The post-fit value of α_j indicates the amount by which the systematic was pulled or shifted from its initial value. The uncertainty on the α_j value, where 1 is the pre-fit value, gives the information about the the size of the systematic (smaller or larger) after the fit. Typically, the fit either has no impact on the uncertainties or reduces (constricts) them.

6.2.7 Pruning of systematics

Over 200 systematic uncertainties are taken into account in the analysis, as is summarized in section 6.1. Some of these significantly affect the fit's outcome, but the majority have little to no effect. The minimization process would take a long time if all of them were incorporated into the fit. To prevent this, systematics that might have a tiny impact are excluded.

First, the normalization and shape components of systematic variations are separated. The normalization component describes the impact on the yield in a certain area. The shape component is systematically modified, so that it has no impact on the normalization in the specified region. If the difference in normalization with regard to the nominal distribution is less than 0.5%, the former is dropped. Similar to this, a shape of a systematic is eliminated if there isn't a relative difference of more than 1.0% between any bins of the shape component in the provided region.

6.2.8 Goodness of fit

In this analysis, a saturated model is used to evaluate the goodness of fit. The saturated model can fully fit the data since it contains an additional free parameter for each bin in the distribution. The resulting χ^2 probability is considered as a measure of the goodness of fit. The ratio between the likelihood of the nominal model and the saturated model then asymptotically follows a χ^2 distribution [119].

6.2.9 Blinding strategy

A bias, whether conscious or unconscious, could occur from just conducting the nominal fit to the data without eliminating the signal and optimizing the model based on its results. A blinding approach is used to prevent this from happening: bins with a significant predicted signal contribution are excluded from the fit, and the data are not shown in the graphs. To validate the nominal model, this is a necessary intermediary step. In this thesis most of the results prior to the unblinding will be with a 0.33% blinding threshold on the signal over background ratio.

6.2.10 Software implementation

Data from Monte-Carlo simulation are stored in specific files with tree-like structure called ROOT n-tuples. N-tuples are created with the help of ROOT framework that extends classical C++ programming language. If we extend our idea about tree-like structure of an n-tuple, branches correspond to properties called variable or features for classification purposes. Every feature is represented by a histogram that contains values for every event with respect to the feature we are about to examine.

The study makes use of the `TRExFitter` [24] internal ATLAS fitting framework, which creates histograms from the input data and feeds them to the statistical analysis tools. TRExFitter needs data in root n-tuple format and a configuration file for its functionality. The framework is directed by the configuration file. a basic text file in plain syntax **blocks** with blank lines separating them.

- **Job** block defines general options
- **Fit** block specifies details of the fit model
- **Region** block define the distributions taken into account by the fit, also specify variables and cuts.
- **Sample** blocks define the samples considered
- **Systematic** blocks specify systematic uncertainties

The TRExFitter program run within a specialized Docker container. A root n-tuple contains required data. A config file contains all the sections mentioned above. The value of some parameters in the config file are too long and complicated, placing them explicitly in the file would complicate readability, therefore a replacement file is used to store these more complicated parts. The values are then referenced from the config file.

The `HistFactory` package [120], a tool created expressly for profile likelihood fits in the form of histograms, is used to do the actual fit. Statistical models described using HistFactory center around the simultaneous measurement of disjoint binned distributions (channels) observed as event counts n. For each channel, the overall expected event rate is the sum over a number of physics processes (samples). The sample rates may be subject to parametrised variations, both to express the effect of free parameters and to account for systematic uncertainties as a function of constrained parameters. In a frequentist framework these constraint terms can be viewed as auxiliary measurements with additional global observable data. A different partition is helpful in the context of hypothesis testing, where a subset of the parameters are declared parameters of interest (POI) and the remaining ones as nuisance parameters, in addition to the partition of the whole parameter set into free and constrained parameters. The signal strength of a process, the ratio of its cross section to a particular reference cross section such as that expected from the Standard Model, is part of the parameters of interest and the set of unconstrained, free parameters. Thus, the overall structure of a HistFactory probability model is a product of the analysis-specific model term describing the measurements of the channels and the analysis-independent set of constraint terms. Given the likelihood equation 6.7, constructed from observed data in all channels and the implied auxiliary data, measurements in the form of point and interval estimates can be defined. The majority of the parameters are nuisance parameters which are not the main target of the measurement but are necessary to correctly model the data. The unconstrained parameters declared as parameters of interest for which measurement hypothesis tests are performed, e.g. profile likelihood methods.

The `RooFit` [121] and `RooStats` [122] packages, which offer the tools required for the fit's execution, are the foundation upon which `HistFactory` is based. RooFit provides classes for facilitating the declaration of models and a way to re-use them in multiple statistical methods, since it has no statistical notion of parameters and observables. Therefore, it can work naturally with both frequentist and bayesian techniques. RooStats is considered as providing high-level statistical tools, while RooFit provides the core data modeling infrastructure. ProfileLikelihood calculator implements a likelihood-based method to estimate a confidence level and to perform hypothesis test for a given parameter value.

The `Minuit` algorithm [114] is used to minimize the likelihood and is implemented in `ROOT`, a `C++`-based data analysis framework [94]. Minuit is conceived as a tool to find the minimum value of a multi-parameter function and analyze the shape of the function around the minimum. To compute the best-fit parameter values and uncertainties, including correlations between the parameters, statistical analysis using log-likelihood functions is the main application. The 'best' values of a set of parameters are typically found using Minuit, where 'best' is defined as the values that minimise a specified function, FCN. The parameter errors, which are frequently referred as the width of the function minimum or, more generally, the shape of the function in some vicinity of the minimum, provide information on the uncertainty in the optimal parameter values. Minuit includes a number of tools to investigate the parameter error, which is a key feature. Uncertainties on the parameters are by default described using the quadratic approximation, while for more interesting parameters the more precise graphical method is used. Both methods were described previously in section 6.2.2.

6.3 Asimov fit results

A fit to the Asimov dataset is performed as the initial test. This is done to calculate the significance and determine how the fit will constrain the expectation. It also identifies which systematics will significantly impact the sensitivity. Figure 6.2 shows the data over simulation agreement for the variables used in the fit.

The fit results in a signal strength $\mu(tHq) = 1.00 \pm 3.12$, derived as described in section 6.2.4. The expected median significance of the 2LSS channel is 0.32 while the expected upper limit at 95% CL is 6.8. The resulting normalisation factors are shown in Fig. 6.3. Statistical uncertainty from limited number of events used to build the histograms for the predicted signal and background result in independent uncertainties in each bin, referred to as 'MC stat'. It is implemented in HistFactory/RooStats as additional NPs and assigned as gamma to the total prediction in each bin. Figure 6.3(right) shows the reasonable gamma uncertainties for each bins of signal and control regions used in the ASIMOV fit.

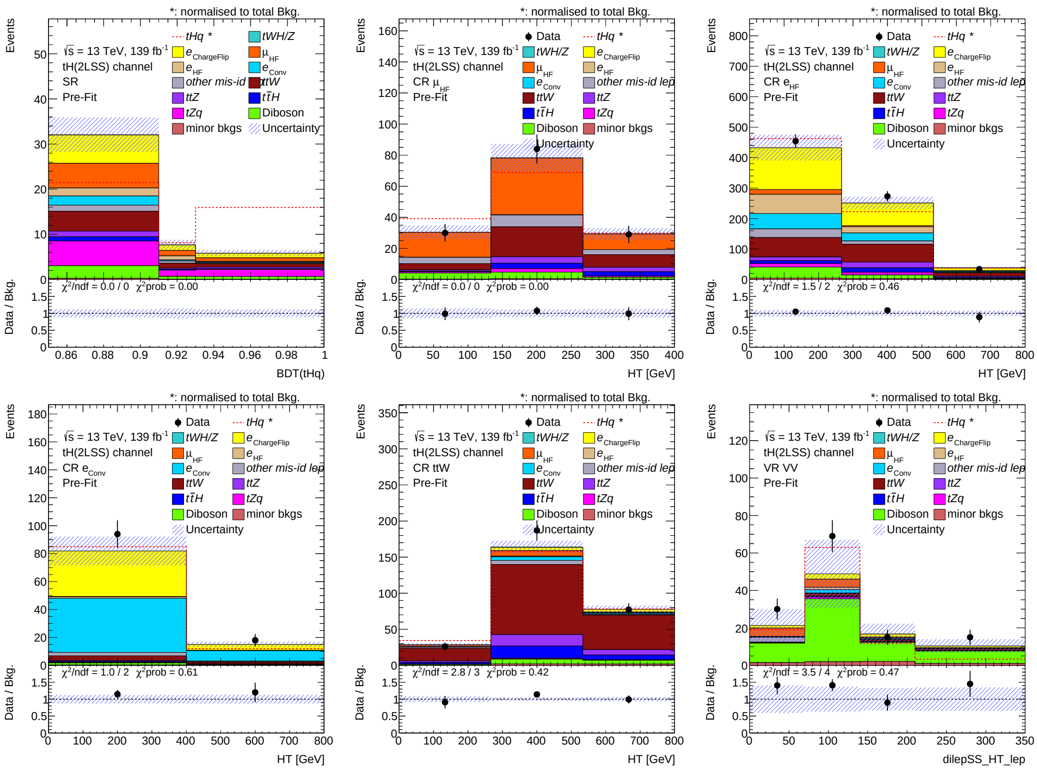

Figure 6.2: Pre-fit plots of the SR and CRs. The SR is fully blinded while the CRs show the real data events. The uncertainty band includes the statistical and systematic uncertainties.

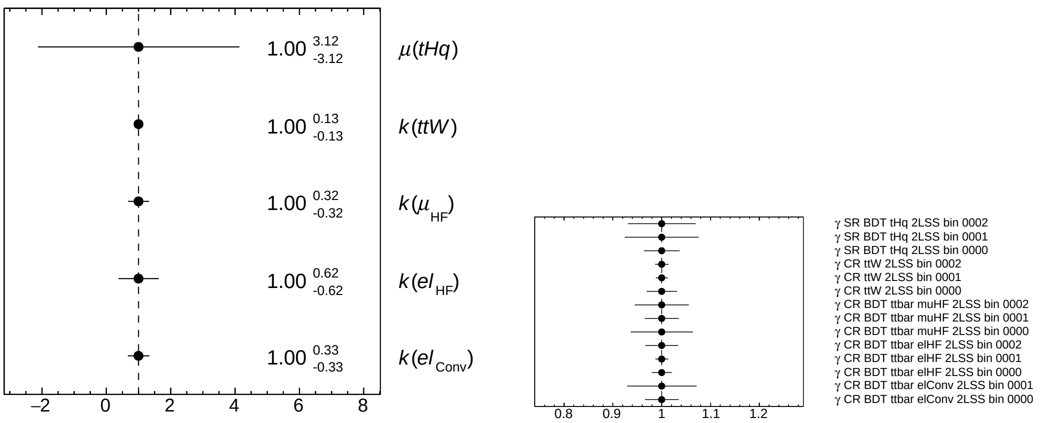

Figure 6.3: Normalisation factors derived form the Asimov fit. The uncertainty includes statistical and systematic effects. Left: The MC statistical (‘gamma‘) parameters derived form the Asimov fit.

The Nuisance parameters pull plots are shown in figure 6.4. No significant pull is observed demonstrating the stability of the fit model. Based on the variance indicated in formula 6.3, the likelihood fit also offers correlations between the various model parameters. Large correlations may indicate unnecessary degrees of freedom that are covered by other parameters or highly correlated variables that reduce the sensitivity of the analysis. To determine whether their impact may be lessened, those parameters can be further examined. The correlation matrix is shown in figure 6.5: the biggest anti-correlation ($\approx$ 66%) is the one between the $k(el_{Co})$ normalisation factor and the uncertainty on the charge flip electron background estimation.

In order to determine the true impact of the systematics on $\mu(tHq)$, a ranking plot is created, which ranks nuisance parameters according to their impact on the signal. This impact can be derived by fixing the nuisance parameter α_i of the given systematic to:

- ± 1 (the pre-fit value) for the pre-fit impact
- its post-fit value for the post-fit impact

and by performing the fit again. The difference in $\mu(tHq)$ between the nominal fit and the variation is then the displayed impact. Figure 6.6 shows the ranking plot for the Asimov fit. The nuisance parameters are ranked according to how much of an impact they have on $\mu(tHq)$ after fitting. The first 10 are displayed, although only a small number have a significant influence on the outcome. Similar to the plots in figure 6.4, the plot likewise depicts the pulls and constraints of the systematic variations.

As shown in table 6.2 in this statistical model the biggest contribution to the $\mu(tHq)$ is given by the data statistical uncertainty followed by the the JES and JER uncertainty.

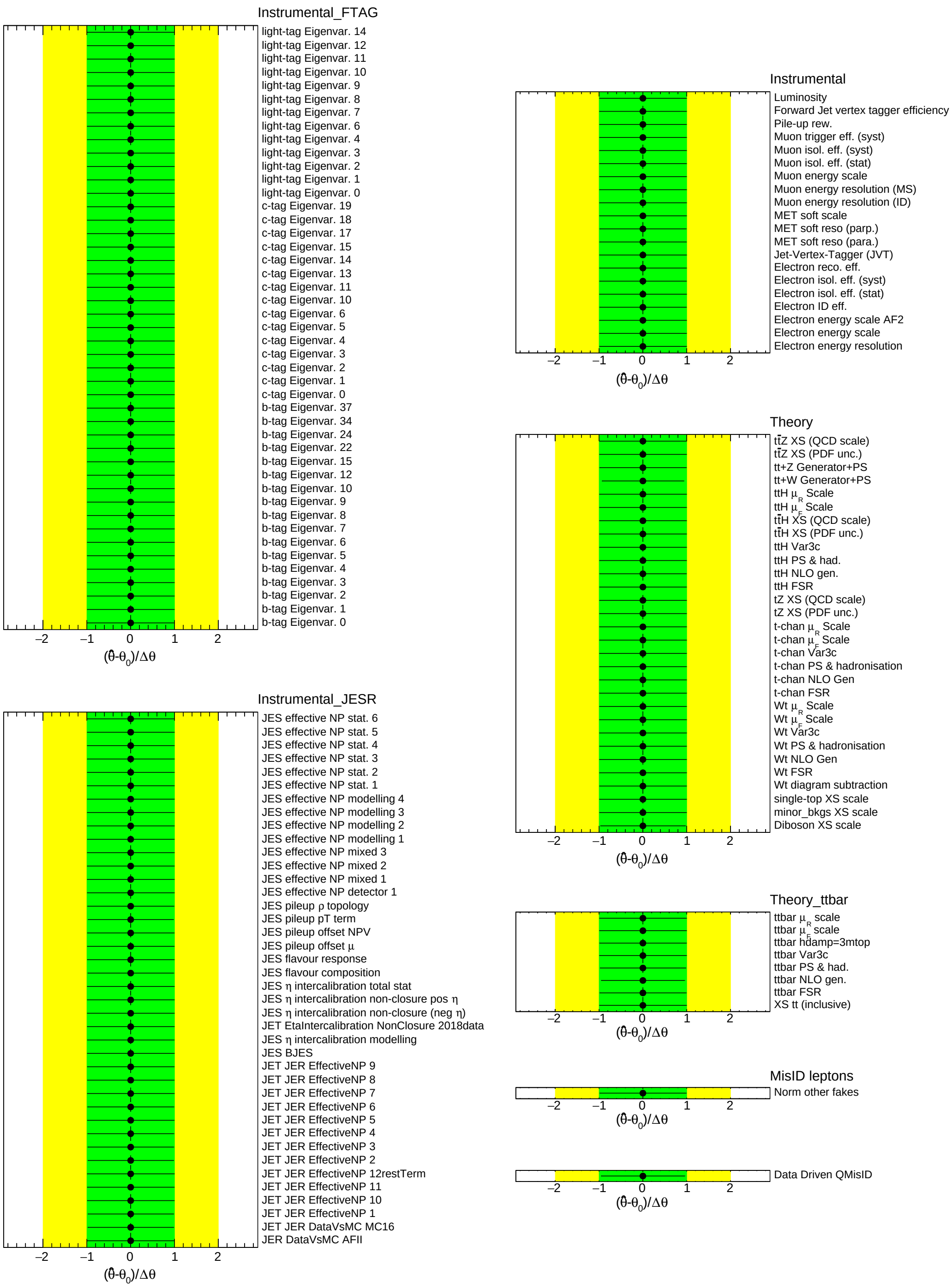

Figure 6.4: Nuisance parameters pull plot for the Asimov fit.

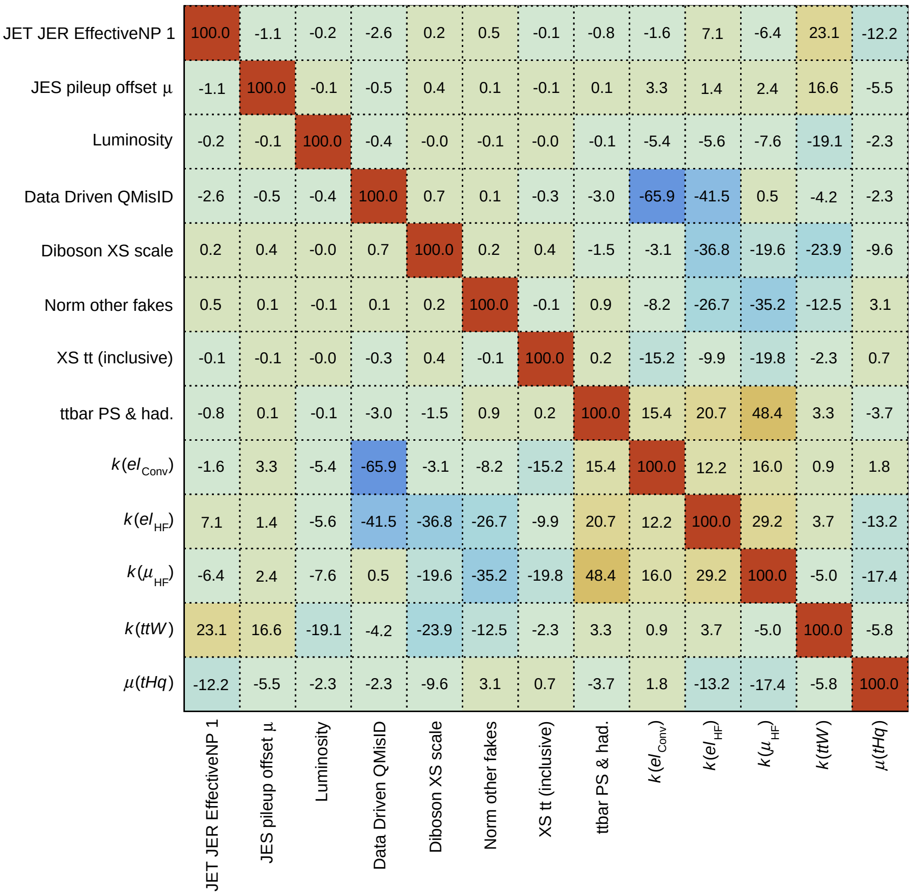

Figure 6.5: Correlation matrix for the Asimov fit.

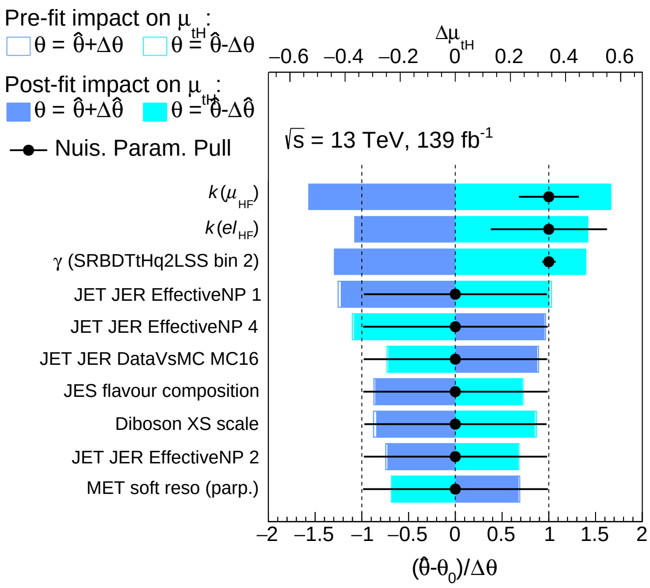

Figure 6.6: Ranking plot for the 10 nuisance parameters with the largest impact on the parameter of interest $\mu(tHq)$. It is shown for the pre-fit uncertainty by the empty box and post-fit by the filled box. The post-fit shifts and constraints of the systematics is displayed by the black markers and the horizontal line respectively.

Uncertainty source	Grouped impact
Gammas	0.5
JES/JER	0.9
Normalisation Factors	0.6
Theory	0.4
Instrumental	0.3
Theory $t\bar{t}$	0.1
Other fakes	0.1
Full Systematics	1.7
Data Statical	2.6
Total	3.1

Table 6.2: The grouped impact of uncertainties on the tHq signal strenght.

6.4 Backgrounds Fit

In order to test the background model and to get a better idea about its expected performance, the Background-only fits, or fits omitting the tHq signal and its modeling uncertainties in the likelihood, are performed in the revealed (not blinded) bins. There are various limitations to this. For example, the model's distributions can be comparable in the revealed bins but different in the blinded bins, resulting in different correlation and, thus, different post-fit values. For this fit the SR is fully blinded together with $\mu(tHq)$. The resulting normalisation factors are the free-floating factors only and their post-fit values are shown in figure 6.7. The normalisation factors for the mis-identified leptons background are well in agreement with the results as shown in section 5.2.1. The ttW normalisation factor is $1.34^{+0.35}_{-0.35}$ and it is in agreement with one.

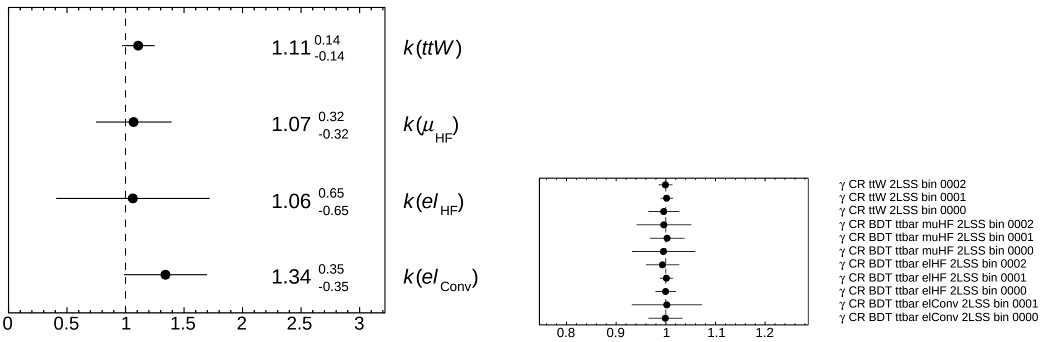

Figure 6.7: Left: Normalisation factors derived from fit to CRs data. The uncertainty includes statistical and systematic effects. Right: The gamma uncertainties.

The nuisance parameters are now shifted with respect to their nominal value, as can be seen in figure 6.8. No significant pull or constraint is observed. They are compatible with the nominal value 0 within one standard deviation. The correlation matrix in Fig. 6.9 shows a similar picture as for the Asimov fit results. Post-fit distributions of the analysis regions can be found in figure 6.10. They show good agreement, with χ^2 probability larger than 80% for the fake control regions.

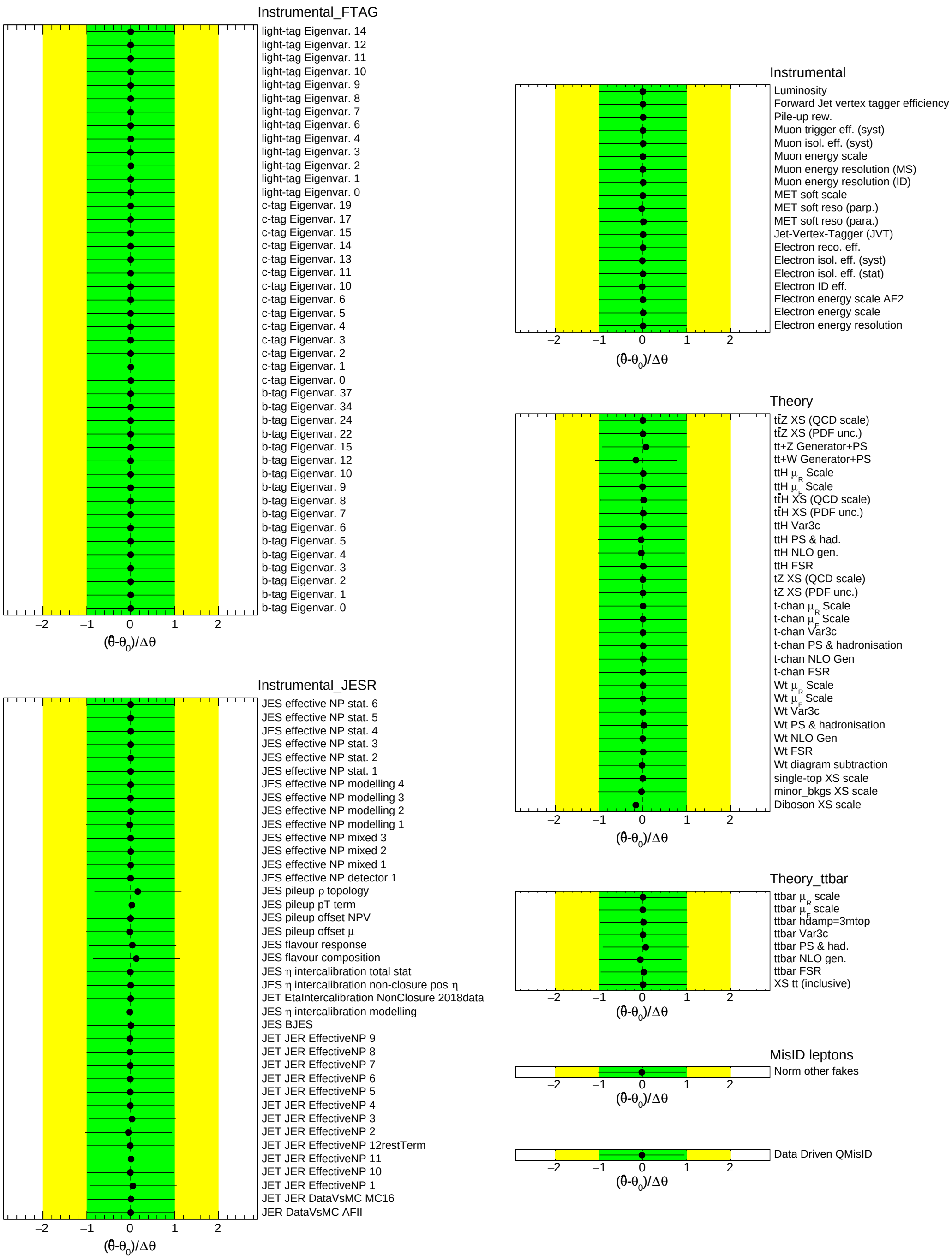

Figure 6.8: Nuisance parameters pull plot from fit to CRs data.

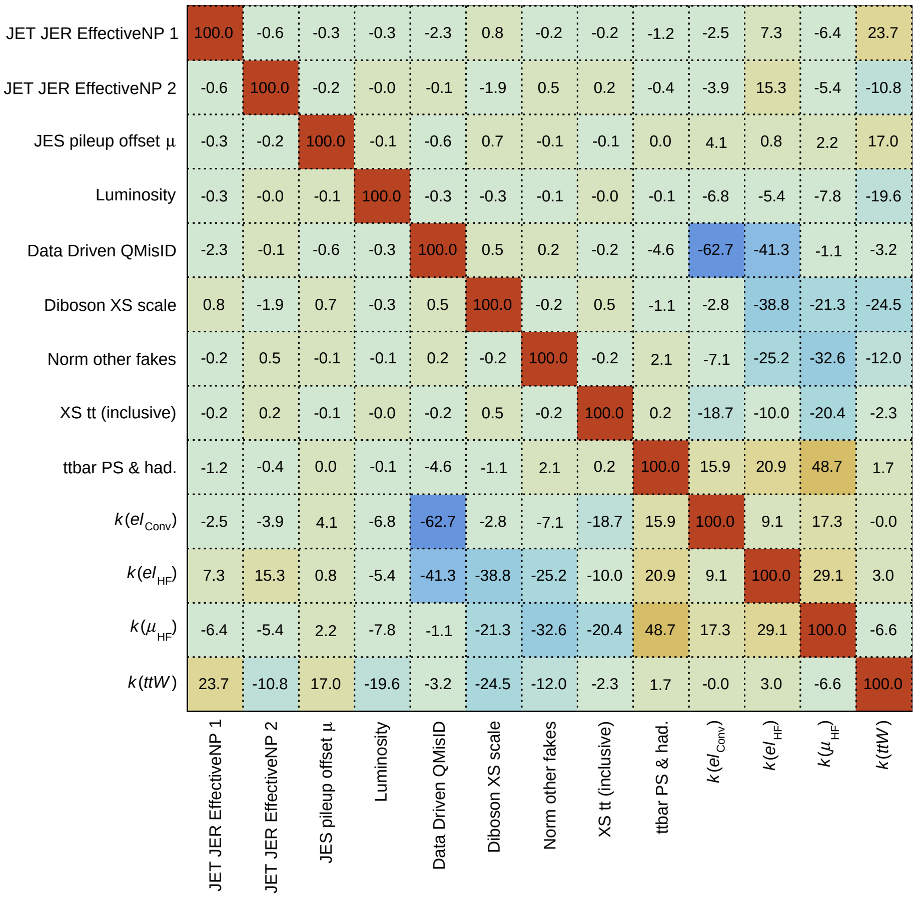

Figure 6.9: Correlation matrix from fit to CRs data.

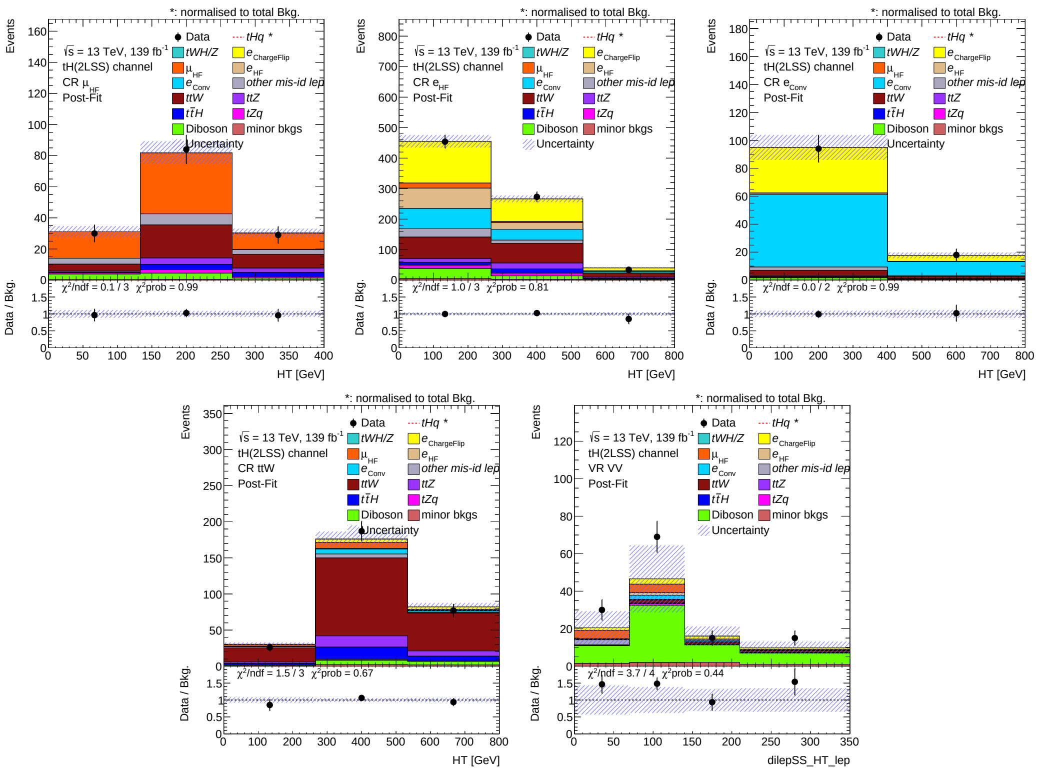

Figure 6.10: Post-fit plots CRs from fit on CRs data. The uncertainty band includes the statistical and systematic uncertainties.

6.5 Data fit results

After unblinding the fit has been performed to the data in one signal region. This section details the data fit results. A binned likelihood fit under the signal-plus-background hypothesis is performed on the BDT discriminant distribution. The unconstrained parameter of the fit is the signal strength. The resulting value of the signal strength is:

$$\mu(tHq) = 1.98 \pm 3.07 \text{ (Syst+Stat)} = 1.98 \pm 2.83 \text{ (StatOnly)}$$

corresponding to a expected median significance 0.32 σ. The figures 6.11 show the BDT output distributions before and after the signal-plus-background fit to the data for the tHq searches. Within the large statistical uncertainties the observed distributions are compatible with the background shapes. There is no indication of the excess of data from background. The exclusion limits are set on $\mu(tHq)$ with at least 95% confidence, derived by using test statistic q_μ in the CLs method which is computed using the asymptotic approximation. The table 6.3 shows the upper limit on $\mu(tHq)$ for SM-like hypothesis.

Coupling hypothesis	Channel	Expected Upper Limit				
		-2σ	-1σ	Median	+1σ	+2σ
$k_t = k_v = 1.0$ (SM-like)	$e^\pm e^\pm$ $\mu^\pm\mu^\pm$ $e^\pm\mu^\pm$	3.62	4.86	6.75	9.68	13.71

Table 6.3: Median value of expected upper limit of signal strength and the corresponding confidence intervals of ±1 and ±2 σ.

The observed and predicted yields after fit to the data are summarized in table 6.4. No significant pulls or constraints are obtained for the fitted nuisance parameters resulting in post-fit background predication in each analysis region that is very close to the pre-fit prediction albeit with reduced uncertainties resulting from the fit. The quoted uncertainties are the sum in quadrature of the statistical and systematic uncertainties of the yields.

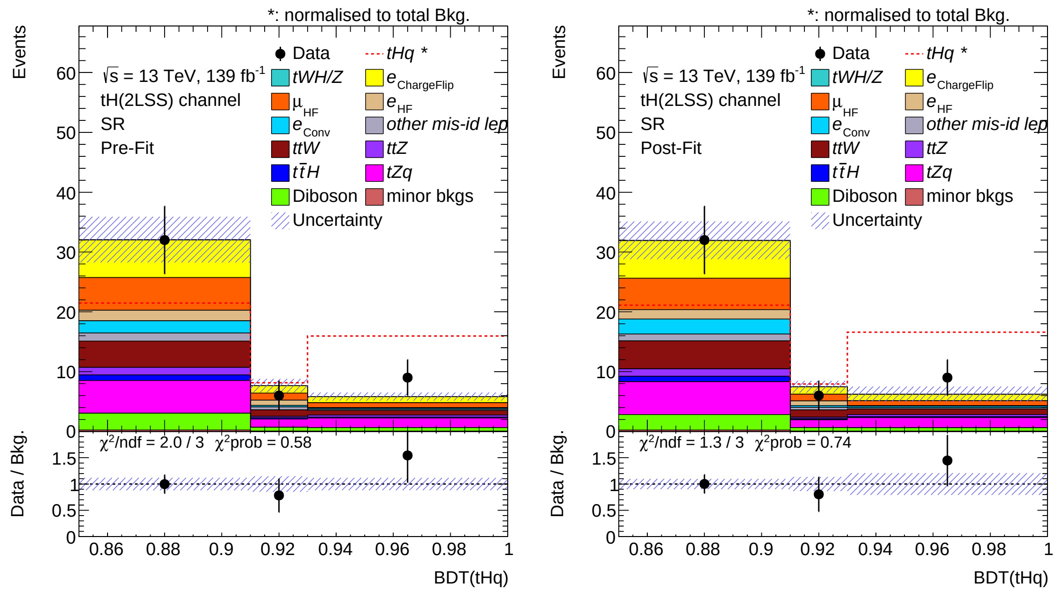

Figure 6.11: Pre(left) and post (right) plots obtained from signal-plus-background fit to data. The plots show the BDT output distribution in signal region. The error band shows total statistical and systematic uncertainties.

	SR	CR muHF	CR eHF	CR eConv	CR ttW	VR VV
tHq	4.26 ± 0.22	1.15 ± 0.09	4.17 ± 0.18	0.132 ± 0.013	0.79 ± 0.08	0.39 ± 0.07
tWH	0.086 ± 0.026	0.26 ± 0.05	1.04 ± 0.08	0.033 ± 0.009	0.66 ± 0.07	0.024 ± 0.017
el chargeflip	8.5 ± 1.3	0.00 ± 0.00	220 ± 40	37 ± 10	8.2 ± 1.6	6.7 ± 1.1
muHF	7.1 ± 2.7	65 ± 19	20 ± 6	0.25 ± 0.08	11 ± 4	10 ± 6
eHF	2.4 ± 1.8	0.00 ± 0.00	80 ± 50	1.2 ± 0.9	1.5 ± 1.2	1.6 ± 1.3
eConv	3.0 ± 1.4	0.00 ± 0.00	108 ± 29	62 ± 15	9.3 ± 2.8	3.4 ± 2.8
Other	1.8 ± 1.5	14 ± 12	42 ± 27	2.9 ± 2.7	9 ± 6	3 ± 4
ttW	6.8 ± 1.1	34 ± 4	147 ± 18	5.2 ± 0.7	179 ± 20	3.5 ± 0.6
ttZ	1.81 ± 0.32	7.8 ± 1.2	35 ± 5	1.09 ± 0.19	25 ± 4	0.75 ± 0.28
ttH	1.2 ± 0.4	6.7 ± 0.8	26.8 ± 3.3	0.79 ± 0.12	25.9 ± 3.0	0.29 ± 0.14
tZq	8.4 ± 0.8	3.8 ± 0.4	21.5 ± 1.9	0.66 ± 0.07	2.20 ± 0.26	1.57 ± 0.26
Diboson	3.7 ± 2.0	8 ± 5	46 ± 24	1.6 ± 0.8	12 ± 6	57 ± 30
minor bkgs	0.32 ± 0.17	1.0 ± 0.6	8 ± 4	0.33 ± 0.18	4.1 ± 2.1	7 ± 4
Total background	45 ± 4	141 ± 12	755 ± 28	113 ± 11	288 ± 17	95 ± 32
Data	47	143	761	112	290	129

Table 6.4: Post-fit yield of the analysis. Both statistical and systematic uncertainties are included.

Chapter 7 Conclusions and outlook

The work presented in this dissertation describes the search for the Higgs boson production in association with single top quark in two leptons (same-sign) final state. The data collected by ATLAS experiment at the center-of-mass energy of $\sqrt{s} = 13$ TeV during Run-II of Large Hardron Collider were considered, which correspond to integrated luminosity of 139 fb^{-1}. The coupling of Higgs boson to the top quark y_t is one of the fundamental properties of the Higgs boson. As the top quark is the heaviest particle in the Standard Model, y_t is expected to be large in the SM. Hence the measurement of y_t is important to prove the compatibility of the Higgs boson observed at the LHC and the properties predicted by the SM. Due to a destructive interference in tH production, this process provides sensitivity to the negative value of the coupling strength modifier $k_t = y_t/y_t^{SM}$. A measurement of SM-like tH production is challenging due to its small cross section. However, devation from y_t^{SM} would result in an enhanced tH cross section.

This measurement makes use of a strict electron and muon isolation requirement named as PromptLeptonImprovedVeto(PLIV) to distinguish between prompt and fake leptons. The use of PLIV provide very good rejection efficiency against the non-prompt leptons. Furthermore, analysis take advantage of the newest jets reconstruction techniques using the $anti-k_t$ jet algorithm on particle-flow objects and multi-variate b-tagging algorithm DL1r is used to improve the description of b-jets. In order to maximize the separation of the signal from the background, a multi-variate algorithm is employed in the signal enriched region which provide good discriminating power between signal and background. In addition, various control regions are used to better constrain modeling of the backgrounds.

One of the main backgrounds, fake leptons, the Template fit method is used to estimate its contribution and matrix method was used as a cross check. As this channel requires two leptons of same sign, there is a significant contribution from charge misidentify (QMisID) background. A separate data driven estimation was used to estimate QMisID background. Generally, good modelling of the fake backgrounds are achieved and results were verified by performing different closure tests .

To extract the signal strength from the data a binned profile likelihood fit is performed. Uncertainties in the signal and background predictions are incorporated by means of nuisance parameters. For standard model‑like Yukawa coupling ($y_t = 1$) there's no significant deviation from the background-only hypothesis. Therefore, the final measurement result of this thesis is the Asymptotic limit of signal strength while the signal strength is the ratio of observed cross section to one predicted by SM. The observed upper limit of signal strength at 95% CL is found to be 8.3, while Expected Upper Limit is: Medium Value: 6.75, $\pm 1\sigma$ confidence interval: [4.86; 9.68], $\pm 2\sigma$ confidence interval: [3.62; 13.71]. The dominating uncertainty on the measurement is the data statistical uncertainty. A larger datasets and the study of additional Higgs boson decay channels will be necessary to be able to measure tH production. In general, the new concepts which are presented in this thesis represent a basis of future measurement of the rare tH processes.

LHC has finished the Phase-I upgrade operation and next data taking operation for Run-3 has already started in 2022. I was involve to check the stability of small-strip thin gap chamber(sTGC) for the ATLAS new small wheel muon upgrade. My task was to perform production quality control test for the sTGC. The LHC will upgrade to High-Luminosity (HL-LHC) in 2026 for collecting pp collision data with total integrated luminosity up-to 3000 fb^{-1}. This will allow a precise determination of both the magnitude and the sign of the top quark Yukawa coupling.

Bibliography

[1] ATLAS collaboration, “Measurement of Higgs boson production in association with a $t\bar{t}$ pair in the diphoton decay channel using 139fb^{-1} of LHC data collected at $\sqrt{s} = 13$~TeV by the ATLAS experiment,” ATLAS-CONF-2019-004.

[2] CMS collaboration, “Measurement of the Higgs boson production rate in association with top quarks in final states with electrons, muons, and hadronically decaying tau leptons at $\sqrt{s} = 13$ TeV,” Eur. Phys. J. C **81** (2021) no.4, 378 doi:10.1140/epjc/s10052-021-09014-x [arXiv:2011.03652 [hep-ex]].

[3] S. L. Glashow, “Partial Symmetries of Weak Interactions,” Nucl. Phys. **22** (1961), 579-588 doi:10.1016/0029-5582(61)90469-2

[4] S. Weinberg, “A Model of Leptons,” Phys. Rev. Lett. **19** (1967), 1264-1266 doi:10.1103/PhysRevLett.19.1264

[5] S. L. Glashow, J. Iliopoulos and L. Maiani, “Weak Interactions with Lepton-Hadron Symmetry,” Phys. Rev. D **2** (1970), 1285-1292 doi:10.1103/PhysRevD.2.1285

[6] ATLAS collaboration, “Observation of a new particle in the search for the Standard Model Higgs boson with the ATLAS detector at the LHC,” Phys. Lett. B **716** (2012), 1-29 doi:10.1016/j.physletb.2012.08.020 [arXiv:1207.7214 [hep-ex]].

[7] ATLAS collaboration, “Observation of a new particle in the search for the Standard Model Higgs boson with the ATLAS detector at the LHC,” Phys. Lett. B **716** (2012), 1-29 doi:10.1016/j.physletb.2012.08.020 [arXiv:1207.7214 [hep-ex]].

[8] CMS collaboration, “Observation of a New Boson at a Mass of 125 GeV with the CMS Experiment at the LHC,” Phys. Lett. B **716** (2012), 30-61 doi:10.1016/j.physletb.2012.08.021 [arXiv:1207.7235 [hep-ex]].

[9] S. Abachi, “Observation of the top quark,” Phys. Rev. Lett. **74** (1995), 2632-2637 doi:10.1103/PhysRevLett.74.2632 [arXiv:hep-ex/9503003 [hep-ex]].

[10] LHC Higgs Cross Section Working Group, "Handbook of LHC Higgs Cross Sections: 4. Deciphering the Nature of the Higgs Sector," doi:10.23731/CYRM-2017-002 [arXiv:1610.07922 [hep-ph]].

[11] Cinzia De Melis. "The CERN accelerator complex."In: (Jan. 2016). General Photo. https://cds.cern.ch/record/2119882

[12] ATLAS collaboration, "Luminosity determination in pp collisions at $\sqrt{s}$ = 13 TeV using the ATLAS detector at the LHC," ATLAS-CONF-2019-021. Geneva: CERN, June 2019. http://cds.cern.ch/record/2677054

[13] ATLAS collaboration, "Public ATLAS Luminosity Results for Run-2 of the LHC," https://twiki.cern.ch/twiki/bin/view/AtlasPublic/LuminosityPublicResultsRun2

[14] Joao Pequenao. "Computer generated image of the whole ATLAS detector". Mar. 2008. https://cds.cern.ch/record/1095924

[15] Joao Pequenao. "Computer generated image of the ATLAS inner detector". Mar. 2008. https://cds.cern.ch/record/1095926

[16] Joao Pequenao."Computer Generated image of the ATLAS calorimeter". Mar. 2008. http://cds.cern.ch/record/1095927

[17] Joao Pequenao. "Computer generated image of the ATLAS Muons subsystem". Mar. 2008. urlhttps://cds.cern.ch/record/1095929

[18] HL-LHC Project. https://project-hl-lhc-industry.web.cern.ch/content/project-schedule

[19] ATLAS collaboration, "New Small Wheel Technical Design Report". Tech. rep. CERNLHCC- 2013-006, ATLAS-TDR-020. June 2013. http://cds.cern.ch/record/1552862

[20] ATLAS collaboration, "The New Small Wheel Upgrade Project of the ATLAS Experiment," Nucl. Part. Phys. Proc. **273-275** (2016), 1160-1165 doi:10.1016/j.nuclphysbps.2015.09.182

[21] P. Teterin, S. Bressler, S. Doronin, K. Filippov, I. Ravinovich, A. Romaniouk, D. Shchukin, V. Smakhtin, S. Smirnov and V. Tikhomirov, "The X-ray scanning technique application for sTGC detectors quality control," JINST **15** (2020) no.08, C08008 doi:10.1088/1748-0221/15/08/C08008

[22] V. O. Tikhomirov, K. A. Filippov, S. P. Konovalov, G. Mikenberg, A. Romaniouk, D. Shchukin, M. Shoa, V. Smakhtin, S. Y. Smirnov and V. V. Sosnovtsev, *et al.* "Visualization tool for X-ray scanner for sTGC detector production quality control," J. Phys. Conf. Ser. **675** (2016) no.1, 012018 doi:10.1088/1742-6596/675/1/012018

[23] CMS collaboration, "Search for associated production of a Higgs boson and a single top quark in proton-proton collisions at $\sqrt{s} = 13$ TeV," Phys. Rev. D **99** (2019) no.9, 092005 doi:10.1103/PhysRevD.99.092005 [arXiv:1811.09696 [hep-ex]].

[24] ATLAS Collaboration, "Documentation for TRExFitter", 2021, `https://trexfitter-docs.web.cern.ch/trexfitter-docs`

[25] ATLAS Collaboration, "SgTop ntuples contents twiki", 2019, `https:3626//twiki.cern.ch/twiki/bin/view/AtlasProtected/SgTopRun2NtuplesContents`

[26] ATLAS Collaboration, "TOPQ derivations twiki", 2021, `https://twiki.cern.ch/twiki/bin/view/AtlasProtected/TopDerivations`

[27] ATLAS Collaboration, "TOPQ derivations twiki", 2021, `https://twiki.cern.ch/twiki/bin/view/AtlasProtected/TopDerivations#The_TOPQ_derivation_formats`

[28] ATLAS Collaboration, "TOPQCommonSelection.py on GitLab", 2021, `https://gitlab.cern.ch/atlas/athena/-/blob/21.2/PhysicsAnalysis/DerivationFramework/DerivationFrameworkTop/`

[29] ATLAS Collaboration, "SingleTopAnalysis project on GitLab", 2021, `https://gitlab.cern.ch/atlasphys-top/singletop/SingleTopAnalysis`

[30] ATLAS Collaboration, "SingleTopAnalysis project on GitLa (tag v34)", 2021, `https:gitlab.cern.ch/atlasphys-top/singletop/SingleTopAnalysis/-/tree/v34`

[31] ATLAS Collaboration, "AnalysisTop twiki", 2021, `https://twiki.cern.ch/twiki/bin/view/AtlasProtected/AnalysisTop21`

[32] ATLAS Collaboration, “AnalysisTop twiki - release 21.2.181”, 2021, https://twiki.cern.ch/twiki/bin/viewauth/AtlasProtected/AnalysisTop21#21_2_181_built_on_2021_08_10

[33] ATLAS Collaboration, “Top Reconstruction Group twiki”, 2015, https://twiki.cern.ch/twiki/bin/view/AtlasProtected/TopReconstructionGroup

[34] ATLAS Collaboration, “tHqLoop README - GitLab”, 2022, https://gitlab.cern.ch/atlasphys-top/singletop/thq_13tev_rel21/thloop/-/blob/master/README.md

[35] ATLAS collaboration, “Performance of the ATLAS Trigger System in 2015,” Eur. Phys. J. C **77** (2017) no.5, 317 doi:10.1140/epjc/s10052-017-4852-3 [arXiv:1611.09661 [hep-ex]].

[36] ATLAS Collaboration, “2015 start-up trigger menu and initial performance assessment of the ATLAS trigger using Run-2 data”, ATL-DAQ-PUB-2016-001, 2016, https://cds.cern.ch/record/2136007

[37] ATLAS Collaboration, “Trigger Menu in 2016, ATL-DAQ-PUB-2017-001”, 2017, https://cds.cern.ch/record/2242069

[38] ATLAS Collaboration, “GoodRunLists for analysis (Run 2) twiki”, 2021, https://twiki.cern.ch/twiki/bin/viewauth/AtlasProtected/GoodRunListsForAnalysisRun2

[39] ATLAS collaboration, “Luminosity determination in pp collisions at $\sqrt{s}=$ 8 TeV using the ATLAS detector at the LHC,” Eur. Phys. J. C **76** (2016) no.12, 653 doi:10.1140/epjc/s10052-016-4466-1 [arXiv:1608.03953 [hep-ex]].

[40] ATLAS collaboration, “The new LUCID-2 detector for luminosity measurement and monitoring in ATLAS,” JINST **13** (2018) no.07, P07017 doi:10.1088/1748-0221/13/07/P07017

[41] ATLAS Collaboration, “AtlasProductionGroupMC16a twiki”, (2021), https://twiki.cern.ch/twiki/bin/view/AtlasProtected/AtlasProductionGroupMC16a

[42] ATLAS Collaboration, "AtlasProductionGroupMC16d twiki", (2021), `https:twiki.cern.ch/twiki/bin/view/AtlasProtected/AtlasProductionGroupMC16d`

[43] ATLAS Collaboration, "AtlasProductionGroupMC16e twiki", (2021), `https://twiki.cern.ch/twiki/bin/view/AtlasProtected/AtlasProductionGroupMC16e`

[44] ATLAS collaboration, "The ATLAS Simulation Infrastructure," Eur. Phys. J. C **70** (2010), 823-874 doi:10.1140/epjc/s10052-010-1429-9 [arXiv:1005.4568 [physics.ins-det]].

[45] T. Sjostrand, S. Mrenna and P. Z. Skands, "A Brief Introduction to PYTHIA 8.1," Comput. Phys. Commun. **178** (2008), 852-867 doi:10.1016/j.cpc.2008.01.036 [arXiv:0710.3820 [hep-ph]].

[46] T. Sjostrand, S. Mrenna and P. Z. Skands, "A Brief Introduction to PYTHIA 8.1," Comput. Phys. Commun. **178** (2008), 852-867 doi:10.1016/j.cpc.2008.01.036 [arXiv:0710.3820 [hep-ph]].

[47] R. D. Ball, V. Bertone, S. Carrazza, C. S. Deans, L. Del Debbio, S. Forte, A. Guffanti, N. P. Hartland, J. I. Latorre and J. Rojo, *et al.* "Parton distributions with LHC data," Nucl. Phys. B **867** (2013), 244-289 doi:10.1016/j.nuclphysb.2012.10.003 [arXiv:1207.1303 [hep-ph]].

[48] ATLAS collaboration, "The Pythia 8 A3 tune description of ATLAS minimum bias and inelastic measurements incorporating the Donnachie-Landshoff diffractive model," ATL-PHYS-PUB-2016-017.

[49] ATLAS collaboration, "Measurement of the Inelastic Proton-Proton Cross Section at $\sqrt{s} = 13$ TeV with the ATLAS Detector at the LHC," Phys. Rev. Lett. **117** (2016) no.18, 182002 doi:10.1103/PhysRevLett.117.182002 [arXiv:1606.02625 [hep-ex]].

[50] J. Alwall, R. Frederix, S. Frixione, V. Hirschi, F. Maltoni, O. Mattelaer, H. S. Shao, T. Stelzer, P. Torrielli and M. Zaro, "The automated computation of tree-level and next-to-leading order differential cross sections, and their matching to parton shower simulations," JHEP **07** (2014), 079 doi:10.1007/JHEP07(2014)079 [arXiv:1405.0301 [hep-ph]].

[51] R. D. Ball *et al.* [NNPDF], "Parton distributions for the LHC Run II," JHEP **04** (2015), 040 doi:10.1007/JHEP04(2015)040 [arXiv:1410.8849 [hep-ph]].

[52] T. Sjöstrand, S. Ask, J. R. Christiansen, R. Corke, N. Desai, P. Ilten, S. Mrenna, S. Prestel, C. O. Rasmussen and P. Z. Skands, "An introduction to PYTHIA 8.2," Comput. Phys. Commun. **191** (2015), 159-177 doi:10.1016/j.cpc.2015.01.024 [arXiv:1410.3012 [hep-ph]].

[53] A. Buckley, "ATLAS Pythia 8 tunes to 7 TeV data," ATL-PHYS-PROC-2014-273.

[54] S. Frixione, E. Laenen, P. Motylinski and B. R. Webber, "Angular correlations of lepton pairs from vector boson and top quark decays in Monte Carlo simulations," JHEP **04** (2007), 081 doi:10.1088/1126-6708/2007/04/081 [arXiv:hep-ph/0702198 [hep-ph]].

[55] P. Artoisenet, R. Frederix, O. Mattelaer and R. Rietkerk, "Automatic spin-entangled decays of heavy resonances in Monte Carlo simulations," JHEP **03** (2013), 015 doi:10.1007/JHEP03(2013)015 [arXiv:1212.3460 [hep-ph]].

[56] D. J. Lange, "The EvtGen particle decay simulation package," Nucl. Instrum. Meth. A **462** (2001), 152-155 doi:10.1016/S0168-9002(01)00089-4

[57] ATLAS Collaboration, "TopCommonObjects13TeV twiki", 2021, `https://twiki.cern.ch/twiki/bin/view/AtlasProtected/TopCommonObjects13TeV`

[58] ATLAS Collaboration, "Lowest un-prescaled triggers per data-taking period twiki", 2020, `https://twiki.cern.ch/twiki/bin/view/Atlas/LowestUnprescaled`

[59] ATLAS Collaboration, "TrigGlobalEfficiencyCorrectionTool twiki", 2022, `https://twiki.cern.ch/twiki/bin/viewauth/Atlas/TrigGlobalEfficiencyCorrectionTool`

[60] ATLAS Collaboration, "XAODMatchingTool", 2019, `https://twiki.cern.ch/twiki/bin/viewauth/Atlas/XAODMatchingTool`

[61] ATLAS collaboration, "Electron reconstruction and identification in the ATLAS experiment using the 2015 and 2016 LHC proton-proton col-

lision data at $\sqrt{s}$ = 13 TeV," Eur. Phys. J. C **79** (2019) no.8, 639 doi:10.1140/epjc/s10052-019-7140-6 [arXiv:1902.04655 [physics.ins-det]].

[62] ATLAS collaboration, "Electron and photon performance measurements with the ATLAS detector using the 2015–2017 LHC proton-proton collision data," JINST **14** (2019) no.12, P12006 doi:10.1088/1748-0221/14/12/P12006 [arXiv:1908.00005 [hep-ex]].

[63] ATLAS Collaboration, "ATLAS Isolation and Fake Forum", 2022, https://twiki.cern.ch/twiki/bin/view/AtlasProtected/IsolationFakeForum

[64] ATLAS Collaboration, "Recommended Lepton Isolation Working Points," 2022, https://twiki.cern.ch/twiki/bin/view/AtlasProtected/RecommendedIsolationWPs

[65] ATLAS Collaboration, "Definition of Prompt Lepton Improved Veto", 2022,https://twiki.cern.ch/twiki/bin/view/AtlasProtected/PLImprovedWPs

[66] ATLAS Collaboration, "Electron Efficiencies for Run 2 (scale factors and uncertainties)", 2021, https://twiki.cern.ch/twiki/bin/view/AtlasProtected/ElectronEfficiencyRun2

[67] ATLAS Collaboration, 'Electron Charge ID Selector Tool', 2022, https://twiki.cern.ch/twiki/bin/view/AtlasProtected/ElectronChargeFlipTaggerTool

[68] ATLAS Collaboration, "EGamma ambiguity tool in analysis", 2022, https://twiki.cern.ch/twiki/bin/view/AtlasProtected/EGammaIdentificationRun2#Using_the_Ambiguity_tool_in_anal

[69] ATLAS Collaboration, "EGamma ambiguity tool in analysis", 2022, https://twiki.cern.ch/twiki/bin/view/AtlasProtected/EGammaIdentificationRun2#Using_the_Ambiguity_tool_in_anal

[70] ATLAS Collaboration, "MCP Analysis Guidelines for MC16", 2021, https://twiki.cern.ch/twiki/bin/view/AtlasProtected/MCPAnalysisGuidelinesMC16

[71] ATLAS collaboration, "Muon reconstruction performance of the ATLAS detector in proton–proton collision data at $\sqrt{s}$ =13 TeV," Eur. Phys. J. C

76 (2016) no.5, 292 doi:10.1140/epjc/s10052-016-4120-y [arXiv:1603.05598 [hep-ex]].

[72] ATLAS collaboration, "Muon reconstruction and identification efficiency in ATLAS using the full Run 2 pp collision data set at $\sqrt{s} = 13$ TeV," Eur. Phys. J. C **81** (2021) no.7, 578 doi:10.1140/epjc/s10052-021-09233-2 [arXiv:2012.00578 [hep-ex]].

[73] ATLAS Collaboration, "Muon Selection Tool in Rel. 21", 2022, `https://twiki.cern.ch/twiki/bin/view/Atlas/MuonSelectionToolR21`

[74] M. Cacciari, G. P. Salam and G. Soyez, "The anti-k_t jet clustering algorithm," JHEP **04** (2008), 063 doi:10.1088/1126-6708/2008/04/063 [arXiv:0802.1189 [hep-ph]].

[75] ATLAS collaboration, "Jet reconstruction and performance using particle flow with the ATLAS Detector," Eur. Phys. J. C **77** (2017) no.7, 466 doi:10.1140/epjc/s10052-017-5031-2 [arXiv:1703.10485 [hep-ex]].

[76] M. Cacciari, G. P. Salam and G. Soyez, "FastJet User Manual," Eur. Phys. J. C **72** (2012), 1896 doi:10.1140/epjc/s10052-012-1896-2 [arXiv:1111.6097 [hep-ph]].

[77] ATLAS Collaboration, "Tagging and suppression of pileup jets with the ATLAS detector", ATLAS-CONF-2014-018, 2014, `https://cds.cern.ch/record/1700870`

[78] ATLAS collaboration, "Performance of pile-up mitigation techniques for jets in pp collisions at $\sqrt{s} = 8$ TeV using the ATLAS detector," Eur. Phys. J. C **76** (2016) no.11, 581 doi:10.1140/epjc/s10052-016-4395-z [arXiv:1510.03823 [hep-ex]].

[79] ATLAS Collaboration, "Jet Vertex Tagger for Run 2 in reco and analysis", 2021, `https://twiki.cern.ch/twiki/bin/view/AtlasProtected/JetVertexTaggerTool`

[80] ATLAS Collaboration, "Pileup jet recommendations", 2021, `https://twiki.cern.ch/twiki/bin/view/AtlasProtected/PileupJetRecommendations`

[81] ATLAS collaboration, "Jet energy scale and resolution measured in proton–proton collisions at $\sqrt{s} = 13$ TeV with the ATLAS detector," Eur. Phys. J. C **81** (2021) no.8, 689 doi:10.1140/epjc/s10052-021-09402-3 [arXiv:2007.02645 [hep-ex]].

[82] ATLAS Collaboration, "Commissioning of the ATLAS -tagging algorithms using $t\bar{t}$ events in early Run 2 data", ATL-PHYS-PUB-2015-039, 2015, https://cds.cern.ch/record/2047871

[83] ATLAS Collaboration, "Optimisation and performance studies of the ATLAS b-tagging algorithms for the 2017-18 LHC run", ATL-PHYS-PUB-2017-013, 2017, https://cds.cern.ch/record/2273281

[84] ATLAS Collaboration, "Identification of Jets Containing b-Hadrons with Recurrent Neural Networks at the ATLAS Experiment", ATL-PHYS-PUB-2017-003, 2017, https://cds.cern.ch/record/2255226

[85] ATLAS collaboration, "ATLAS b-jet identification performance and efficiency measurement with $t\bar{t}$ events in pp collisions at $\sqrt{s} = 13$ TeV," Eur. Phys. J. C **79** (2019) no.11, 970 doi:10.1140/epjc/s10052-019-7450-8 [arXiv:1907.05120 [hep-ex]].

[86] ATLAS Collaboration, "Measurement of -tagging efficiency of c-jets in $t\bar{t}$ events using a likelihood approach with the ATLAS detector", ATLAS-CONF-2018-001, 2018, https://cds.cern.ch/record/2306649

[87] ATLAS Collaboration, "Calibration of light-flavour b-jet mistagging rates using ATLAS proton–proton collision data at $\sqrt{s} = 13$ TeV", ATLAS-CONF-2018-006, 2018, https://cds.cern.ch/record/2314418

[88] ATLAS Collaboration, "Performance of missing transverse momentum reconstruction with the ATLAS detector in the first proton–proton collisions at $\sqrt{s} = 13$ TeV" , ATL-PHYS-PUB-2015-027, 2015, https://cds.cern.ch/record/2037904

[89] ATLAS Collaboration, "AnalysisTop Overlap Removal", 2021, https://twiki.cern.ch/twiki/bin/view/AtlasProtected/TopRecoObjTwikiModel#Overlap_Removal

[90] ATLAS Collaboration, "Combined Performance Tools for Physics Analysis: Event Cleaning", 2017,https://twiki.cern.ch/twiki/bin/view/AtlasProtected/PhysicsAnalysisWorkBookRel20CPRec#Event_cleaning

[91] ATLAS collaboration, "ATLAS data quality operations and performance for 2015–2018 data-taking," JINST **15** (2020) no.04, P04003 doi:10.1088/1748-0221/15/04/P04003 [arXiv:1911.04632 [physics.ins-det]].

[92] ATLAS collaboration, "Monitoring and data quality assessment of the ATLAS liquid argon calorimeter," JINST **9** (2014), P07024 doi:10.1088/1748-0221/9/07/P07024 [arXiv:1405.3768 [hep-ex]].

[93] ATLAS Collaboration, "JetEtmiss Recommendations R21: How to clean jets", 2021, https://twiki.cern.ch/twiki/bin/view/AtlasProtected/HowToCleanJetsR21

[94] I. Antcheva, M. Ballintijn, B. Bellenot, M. Biskup, R. Brun, N. Buncic, P. Canal, D. Casadei, O. Couet and V. Fine, *et al.* "ROOT: A C++ framework for petabyte data storage, statistical analysis and visualization," Comput. Phys. Commun. **180** (2009), 2499-2512 doi:10.1016/j.cpc.2009.08.005 [arXiv:1508.07749 [physics.data-an]].

[95] A. Hocker, P. Speckmayer, J. Stelzer, J. Therhaag, E. von Toerne, H. Voss, M. Backes, T. Carli, O. Cohen and A. Christov, *et al.* "TMVA - Toolkit for Multivariate Data Analysis," [arXiv:physics/0703039 [physics.data-an]].

[96] Holland, John H."Genetic Algorithms" Scientific American, vol. 267, no. 1, 1992, pp. 66–73. JSTOR, http://www.jstor.org/stable/24939139

[97] F. Demartin, F. Maltoni, K. Mawatari and M. Zaro, "Higgs production in association with a single top quark at the LHC," Eur. Phys. J. C **75** (2015) no.6, 267 doi:10.1140/epjc/s10052-015-3475-9 [arXiv:1504.00611 [hep-ph]].

[98] CERN, "SM Higgs production cross sections at $\sqrt{s}$" = 13 TeV, https://twiki.cern.ch/twiki/bin/view/LHCPhysics/CERNYellowReportPageAt13TeV

[99] ATLAS collaboration, "Estimation of non-prompt and fake lepton backgrounds in final states with top quarks produced in proton-proton collisions at $\sqrt{s}$ =8 TeV with the ATLAS detector," ATLAS-CONF-2014-058.

[100] ATLAS Collaboration, "TruthClassification package", 2022, `https://gitlab.cern.ch/atlas/athena/-/tree/21.2/PhysicsAnalysis/AnalysisCommon/TruthClassification`

[101] ATLAS Collaboration, "Monte Carlo Truth Classifier", 2022, `https://twiki.cern.ch/twiki/bin/viewauth/AtlasProtected/MCTruthClassifier`

[102] ATLAS Collaboration, "Egamma CP: Background Electron Classification", 2022 `https://twiki.cern.ch/twiki/bin/viewauth/AtlasProtected/EGammaTruthRun2`

[103] ATLAS Collaboration, "Muon Truth Information for Run 2", 2022, `https://twiki.cern.ch/twiki/bin/view/AtlasProtected/MuonTruthRun2`

[104] ATLAS Collaboration, "ATLAS Isolation and Fake Forum", 2022 `https://twiki.cern.ch/twiki/bin/view/Sandbox/YoheiYamaguchiSandbox20210104`

[105] ATLAS collaboration, "Estimation of non-prompt and fake lepton backgrounds in final states with top quarks produced in proton-proton collisions at \sqrts=8~TeV with the ATLAS detector," ATLAS-CONF-2014-058.

[106] ATLAS collaboration, "Search for supersymmetry at $\sqrt{s}$=8 TeV in final states with jets and two same-sign leptons or three leptons with the ATLAS detector," JHEP **06** (2014), 035 doi:10.1007/JHEP06(2014)035 [arXiv:1404.2500 [hep-ex]].

[107] E. W. Varnes, "A Poisson likelihood approach to fake lepton estimation with the matrix method," [arXiv:1606.06817 [hep-ex]].

[108] J. Erdmann, C. Grunwald, K. Kröninger, S. La Cagnina, L. Röhrig and E. Varnes, "Reformulation of a likelihood approach to fake-lepton estimation in the framework of Bayesian inference," Nucl. Instrum. Meth. A **1021** (2022), 165939 doi:10.1016/j.nima.2021.165939 [arXiv:2106.13628 [hep-ph]].

[109] ATLAS collaboration, "Measurement of the top quark-pair production cross section with ATLAS in pp collisions at $\sqrt{s}$ = 7 TeV," Eur. Phys. J. C **71** (2011), 1577 doi:10.1140/epjc/s10052-011-1577-6 [arXiv:1012.1792 [hep-ex]].

[110] G. Bohm and G. Zech, “Statistics of weighted Poisson events and its applications,” Nucl. Instrum. Meth. A **748** (2014), 1-6 doi:10.1016/j.nima.2014.02.021 [arXiv:1309.1287 [physics.data-an]].

[111] ATLAS Collaboration, “Electron Efficiencies for Run 2 (scale factors and uncertainties)”, 2022, `https://twiki.cern.ch/twiki/bin/view/AtlasProtected/ElectronEfficiencyRun2`

[112] ATLAS Collaboration, “Extracting Muon Efficiencies for Analyses”, `https://twiki.cern.ch/twiki/bin/view/AtlasProtected/MuonEfficienciesForAnalysis`

[113] ATLAS Collaboration, “Electron Charge ID Selector Tool, 2022”, `https://twiki.cern.3876ch/twiki/bin/view/AtlasProtected/ElectronChargeFlipTaggerTool`

[114] F. James, “MINUIT Function Minimization and Error Analysis: Reference Manual Version 94.1,” CERN-D-506.

[115] ATLAS collaboration, “Analysis of $t\bar{t}H$ and $t\bar{t}W$ production in multilepton final states with the ATLAS detector,” ATLAS-CONF-2019-045.

[116] G. Cowan, “Statistical data analysis”, Oxford University Press, USA, 1998

[117] G. Cowan, K. Cranmer, E. Gross and O. Vitells, “Asymptotic formulae for likelihood-based tests of new physics,” Eur. Phys. J. C **71** (2011), 1554 [erratum: Eur. Phys. J. C **73** (2013), 2501] doi:10.1140/epjc/s10052-011-1554-0 [arXiv:1007.1727 [physics.data-an]].

[118]

[118] M. Tanabashi *et al.* [Particle Data Group], “Review of Particle Physics,” Phys. Rev. D **98** (2018) no.3, 030001 doi:10.1103/PhysRevD.98.030001

[119] R. Cousins, “Generalization of Chisquare Goodness-ofFit Test for Binned Data Using Saturated Models , with Application to Histogram”, 2013, `http://www.physics.ucla.edu/~cousins/stats/cousins_saturated.pdf`

[120] K. Cranmer, G. Lewis, L. Moneta, A. Shibata, and W. Verkerke, “HistFactory: A tool for creating statistical models for use with RooFit and RooStats”, tech. rep. CERNOPEN-2012-016, New York U., 2012, `https://cds.cern.ch/record/1456844`

[121] W. Verkerke and D. P. Kirkby, “The RooFit toolkit for data modeling,” eConf **C0303241** (2003), MOLT007 [arXiv:physics/0306116 [physics]].

[122] L. Moneta, K. Belasco, K. S. Cranmer, S. Kreiss, A. Lazzaro, D. Piparo, G. Schott, W. Verkerke and M. Wolf, “The RooStats Project,” PoS **ACAT2010** (2010), 057 doi:10.22323/1.093.0057 [arXiv:1009.1003 [physics.data-an]].

附录 A Appendices

A.1 List of variables included in the training of the BDT

Variable name	$t\bar{t}$	VV	ttW	tHq	Description
$p_{\mathrm{T,min}}$	×	-	×	×	p_{T} of softest lepton
$E_{\mathrm{T}}^{\mathrm{miss}}/H_{\mathrm{T}}$	-	×	-	-	Ratio between $E_{\mathrm{T}}^{\mathrm{miss}}$ and H_{T}
$\eta(\text{No-}b\text{-jet})_{\max}$	-	-	×	-	Maximum η value among non-b-tagged jets.
$E_{\mathrm{T}}^{\mathrm{miss}}$	×	×	×	×	$E_{\mathrm{T}}^{\mathrm{miss}}$.
$\Sigma_i\text{charge}(\ell_i)$	×	×	×	×	Sum of lepton charges.
E_pt	×	×	×	×	$\sqrt{\Sigma_i(E_{\ell_i}^2 + p_{T,\ell_i}^2)}$
$m_H(WW)$	×	-	×	×	Mass of a candidate Higgs Boson when decays to a pair of W bosons.
$\Delta m(Z,\ell\ell)$	×	×	×	-	Difference between the invariant mass of $\ell\ell$ and the mass of the Z boson.
$\Delta\phi(\phi_T^{\mathrm{miss}},\ell_2)$	-	-	×	-	$\Delta\phi$ between ϕ_T^{miss} and ℓ_2
$N(\text{non-}b\text{-jet})$	-	×	-	×	Number of non b-tagged jets.
$N(\text{central-jet})$	×	×	×	×	Number of central jets.
$N(b\text{-jet})$	×	×	×	-	Number of b-tagged jets.
$m(j_s)$	-	-	-	×	Mass of the spectator jet.
$E(j_s)$	-	-	-	×	Energy of the spectator jet.
$p_T(j_s)$	-	-	-	×	p_{T} of the spectator jet.
$\chi^2(m(\ell_i,\ell_j)_{\mathrm{top}})_{\min}$	×	×	×	-	Minimum χ^2 value between the masses of top candidates given by the combination of leptons.
$m(\ell,\ell)_{\mathrm{top}}$	×	×	×	-	Invariant mass between two leptons giving best top visible mass
H_{T}	-	×	-	×	H_{T}.

Table A.1: List of variables included in the training of the BDTs. The × indicates in which BDTs the variable is used

Variable name	$t\bar{t}$	VV	ttW	tHq	Description
$H_{\mathrm{T}}(\ell\ell)$	×	-	×	×	Sum of the transverse momentum of the two leptons.
$H_{\mathrm{T}}(\mathrm{jets})$	×	-	×	-	Sum of the transverse momentum of the jets.
$m(\mathrm{jet},\mathrm{jet})_W$	-	×	×	×	Mass of the best two jet candidates for the W boson.
$m(\mathrm{jet},\mathrm{jet})_{\mathrm{top}}$	×	×	×	×	Mass of the best top quark candidate from jets.
$m(\ell_2,\mathrm{jet}_2)$	×	×	×	×	Invariant mass of ℓ_2 and jet_2.
$m(\ell_2,\mathrm{jet}_1)$	×	×	-	×	Invariant mass of ℓ_2 and jet_1..
$m(\ell_1,\mathrm{jet}_2)$	-	-	-	×	Invariant mass of ℓ_1 and jet_2.
$m(\ell_1+\ell_2,\mathrm{jet}_2)$	-	-	×	-	Invariant mass of both leptons and jet_2.
$m(\ell_1+\ell_2,\mathrm{jet}_1+\mathrm{jet}_2)$	-	-	×	×	Invariant mass of both leptons, the leading jet and the second jet.
$m(\ell_1+\ell_2,\mathrm{jet}_1)$	×	-	-	-	Invariant mass of both lepton and the jet_1.
$m(\mathrm{jet}_1+\mathrm{jet}_2)$	-	×	×	×	Invariant mass of the leading jet and the second jet.
$m(\ell_1+\ell_2)$	×	×	×	×	Invariant mass of both leptons.
p_{FW4}	×	×	-	-	Fourth Fox–Wolfram moment.
p_{FW1}	-	-	×	-	First Fox–Wolfram moment.
Lepton flavours	×	-	-	-	Identification of the flavour of the leptons.
$e\mu$-events	×	×	-	-	Identification of the events $e\mu$.
ee-events	-	×	×	×	Identification of the events ee.
$\Delta R(\text{non-}b\text{-jet},\ell_1)$	-	-	-	×	ΔR between the ℓ_1 and its closest non b-jet.
$\Delta R(\text{non-}b\text{-jet},\ell_2)$	-	-	-	×	ΔR between the ℓ_2 and its closest non b-jet.

Table A.1: List of variables included in the training of the BDTs. The × indicates in which BDTs the variable is used

Variable name	$t\bar{t}$	VV	ttW	tHq	Description
$\Delta R(\ell_2, b\text{-jet})$	×	×	-	-	ΔR and $\Delta\eta$ between ℓ_2
$\Delta\eta(\ell_2, b\text{-jet})$	×	×	-	-	and the its closest b-jet.
$m(b\text{-jet}, j_s)$	-	-	×	×	Invariant mass, ΔR, $\Delta\eta$
$\Delta R(b\text{-jet}, j_s)$	-	-	×	×	between the spectator jet
$\Delta\eta(b\text{-jet}, j_s)$	×	-	-	-	and the leading b-jet.
$\Delta R(\ell_1, b\text{-jet})$	×	×	-	-	ΔR and $\Delta\eta$ between
$\Delta\eta(\ell_1, b\text{-jet})$	×	×	-	-	ℓ_1 and its closest b-jet.
$\Delta R(\ell, j_f)$	×	-	-	-	ΔR and $\Delta\eta$ between the leading.
$\Delta\eta(\ell, j_f)$	-	-	-	×	j_f and its closest lepton.
$\Delta\phi(\ell, \ell)$	-	-	×	-	$\Delta\phi$, ΔR, $\Delta\eta$.
$\Delta R(\ell, \ell)$	×	-	×	-	ΔR between the two leptons.
$\Delta\eta(\ell, \ell)$	-	-	-	×	$\Delta\eta$
b-score$_1$	×	×	×	×	DL1r score of leading b-jet
b-score$_2$	×	×	×	-	DL1r score of second b-jet
b-score$_3$	×	×	×	-	DL1r score of third b-jet